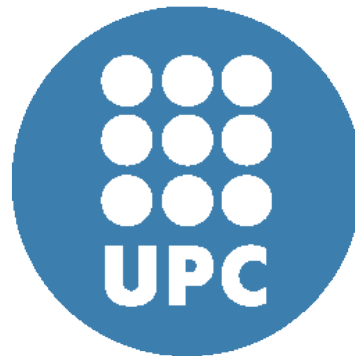


KUNGLIGA TEKNISKA HÖGSKOLAN
UNIVERSITAT POLITÈCNICA DE CATALUNYA

Nuclear Energy Engineering
Reactor Physics Department

Master thesis

**Safety aspects of
Ceramic Fully Encapsulated fuel
for Light Water Reactors**



GUILLERMO DÍEZ FERNÁNDEZ

Erasmus Student Exchange Cooperation between
Universitat Politècnica de Catalunya (UPC) and
Kungliga Tekniska Högskolan (KTH)

August 2012

TRITA-FYS 2012:71
ISSN 0280-316X
ISRN KTH/FYS/--12:71--SE

Printed by Universitetservice US-AB, Stockholm 2012

*“I hear and I forget,
I see and I remember,
I do and I understand.”*

*Confucius (551 BC - 479 BC)
Chinese philosopher & reformer*

Abstract

Japan's nuclear disaster has highlighted important inherent weaknesses regarding to the nuclear fuel behavior after shutdown in Light Water Reactors. The low thermal conductivity and the low fission products retention capacity of oxide fuel, combined with important amounts of zirconium in the clad, lead to an uncontrollably soon fuel failure after losing the coolant inside the core.

The purpose of this thesis is to study the feasibility of replacing current oxide fuel used in Light Water Reactor with an alternative fuel that performs a better behavior under these accident conditions. The alternative fuel studied is the Fully Ceramic Micro-encapsulated (FCM) fuel based on the TRISO particles technology, which enhances safety after a loss-of-coolant accident because of its better thermal conductivity and fission products retention capability. The aim of the project is to compare the neutronics behavior and safety parameters between the current 17x17 Westinghouse fuel assembly and a new fuel assembly model, designed to replace the original but using FCM fuel. The analyses have been done using the SERPENT code, based in the Monte Carlo probabilistic methodology.

The thesis is mainly divided in three stages. The first part involves the design of the fuel assembly models desired to benchmark, with especial attention to the description of the FCM fuel configuration, result of a compatibility study with the original. The second part is addressed to obtain all the simulation parameters decided to use for the following calculations. The last part is focused on analyzing the results obtained from these simulations, especially comparing the safety parameters between both fuel configurations.

The final results show a better behavior of FCM fuel regarding to the neutronics under accident conditions. However, temperature feedbacks tend to be more positive with the new fuel, especially at the end of the cycle and with a significant concentration of boron in the water.

Resumen

El desastre nuclear sucedido en Japón ha puesto de manifiesto debilidades inherentes muy importantes en relación al comportamiento del combustible nuclear después de parada en los reactores de agua ligera. La baja conductividad térmica y la poca capacidad de retener los productos de fisión por parte del óxido de uranio, combinado con importantes concentraciones de zirconio en la vaina, conducen a la falla incontrolablemente rápida del combustible después de perder el refrigerante en el núcleo.

El objetivo de esta tesis es estudiar la viabilidad de remplazar el óxido de uranio usado actualmente por un combustible alternativo que presente un mejor comportamiento en condiciones de accidente. El combustible alternativo estudiado es el combustible encapsulado *Fully Ceramic Micro-encapsulated (FCM)* basado en la tecnología de las partículas TRISO, que mejora la seguridad en caso de accidente de pérdida de refrigerante gracias a su mejor conductividad térmica y capacidad de retención de los productos de fisión. El propósito del proyecto es comparar el comportamiento neutrónico y los parámetros seguridad entre el elemento combustible 17x17 de Westinghouse actual y un nuevo modelo, diseñado para remplazar al original usando el combustible FCM. Los análisis se han realizado usando el código computacional SERPENT, basado en la metodología probabilista de Monte Carlo.

La tesis está dividida básicamente en tres etapas. La primera parte engloba el diseño de los elementos combustibles que se desean comparar, con especial atención a la descripción de la configuración que usa combustible FCM, resultado de un estudio de compatibilidad con la original. La segunda parte está dirigida a obtener todos los parámetros de simulación que se han decidido usar para los posteriores cálculos. La última parte está enfocada al análisis de los resultados obtenidos en estas simulaciones, especialmente comparando los parámetros de seguridad entre las dos configuraciones.

Los resultados finales muestran un mejor comportamiento neutrónico del combustible FCM en condiciones de accidente. No obstante, los coeficientes de realimentación por temperatura tienden a ser más positivos para el nuevo combustible, especialmente a final de ciclo y con una concentración significativa de boro en el agua.

Resum

El desastre nuclear succeït a Japó ha manifestat debilitats inherents molt importants en relació al comportament del combustible nuclear després de parada en reactors d'aigua lleugera. La baixa conductivitat tèrmica i la poca capacitat de retenir els productes de fissió per part de l'òxid d'urani, combinat amb importants concentracions de zirconi a la beina, condueixen a la falla incontrolablement ràpida del combustible després de perdre el refrigerant al nucli.

L'objectiu d'aquesta tesi és estudiar la viabilitat de substituir l'òxid d'urani que s'utilitza actualment per un combustible alternatiu que presenti un millor comportament en condicions d'accident. El combustible alternatiu estudiat es el combustible encapsulat *Fully Ceramic Micro-encapsulated (FCM)* basat en la tecnologia de les partícules TRISO, que millora la seguretat en cas d'accident de pèrdua de refrigerant gràcies a la seva millor conductivitat tèrmica i capacitat de retenció dels productes de fissió. El propòsit del projecte és comparar el comportament neutrònic i els paràmetres de seguretat entre l'element combustible 17x17 de Westinghouse actual i un nou model, dissenyat per substituir l'original utilitzant combustible FCM. Els anàlisis s'han realitzat utilitzant el codi computacional SERPENT, basat en la metodologia probabilista de Monte Carlo.

La tesi està dividida bàsicament en tres etapes. La primera engloba el disseny dels elements combustibles que es desitgen comparar, amb especial atenció a la descripció de la configuració de que utilitza combustible FCM, resultat d'un estudi de compatibilitat amb l'original. La segona part està dirigida a obtenir tots els paràmetres de simulació que s'han decidit utilitzar pels càlculs posteriors. La última part està enfocada a l'anàlisi dels resultats obtinguts en aquestes simulacions, especialment comparant els paràmetres de seguretat entre les dues configuracions.

El resultats finals mostren un millor comportament neutrònic per part del combustible FCM en condicions d'accident. No obstant, els coeficients de realimentació per temperatura tendeixen a ser més positius utilitzant el nou combustible, especialment a final de cicle i amb una concentració significativa de bor a l'aigua.

Acknowledgments

First and foremost, I would like to express my sincere gratitude to my supervisor Prof. Waclaw Gudowsky, for giving me the opportunity to come to KTH, for providing me the project idea and for being concerned for my happiness here in Sweden, which has been extremely important for me. This thesis would have not been possible without US Nuclear collaboration, in particular Dr. Francesco Venneri, who I wish to deeply acknowledge for providing me essential data and information in the field.

I would like to thank all the members in the reactor physics department, especially my office mates Antoine and Karl, for the good environment and their supports. And of course say thank you to Sara, who deserves a separate chapter in the story. A thousand thanks for your time, company, comprehension and invaluable help.

I wish to use this opportunity to thank all my friends that have accompanied me in this Swedish adventure, but particularly to my old friends Adri and Fran, for their friendship and hand-in-hand working during several years. Also to say thanks to my family, especially my grandparents, Aita for his knowledge and advice, Ama for believing in me in everything I do, and my sister Irene for her never failing love.

Last but not least, thank you María for your support and for showing me that love does not know any distance. I feel very lucky.

I want to dedicate this thesis to my wise grandpa, because he started everything.

I gratefully acknowledge financial support of the European Erasmus Program and the Consejo de Seguridad Nuclear (CSN) – Universitat Politècnica de Catalunya (UPC) ARGOS fellowship program.

Abbreviations

α_{fuel}	Fuel Temperature Coefficient
α_{mod}	Moderator Temperature Coefficient
α_V	Void Coefficient
BDBA	Beyond Design-Basis Accident
BISO	Bistructural-Isotropic
BOL	Begin Of Life
BWR	Boling Water Reactor
CRAM	Chebyshev Rational Approximation Method
CPU	Central Processing Unit
CVR	Coolant Void Reactivity (Void Worth)
DBA	Design-Basis Accident
EFPD	Effective Full-Power Days
EOL	End Of Life
FA	Fuel Assembly
FCM	Fully Ceramic Microencapsulated
FEM	Finite Element Method
FOM	Figure Of Merit
FTC	Fuel Temperature Coefficient
HM	Heavy Metal
HTGC	High Temperature Gas Cooled
HTR	High Temperature Reactor
IPyC	Inner Pyrolytic Carbon
KD	Kernel Diameter
LEU	Low Enriched Uranium
LWR	Light Water Reactor
MTC	Moderator Temperature Coefficient
NITE	Nano-Infiltration and Transient Eutectic-phase
NPP	Nuclear Power Plant
OPyC	Outer Pyrolytic Carbon
PBR	Pebble Bed Reactor
PF	Packing Fraction
PSA	Probabilistic Safety Analysis
PSG	Probabilistic Scattering Game
PWR	Pressurized Water Reactor
PyC	Pyrolytic Carbon
RBMK	<i>Reaktor Bolshoy Moshchnosti Kanalniy</i> (High Power Channel-type Reactor)
SCRAM	Safety Control Rod Ax Man
SDP	Slowing Down Power
SG	Steam Generator
TRISO	Tristructural-isotropic
TRU	Transuranic radionuclide
TTA	Transmutation Trajectory Analysis
UCO	Uranium Carbide / Uranium Oxide
UN	Uranium Nitrate

Contents

Abstract	V
Resumen	VI
Resum	VII
Acknowledgments	VIII
Abbreviations	IX
List of Figures	XIII
List of Tables	XV
1. Introduction	1
1.1. Nuclear power	1
1.2. Light Water Reactors and oxide fuel.....	2
1.3. Nuclear power safety challenges.....	6
1.3.1. Severe accident scenario in LWRs.....	7
1.3.2. Safety weaknesses in current LWRs.....	8
1.3.3. Meltdown resistant fuel and thesis purpose	9
2. Theoretical background	11
2.1. FCM fuel.....	11
2.1.1. FCM fuel description.....	11
2.1.2. FCM fuel advantages.....	14
2.1.3. Technological landscape	15
2.2. Safety parameters.....	15
2.2.1. Fuel Temperature Coefficient (Nuclear Doppler Effect)	15
2.2.2. Moderator Temperature Coefficient.....	17
2.2.3. Void coefficient	18
2.2.4. Void worth	19

3. Methodology	21
3.1. Neutron transport.....	21
3.1.1. Neutron definition	21
3.1.2. Neutron transport equation	23
3.1.3. Integral form of the transport equation and final solution	24
3.2. Simulation tools	26
3.2.1. Deterministic codes	26
3.2.2. Probabilistic codes	26
3.3. The Monte Carlo Method	27
3.3.1. The analog Monte Carlo estimation	27
3.3.2. The implicit Monte Carlo estimation	28
3.4. The SERPENT code	29
3.4.1. SERPENT advantages.....	30
4. Fuel Assembly Models	33
4.1. 17x17 Westinghouse fuel assembly	33
4.2. 13x13 FCM fuel assembly	38
4.2.1. Compatibility study	39
5. Simulation	49
5.1. Simulation parameters analysis.....	49
5.1.1. Analog and implicit estimations comparison	51
5.1.2. Number of cycles and neutron population.....	54
5.1.3. Burnup parameters.....	60
5.2. TRISO particles modeling comparison.....	65
6. Results and discussion	69
6.1. Reactivity curves	69
6.2. Safety parameters.....	74
6.2.1. MTC.....	74
6.2.2. MTC (1000ppm boron)	82
6.2.3. FTC.....	85
6.2.4. Void worth	89
7. Conclusions	95
Bibliography	97

List of Figures

Figure 1.1. World marketed energy consumption, 2007-2035.....	1
Figure 1.2. World electricity generation by fuel, 2007-2035	2
Figure 1.3. Binding energy per nucleon versus mass number	3
Figure 1.4. Pressurized Water Reactor outline	4
Figure 1.5. Boiling Water Reactor outline	4
Figure 1.6. Stages of the nuclear fuel manufacturing process.....	5
Figure 1.7. Fuel rod cladding.....	5
Figure 1.8. Example of a whole core cross-cut with hexagonal fuel assemblies	6
Figure 2.1. TRISO particle geometry	11
Figure 2.2. SiC crack with OPyC layer.....	13
Figure 2.3. SiC crack without OPyC layer	13
Figure 2.4. FCM pellet with TRISO loading.....	13
Figure 2.5. Temperature distribution over pellet section	14
Figure 2.6. ²³⁵ U fission cross section	16
Figure 2.7. ²³⁸ U absorption resonances	16
Figure 2.8. 1/v dependence of the ²³⁸ U absorption cross section	18
Figure 3.1. Neutron's phase space	22
Figure 3.2. Neutron motion along Ω	25
Figure 3.3. Schematic of decisions to generate the “history” of a neutron in the analog Monte Carlo estimation	28
Figure 4.1. 17x17 Westinghouse fuel assembly.....	33
Figure 4.2. 17x17 FA fuel rod geometry.....	34
Figure 4.3. 17x17 FA guide tube geometry	34
Figure 4.4. 17x17 FA Z=0 cross-cut.....	35
Figure 4.5. 17x17 FA fuel pin materials.....	35
Figure 4.6. Temperature distribution over UO ₂ pellet section	36
Figure 4.7. Density – Temperature water curve for 150kg/cm ² pressure.....	36
Figure 4.8. Total fuel assembly water channel.....	40
Figure 4.9. One fuel pin water channel.....	40
Figure 4.10. UN enrichment depending on KD – PF configuration	43
Figure 4.11. UN enrichment depending on PF value for KD=700 μ m.....	43
Figure 4.12. Regular cubical 3D lattice TRISO particles distribution	44
Figure 4.13. Hexagonal prismatic 3D lattice TRISO particles distribution.....	44
Figure 4.14. Random TRISO particles distribution using explicit particle fuel model.....	45
Figure 4.15. 13x13 FA fuel pin geometry	46
Figure 4.16. 13x13 FA guide tube geometry	46
Figure 4.17. 13x13 FCM FA Z=0 cross-cut	46
Figure 4.18. Materials of 13x13 FCM FA	47
Figure 4.19. Temperature distribution over a UN pellet section	48

Figure 5.1. Difference between accuracy and precision	50
Figure 5.2. The normal distribution and the 68%, 95% and 99% confidence intervals	51
Figure 5.3. FOM using Analog k_{eff} estimation	52
Figure 5.4. σx using Analog k_{eff} estimation.....	52
Figure 5.5. FOM using Implicit k_{eff} estimation.....	53
Figure 5.6. σx using Implicit k_{eff} estimation.....	53
Figure 5.7. FOM for 1000 cycles and 25000 neutron population	55
Figure 5.8. σx for 1000 cycles and 25000 neutron population.....	55
Figure 5.9. FOM for 1000 cycles and 50000 neutron population	56
Figure 5.10. σx for 1000 cycles and 50000 neutron population	56
Figure 5.11. FOM for 1000 cycles and 80000 neutron population	57
Figure 5.12. σx for 1000 cycles and 80000 neutron population.....	57
Figure 5.13. FOM for 1000 cycles and 100000 neutron population	58
Figure 5.14. σx for 1000 cycles and 100000 neutron population.....	58
Figure 5.15. Number of steps influence on last step result	64
Figure 5.16. Regular distribution of TRISO using an infinite 3D lattice	65
Figure 5.17. Random distribution of TRISO using explicit model	65
Figure 5.18. 3D lattice and explicit model reactivity curves comparison	66
Figure 6.1. Burnup curves versus EFPD.....	71
Figure 6.2. Reactivity curves versus burnup	71
Figure 6.3. Depletion rate comparison	72
Figure 6.4. Resonance escape probability (ρ) comparison	73
Figure 6.5. ^{235}U depletion.....	73
Figure 6.6. ^{239}Pu mass versus EFPD	74
Figure 6.7. MTC linear fitting example.....	75
Figure 6.8. MTC burnup calculation.....	78
Figure 6.9. ^{238}U - ^{235}U ratio versus time	78
Figure 6.10. Decrease of the resonance scape probability (ρ) comparison.....	79
Figure 6.11. ^{135}Xe radiative capture cross section.....	79
Figure 6.12. ^{149}Sm radiative capture cross section.....	80
Figure 6.13. ^{240}Pu mass versus time.....	80
Figure 6.14. ^{149}Sm mass versus time	81
Figure 6.15. Oxide fuel ρ factor variation.....	81
Figure 6.16. FCM fuel ρ factor variation.....	81
Figure 6.17. MTC comparison for 0ppm and 1000ppm boron concentration	84
Figure 6.18. FTC linear fitting example	85
Figure 6.19. FTC comparison.....	87
Figure 6.20. CVR comparison	91
Figure 6.21. Burnup calculation for k_{eff} with and without water in the core	91
Figure 6.22. Fission probability of TRU in a thermal and fast neutron spectrum.....	92
Figure 6.23. ^{242}Pu fission cross section	93
Figure 6.24. ^{242}Pu mass with and without water in the core	93

List of Tables

Table 4.1. 17x17 FA dimensions	34
Table 4.2. Water density values for 150kg/cm ² pressure (Range of interest).....	37
Table 4.3. Zirlo TM nuclei composition and used values	37
Table 4.4. Number of TRISO particles inside a fuel rod depending on KD – PF configuration	42
Table 4.5. UN enrichment depending on KD – PF configuration	42
Table 4.6. 13x13 FCM FA dimensions.....	46
Table 4.7. TRISO particles materials description.....	47
Table 5.1. Comparison between analog and implicit k_{eff} estimations.....	54
Table 5.2. Different number and length steps burnup calculation	60
Table 5.3. Comparison between TTA method and CRAM method	61
Table 5.4. Burnup calculation for k_{eff} convergence (5 to 20 equal steps)	62
Table 5.5. Burnup calculation for k_{eff} convergence (30 to 60 equal steps)	63
Table 5.6. Number of steps and step length comparison	64
Table 5.7. 3D lattice and explicit model comparison	67
Table 6.1. Burnup calculation for the 17x17 Westinghouse FA and the 13x13 FCM FA	70
Table 6.2. MTC burnup calculation	77
Table 6.3. MTC burnup calculation for 1000ppm boron concentration	83
Table 6.4. FTC burnup calculation	86
Table 6.5. SDP for H ₂ O and carbon moderators.....	88
Table 6.6. CVR burnup calculation	90

Chapter 1

Introduction

1.1. Nuclear power

Energy consumption is an essential need in nowadays society, and represents one of the more important factors involved when determining the overall development of a country. The center of gravity for world energy consumption continues to shift from the OECD¹ to emerging economies, especially in Asia, due to their extremely fast current development. Although demand in the OECD tends to slightly increase, the growing importance of the non-OECD economies leads to enormously magnify the projections of the marketed energy consumption for the next decades (see Figure 1.1). The main example of this increasing tendency is China, which accounts the 71% of the global energy consumption growth [1].

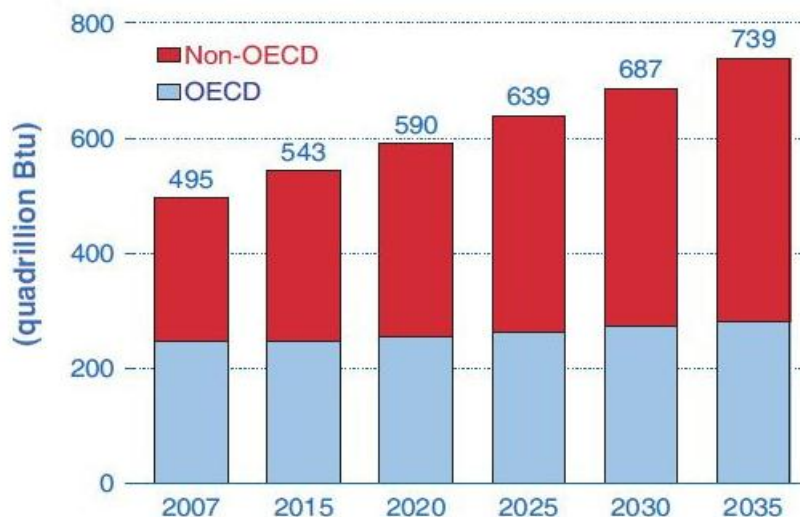


Figure 1.1. World marketed energy consumption, 2007-2035²

¹ The OECD is the Organization for Economic Co-operation and Development of 34 countries founded in 1961 to stimulate economic progress and world trade.

² Energy & Capital. <http://www.energyandcapital.com/articles/runaway-energy-demand/1455>

Nowadays, nuclear power supplies the 16%³ of the world's electricity, although after Fukushima Daiichi accident worldwide nuclear output fell during the last year, mainly because of the declines in Italy, Japan and Germany. However, nuclear power has an important role in order to meet this increasing demand of energy while minimizing the emission of greenhouse gases. Projections indicate that nuclear power will increase accordingly to the world consumption growth (see Figure 1.2), which is noticed basically by the important number of new nuclear power plants (NPPs) that are already under construction, especially in countries such as China (28), Russia (11) or India (7)⁴.

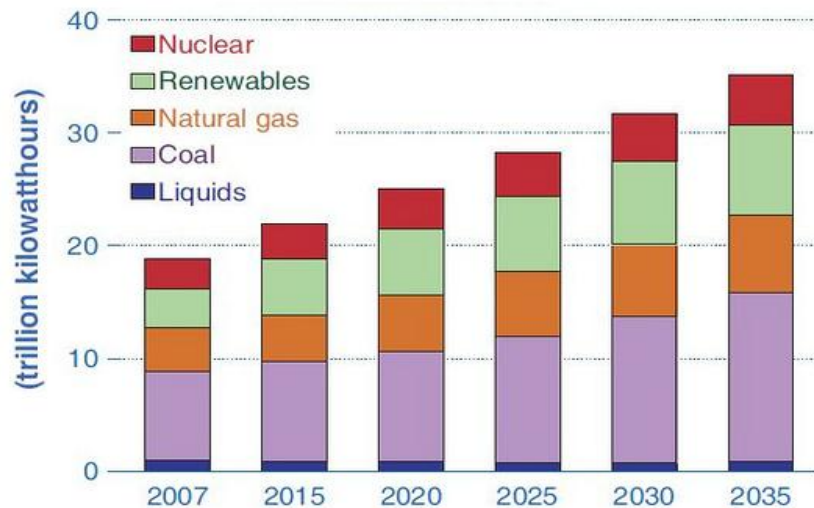


Figure 1.2. World electricity generation by fuel, 2007-2035

On the other hand, independently from the expected tendency of the nuclear power, the truth is that a logical controversy for nuclear energy has been created during the last year as a consequence of Japan's disaster, even leading to drastic political decisions as giving up nuclear power. This situation forces nuclear industry and research to do an important step forward in the nuclear field, in order to make nuclear power more convincing especially in safety concerns. This is the motivation and the focus given by this thesis.

1.2. Light Water Reactors and oxide fuel

NPPs are built to generate electricity from the nuclear energy released from the controlled fission process of nuclear fuel, which is a physical process that entails the splitting of uranium atoms or other fissile elements inside a nuclear reactor. This energy release ($\sim 200\text{MeV}$ per fission) is explained by equation (1.1), probably the most famous expression in all of physics. It describes the equivalence of mass (m) and energy (E), which are related by the square of the speed of light (c^2).

$$E = mc^2 \quad (1.1)$$

³ World Nuclear Association. <http://www.world-nuclear.org/how/npreactors.html>

⁴ European Nuclear Society. <http://www.euronuclear.org/info/encyclopedia/n/nuclear-power-plant-world-wide.htm>

It must be taken into account that a nucleus is a bound system of Z protons and N neutrons, whose total energy is less than the energy of its constituent parts far apart and at rest. This means that energy must be supplied to separate a nucleus into individual protons and neutrons, which is called the *binding energy* (E_B). Due to the equivalence of mass and energy, this energy difference can be expressed in mass terms, called *mass defect* (Δm), which expresses the difference between the nucleus mass and its constituents mass far apart and at rest.

By the fission process, a nucleus splits into other nuclei that have a higher binding energy (higher mass defect), obtaining a difference between the initial and final masses of the involved nucleons and thus leading to an important energy release (see Figure 1.3). It must be noticed that fusion energy follows the same principle, but by joining together two or more atoms.

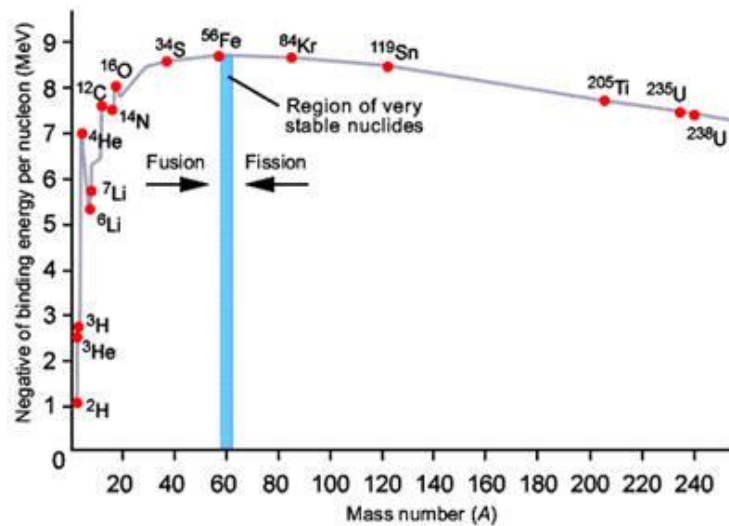


Figure 1.3. Binding energy per nucleon versus mass number⁵

Besides releasing energy, fission process also generates new neutrons that are able to produce new fissions, and thus generate more energy. Nowadays, this chain reaction can be controlled inside various types of nuclear reactors. One of the most common nuclear reactors in the world and the one this thesis deals with is the **Light Water Reactor (LWR)**, which is characterized by absorbing the nuclear energy as thermal energy in a primary circuit of ordinary water (H_2O). This water plays two roles into the reactor: coolant and neutron moderator⁶, making from LWR one of the most simple and cheap to build current reactors. According to the nuclear energy obtaining process as thermal energy in the water, two types of LWRs are basically differentiated:

⁵ The Encyclopedia of Science. http://www.daviddarling.info/encyclopedia/B/binding_energy.html

⁶ The neutron moderator is the medium used to slow down (thermalize) neutrons released from nuclear fission process (which have very high speeds) without easily absorbing them. This process is essential in a LWR to increase the fission interaction probability of the neutrons with the nuclear fuel and be able to maintain the chain reaction. The type of nuclear reactor in which most of the fission is caused by thermal (slow) neutrons is called *thermal reactor*.

- Pressurized Water Reactor (PWR):** In this type of LWR the water of the primary circuit is pressurized at $\sim 150\text{kg/cm}^2$, entering the vessel at $\sim 560\text{K}$ temperature and, after extracting the thermal heat generated by the nuclear fissions, exiting the vessel at $\sim 590\text{K}$ temperature (always as a liquid-phase). It is important to notice the presence of the pressurizer, whose function is to maintain the pressure of this subcooled primary water circuit. By using the Steam Generator (SG), the heat is transferred to a secondary water circuit that is pressurized at $\sim 60\text{kg/cm}^2$, which extracts the heat from the primary circuit by boiling at the saturation temperature of $\sim 550\text{K}$ [2]. After absorbing the heat, the secondary water circuit performs a typical Rankine cycle⁷ as happens in other common thermal plants, where the thermal energy of the generated steam is properly converted into electrical power by rotating turbine generators (see Figure 1.4).

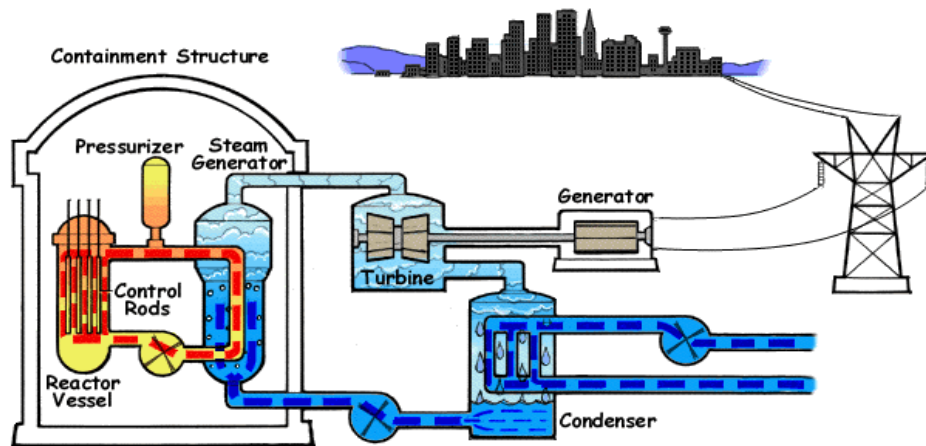


Figure 1.4. Pressurized Water Reactor outline⁸

- Boiling Water Reactor (BWR):** In this second type of LWR the water of the primary circuit is pressurized at $\sim 80\text{kg/cm}^2$, extracting the heat by boiling at its saturation temperature $\sim 570\text{K}$ [2]. No subcooled water circuit and no pressurizer are present in a BWR (the main difference compared to a PWR), so the steam generated in the new primary circuit is the one which performs the Rankine cycle and rotates the turbine generators (see Figure 1.5).

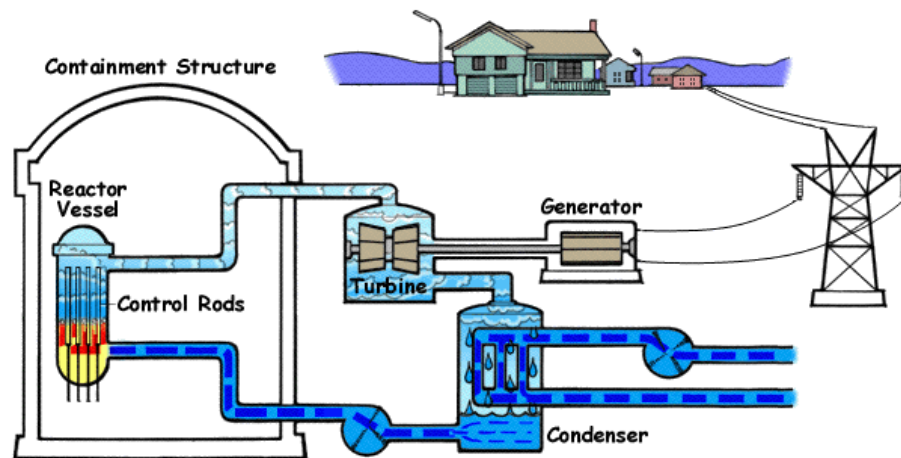


Figure 1.5. Boiling Water Reactor outline⁹

⁷ The Rankine cycle is an idealized thermodynamic cycle used for steam power plants which converts heat into work.

⁸ United States Nuclear Regulatory Commission. *The Pressurized Water Reactor (PWR)*.
<http://www.nrc.gov/reading-rm/basic-ref/students/animated-pwr.html>

Either in PWR or in BWR reactor types the **nuclear fuel** used is typically composed of Uranium Oxide (UO_2) pellets, which are a result of the manufacturing process of the nuclear fuel cycle (see Figure 1.6). First, natural Uranium ore (which contains less than 0,1% of Uranium) is extracted through conventional mining from natural deposits. This natural ore undergoes to a milling process where is chemically treated to produce a Uranium Oxide concentrate called “yellowcake” (U_3O_8 powder that contains more than 80% uranium). However, this Uranium Oxide requires an additional processing (enrichment) in order to increase the ^{235}U fissile isotope¹⁰ concentration (only 0,71% in natural Uranium) and be able to sustain a nuclear chain reaction in a LWR core. Therefore, U_3O_8 is turned into the form required by most Uranium enrichment plants, uranium hexafluoride (UF_6), and typically enriched to 3,5% - 5% ^{235}U . Finally, for its use as nuclear fuel, enriched UF_6 is converted to Uranium dioxide (UO_2) powder and sintered at high temperature into pellet form [3].

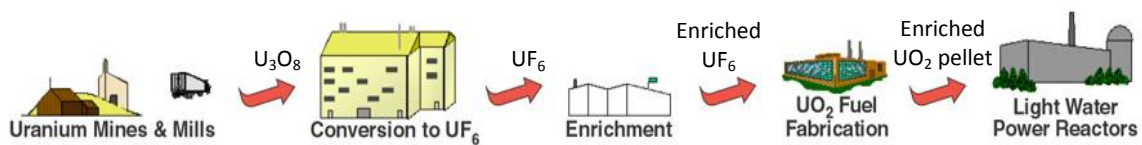


Figure 1.6. Stages of the nuclear fuel manufacturing process¹¹

Fission process of this nuclear fuel, besides being a very high density energy source, produces an important amount of fission products generated by the rupture of the fissile atom. These fission products are often unstable (radioactive) and its decay energy can be very dangerous if they are released to the environment, which forces NPPs to dispose of successive barriers against any possible radioactivity release. The first barrier in current LWRs is to contain UO_2 pellets inside a Zirconium alloy cladding to prevent radioactivity release to the water of the primary circuit (see Figure 1.7).

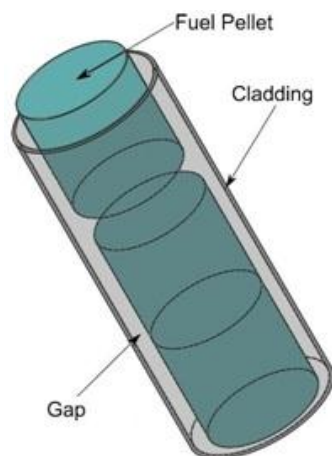


Figure 1.7. Fuel rod cladding¹²

⁹ United States Nuclear Regulatory Commission. *The Boiling Water Reactor (BWR)*. <http://www.nrc.gov/reading-rm/basic-ref/students/animated-bwr.html>

¹⁰ Isotope capable of undergoing fission as a result of the impact of slow neutrons.

¹¹ Massachusetts Institute of Technology. Mitopencourseware. <http://ocw.mit.edu>

¹² Objexx Engineering. *Nuclear Fuel Rod Finite Element Modeling*. <http://objexx.com/projects.html>

A zirconium alloy is a solution of Zirconium and other metals¹³ and is mainly used in cladding and structural components due to its corrosion resistance, its stability under radiation and temperature exposures, and its transparency to neutrons. It is also important to notice the presence of a gap between the outer surface of the fuel pellet and the inner surface of the cladding, which is typically filled with Helium gas in order to improve heat conduction from the pellet to the clad. Gap importance increases over time because the fission products accumulation and the fuel pellet swelling increase with burnup, so takes the function of confining gaseous fission products and preventing any possible pellet-cladding contact.

These fuel rods composed of fuel pellets and the surrounding Zirconium alloy are arranged into fuel assemblies, which in turn are properly joined up to configure the whole core of a LWR (see Figure 1.8). Fuel assemblies have different forms, different dimensions and are composed by a different number of fuel rods depending on the model of reactor.

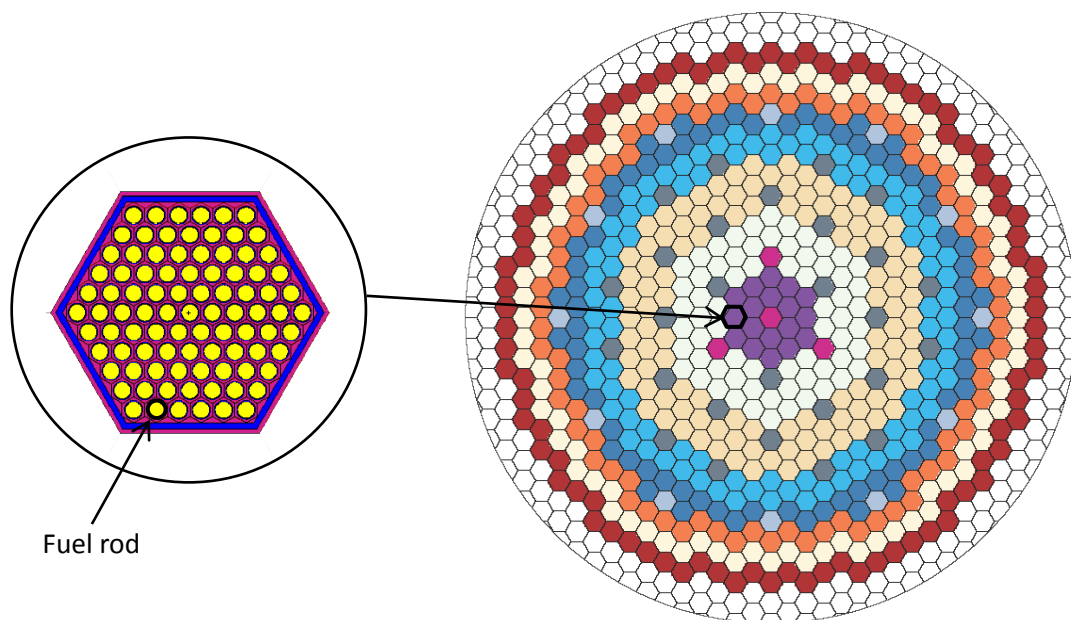


Figure 1.8. Example of a whole core cross-cut with hexagonal fuel assemblies¹⁴

1.3. Nuclear power safety challenges

The safety assessment is essential for the correct design and subsequent licensing of a NPP, and it is mainly carried out by the accomplishment of different safety analyses, which involve deterministic and probabilistic studies. Safety analyses are used to demonstrate the compliance of the safety requirements for different operating conditions and various initiating events. These identified initiating events are classified, based on the results of previous probabilistic studies, into the following three classes of events [4]:

¹³ Very common trademarks such as Zircaloy™ or Zirlo™ are included in this group, and are widely used in current LWRs.

¹⁴ Website: <http://www.whatisnuclear.com/articles/nucreactor.html>

- **Anticipated Operational Occurrences (AOO):** Include events with frequencies of occurrence equal to or greater than 10^{-2} per reactor year. These events may occur during normal operation and are not considered accidents, but they are analyzed to ensure that any possible malfunction in the NPP does not end up in accident.
- **Design Basis Accidents (DBA):** Include events with frequencies of occurrence equal to or greater than 10^{-5} per reactor year but less than 10^{-2} per reactor year. DBAs are not expected to happen in normal operation, and acceptance criteria are established to basically confirm the effectiveness of plant systems in maintaining the integrity of physical barriers against releases of radioactive material.
- **Beyond Design Basis Accidents (BDBA):** Include events with frequencies of occurrence less than 10^{-5} per reactor year. An accident management program is established for this type of accidents and the acceptance criteria are mainly focused on ensure the effectiveness of the accident management needs.

Therefore, the safety assessment must ensure no accidents that may challenge safety systems at a level much higher than expected (severe accidents), as well as ensure radioactivity containment and provide mitigation of any possible accident consequences.

1.3.1. Severe accident scenario in LWRs

One of the most important severe accidents is the fuel failure, mainly produced by the lack of adequate cooling for the decay heat generated after reactor shutdown. In an emergency shutdown of a nuclear reactor (SCRAM), all safety control rods are inserted and the fission chain is stopped, but power does not drop to zero because some radioactive isotopes (fission products) that remain from previous fissions continue to produce radiation, such as gamma rays, beta particles and alpha particles. This energy is about $\sim 7\%$ of full thermal power in normal operation [5], but still is a large heating power that must be removed as rapidly as produced; otherwise reactor core begins to heat up compromising the integrity of its components. The failure of the cooling systems that provide flow through the reactor core cause an accident called Loss-of-Coolant Accident (LOCA).

When a LOCA occurs core temperature increases fast, achieving the rapid oxidation temperature of zirconium alloy (1470K) if the decay heat is not successfully cooled during the first 24-48 hours [6]. Then, the exothermic oxidation reaction takes place, resulting in a local uncontrolled temperature rise and starting UO_2 dissolution from 2030K. This becomes a severe accident scenario because fission products are not contained inside the cladding, leading to a radiation release, the important amount of Hydrogen produced by the Zirconium alloy oxidation reaction might cause an explosion if a high concentration level is reached, and the change in the fuel geometry by the dissociation of UO_2 might lead to an uncontrolled criticality.

1.3.2. Safety weaknesses in current LWRs

In order to prevent any type of accidents and increase safety in current and future NPPs, since the early 1970s nuclear industry has been widely using a methodology called Probabilistic Safety Assessment (PSA) [7]. This probabilistic point of view understands the *risk* of accident as a weighing of happening probability and damage consequences, and it is basically focused on minimalizing this *risk* by working on event tree analysis. This is done by defining concrete initiating events that can lead to an interruption of normal operation of the NPP, and analyzing the fault tree considering the mitigation systems available. PSA helps to add redundancy, isolation and independence¹⁵ on process components and safety systems if needed, in order to comply with the single-failure criterion¹⁶. By this methodology, a big step forward in safety has been done (even beyond the nuclear field).

However, after Fukushima Daiichi (BWR) accident, the importance of melt down safety proof becomes more pronounced. In Fukushima's reactor the core partially melted down because of a long-term loss of emergency core cooling (extended station blackout), caused by a loss of the off-site electrical power and emergency on-site electrical power after the tsunami. In addition, the large oxidation of the zirconium cladding led to a Hydrogen explosion, blowing off the roof and cladding on the top part of the building [9].

Although current PSA fix a core damage frequency value in $\sim 10^{-6}$ per reactor and year¹⁷ (which means almost 2.300 years between two core damage accidents in the world considering 436 operative reactors¹⁸); Fukushima accident happened only 32 years after Three Mile Island (PWR) incident, the first meltdown of a major commercial power reactor. The need of a large backup power supply during shutdown, the failure of important cooling systems, DBA equipment malfunction or unexpected BDBA highlight some worrying inherent weaknesses in current LWRs that must be taken into account. They could be identified as follows [10]:

- Large amounts of zirconium in the clad that can react with steam at high temperature and produce hydrogen in the exothermic oxidation reaction.
- Very low conductivity of the UO₂ fuel that may cause high temperatures in the fuel, impeding its cooling during off-normal situations.
- Fission fragments only loosely bound to the solid oxide fuel, which can be dispersed in the coolant upon clad failure.

Fukushima Daiichi accident may now increase inherent safety investigation, pushing for a more aggressive adoption of an alternative fuel, resistant to meltdown and lacking in these weaknesses.

¹⁵ An element is *redundant* if it contains backups to do its work if it fails. Two elements are *independent* if the chances of one failing are not linked in any way to the chances of the other failing. Finally, *isolation* refers to physically separating them and shielding them from each other [8].

¹⁶ The single-failure criterion: Requirement applied to a system such that it must be capable of performing its task in the presence of any single failure

¹⁷ Consejo de Seguridad Nuclear (CSN). *Módulo 1: Fundamento de Emergencias Nucleares*.

¹⁸ European Nuclear Society. *Nuclear power plants world-wide*. March 2012. www.euronuclear.org

1.3.3. Meltdown resistant fuel and thesis purpose

Summarizing previously section, oxide fuels in Zirconium cladding used in current LWRs are mainly vulnerable to loss-of-coolant conditions because of its chemically active cladding, low conductivity of the fuel and loosely bound fission products. Hence, a fuel gathering next properties could be a solution to prevent meltdown and to improve these inherent weaknesses [10]:

- A clad made with a less reactive material (e.g. Stainless steel or a non-metallic material).
- A fuel with higher conductivity (e.g. Uranium carbide or Nitride fuel).
- The ability to retain fission products tightly bound to its matrix (e.g. coated particle fuel).

Although alternative fuels with these properties will be initially more expensive to manufacture than current fuels, they could increase protection to the public, which is one of the main targets of nuclear industry. As explained in Chapter 2.1, Fully Ceramic Microencapsulated fuel (FCM fuel) gathers these properties, and it is the fuel this project analyzes.

This thesis is mainly focused on obtaining conclusions concerning neutronics safety aspects of FCM fuel in LWRs, concretely for a PWR type, and analyze whether FCM fuel could be a strong alternative to current UO_2 fuel in this type of reactors. To perform this analysis the SERPENT code has been used, which is a very useful computational tool but still in development. In this sense, thesis purpose also involves obtaining interesting conclusions on how SERPENT code works with the geometry and conditions described is the project.

Chapter 2

Theoretical background

2.1. FCM fuel

FCM fuel is an innovated concept that builds on the tested Tristructural-Isotropic (TRISO) fuel technology to develop a new fuel form that can be used in multiple reactors. FCM fuel consists of amounts of TRISO fuel particles embedded inside a dense non-fuel SiC matrix that is sintered with nanoparticles of SiC [11]. The compacted fuel can be manufactured in a pellet form to be placed in cladding tubes and fuel assemblies (e.g. for its use in LWRs), as well as in other types of compacts or pebbles.

2.1.1. FCM fuel description

TRISO particles used in FCM fuel are a type of micro spherical coated particle fuel, which has an external diameter in the range of 500 - 1000 μm and consists on a fuel kernel, coated with four layers of three isotropic materials (see Figure 2.1): A porous Pyrolytic Carbon (PyC) buffer layer, followed by a dense inner PyC layer (IPyC), followed by a ceramic SiC layer, followed by a last dense outer PyC layer (OPyC) [10].

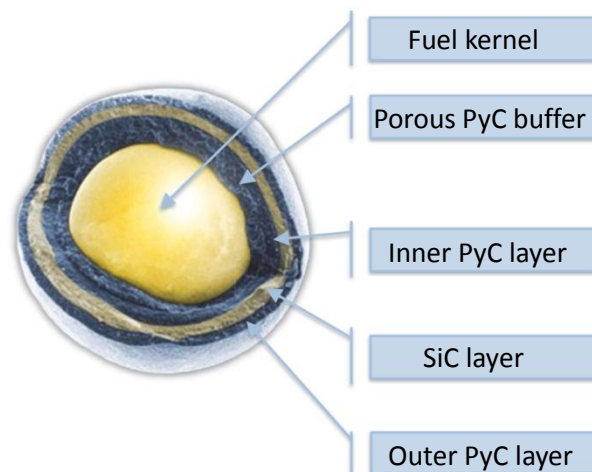


Figure 2.1. TRISO particle geometry [12]

Because of the presence of these coating layers and the SiC matrix around TRISO particles, it is more difficult to achieve high heavy metal density in the FCM fuel pellet compared to the ordinary UO₂ fuel pellet. Therefore, the use of TRISO fuel in LWRs will demand higher enrichments than current oxide fuels, and the coating thicknesses will be required to be as reduced as possible while also configuring a good fission product barrier. TRISO particle geometry, materials and functions of the various layers are described below [12, 13]:

Fuel kernel: It is a fuel sphere that provides energy and neutrons. Kernel diameter is variable, typically in the range of 350 - 700 μm, and may contain different alternatives of fissile fuel material, such as UO₂ (oxide fuel), UCO (carbide fuel) or UN (nitrate fuel). As introduced before, kernel increases its swelling and generates radioactive fission products throughout burnup, besides producing energy and neutrons. The coating layers design is determined according to these fission products, taking into account that solid metallic species chemically interact with the coatings and gaseous species causes stresses in them. Fuel enrichments vary from 8% to 20% depending on the kernel diameter, the fuel type and other power rating considerations.

Porous PyC buffer: It is a low-density PyC layer, which is in direct contact with the kernel. The aim of this buffer is to attenuate fission fragment recoil atoms ejected from the fuel kernel, to provide volume for fission gases and to accommodate kernel swelling by mechanically isolating it from the structural coating layers. Its density is in the range of 0.9 – 1.1 g/cm³ and its thickness is typically ~50 μm.

Inner PyC layer: It is the first of the three structural layers, the first barrier against the fission gas release and a protection for the surrounding SiC layer by stopping many fission products that might chemically attack it. It is practically impenetrable for Krypton and Xenon, but does not stop Silver and is pervious for Cesium and Strontium at higher than normal operation temperatures [14]. In addition, it provides structural support for the SiC layer and prevents reaction between the kernel and Cl containing materials, which are sometimes released during manufacture. Its density is in the range of 1.8 – 2.0 g/cm³ and its thickness is typically ~35 μm.

SiC layer: It is the main bearing element of the TRISO particle, and also enhances the mechanical stability of the pressure vessel to retain gaseous fission products by having a higher mechanical strength than the dense PyC layers. The SiC layer is the major containment barrier for fission products release by providing retention for all fission products under normal operation, leading to be very important to remain this layer intact. Its density is ~3.20 g/cm³ and layer's thickness is typically ~35 μm.

SiC is an excellent material in terms of material properties, is highly stable under fast neutron irradiation, has excellent oxidation resistance, low irradiation swelling and it is manufactured on an industrial scale at a reasonable cost. However, above 1870K its corrosion is increased, becoming porous to Cesium, Strontium and Silver [13].

Outer PyC layer: It provides structural support and gives to the particle a higher temperature capability by preventing the vaporization of the SiC layer. It also protects the SiC from any possible mechanical damage during fuel manufacture, is an additional barrier for gaseous fission products in case of rupture of the SiC layer and provide bonding surface for compacting. As well as IPyC layer, its density is in the range of $1.8 - 2.0 \text{ g/cm}^3$, but a lower thickness is typically needed, about $\sim 20 \mu\text{m}$.

OPyC layer is also important to deflect a possible crack in the SiC matrix around the particle and prevent fission product release, as shown in Figure 2.2 and Figure 2.3.

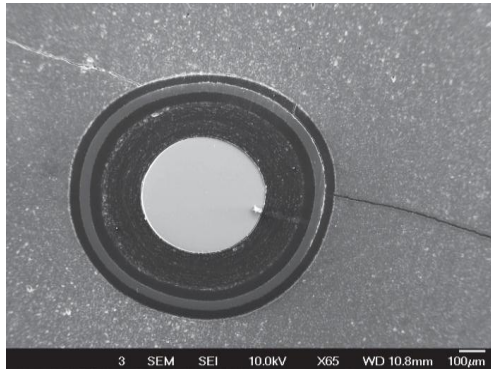


Figure 2.2. SiC crack with OPyC layer [12]

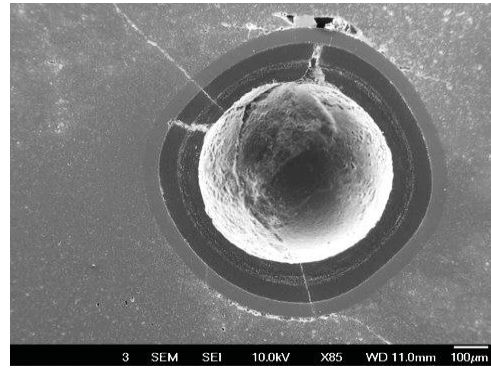


Figure 2.3. SiC crack without OPyC layer [12]

TRISO particles are over coated with a resinated graphite powder to prevent contact between them during formation of the FCM compact, which is fabricated by composing the SiC matrix around TRISO particles using a specific liquid-phase sintering process called *Nano-Infiltration and Transient Eutectic-phase* (NITE). A SiC nanopowder (40nm particle size) is used to make up the matrix because it provides very high reaction surface area, achieving a theoretical density of the matrix in the range of 97 - 98%. This SiC nanopowder is mixed with minute amounts of oxide additives ($\sim 5\%$ of Y_2O_3 and Al_2O_3 used as sintering aids) and mixed with TRISO particles. An important consideration is that oxide additives must be completely dispersed in the SiC nanopowder mixture, in order to achieve ideal microstructures [12].

After the mixing process it undergoes hot pressing to fabricate the FCM pellet (see Figure 2.4). Typical hot-press parameters are 1h time, 1850°C temperature and 15-20 MPa pressure [15]. TRISO fuel is not expected to be damaged during the compaction process under these conditions.



Figure 2.4. FCM pellet with TRISO loading [12]

2.1.2. FCM fuel advantages

Thanks to FCM fuel geometry and the properties of its materials, the use of FCM fuel could improve the main three LWRs inherent weaknesses suggested before; achieving a new behavior that would enhance safety during normal and off-normal operation and representing three very strong levels of defense-in-depth at a fuel level that current LWRs do not have:

- The **cladding work conditions are improved**, and the use of a non-metallic material for the clad is even possible. The stainless steel cladding alternative was used in the past but nowadays Zirconium alloys are used in most reactors. Although stainless steel is much less prone to react with steam than Zirconium alloys, these latter have a very low neutron absorption cross section and highly resistant to corrosion under operating conditions, which are essential properties for a cladding material. In addition, and besides being an advantage regarding to the neutronics, this low neutron absorption property becomes an important economical factor since it allows the use of lower enriched fuels for similar operating cycles.

By using FCM fuel, fission gas products are contained inside the TRISO particles and not released to the gap, which leads to not increase internal pressure of the clad, reducing mechanical stresses and eliminating corrosion cracking at the inner surface of the cladding. These new work conditions also allow increasing pellet diameter by reducing pellet-to-clad gap, which is very important to reduce the fuel enrichment needed. Under these new conditions, cladding will creep down at the beginning of fuel operation because of coolant pressure, but the absence of fission gas releases will prevent gap reappearance, improving its thermal conductivity and decreasing mechanical demands [11]. However, the use of SiC instead of metallic Zirconium alloys for cladding could be possible due to this new cladding mechanical behavior, having a higher resistance to creep and avoiding any safety problem related to the Zirconium oxidation reaction.

- The thermal conductivity of the SiC matrix is on the order of 30 times higher than that of uranium oxide [15]. Hence, **the maximum temperature of the FCM fuel pellet is significantly lower than that for the UO₂ pellet**, only 200K above coolant temperature (see Figure 2.5), reducing its chance of failure.

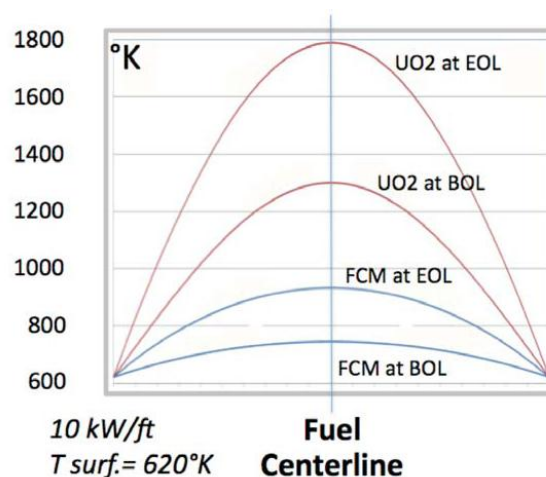


Figure 2.5. Temperature distribution over pellet section [12]

In addition, SiC dissociates at 2730K whereas Zirconium fast oxidation starts from 1470K and UO₂ fuel dissolution from 2030K [15]. By having this higher dissociation temperature, FCM fuel allows an enough enthalpy margin to start severe damage for FCM fuel, enhancing the safety of a nuclear reactor.

- Last but not least, **fission products are tightly bound** to FCM fuel, as a result of composing three very strong barriers against the release of fission products to the coolant: 1) The coating layers around the fuel kernel, 2) the SiC matrix around the particles and 3) the cladding around the fuel rod. This is a very important difference between the use of FCM fuel and current UO₂ fuel pellet configuration, where Zirconium alloy clad is the only barrier against fission products release to the water of the primary circuit.

2.1.3. Technological landscape

In the 1960s ceramic coated particle fuel was developed for ROVER/NERVA nuclear rockets, as well as used in large graphite HTRs as German AVR Reactor (PBR) in order to develop pebble fuel¹⁹. The design of the coated particle fuel has changed since the early stages in the 1960s. Although several variations of coating designs have been produced, only the next three designs have been used in HTRs (chronologically ordered): laminar²⁰ (AVR Reactor), BISO²¹ and finally the explained TRISO design [10]. In the 1980s, already in the form of TRISO particles, ceramic coated particle fuel was developed for large and modular HTGC systems such as German THTR-300, achieving its record performance in the 2000s [11, 13].

In light of this historical development, TRISO particle technology is not considered a new concept and its manufacturing is well established. In the proper SiC matrix, TRISO fuel seems to be an alternative for oxide fuels in LWRs because of working at lower operation temperatures than in HTRs, the original type of reactor TRISO fuel was designed for.

2.2. Safety parameters

The aim of this second section of the theoretical background is to introduce the safety parameters will be calculated further on in order to analyze safety aspects of the FCM fuel behavior in current PWRs [16, 17].

2.2.1. Fuel Temperature Coefficient (Nuclear Doppler Effect)

Neutrons, which are born in the fast region (>0,5MeV) with approximately 2MeV energy, interact with the moderator and reduce their energy until a thermal energy (~0,025eV), where they are able to undergo fission (see Figure 2.6).

¹⁹ Spherical fuel elements made of pyrolytic graphite containing thousands of TRISO particles.

²⁰ Type of micro particle fuel coated with a single PyC layer.

²¹ Bistructural-ISOTropic. Type of micro particle fuel coated with a porous PyC layer and a dense PyC layer.

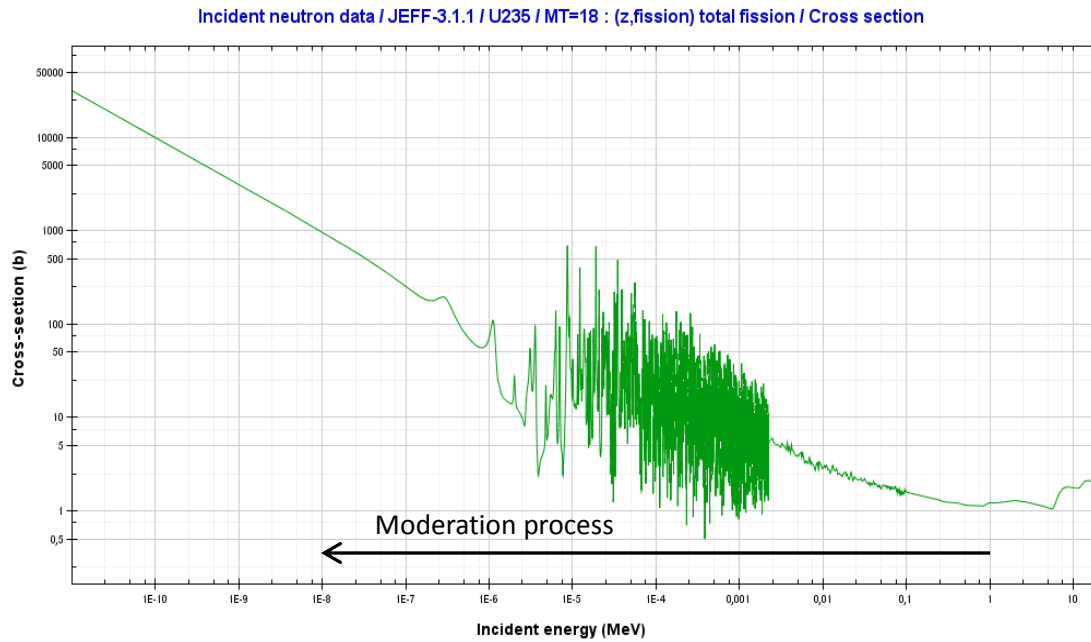


Figure 2.6. ^{235}U fission cross section²²

However, heavy metal nuclides (mainly ^{238}U and ^{240}Pu) exhibit a strong resonance behavior for neutron absorption in the energy range between the fast region and the thermal region. Although the width of the absorption resonances is very small, the probability of absorption is very high (see Figure 2.7), even higher than the ^{235}U fission probability for the same neutron energy, leading to an important neutron absorption rate during the moderation process.

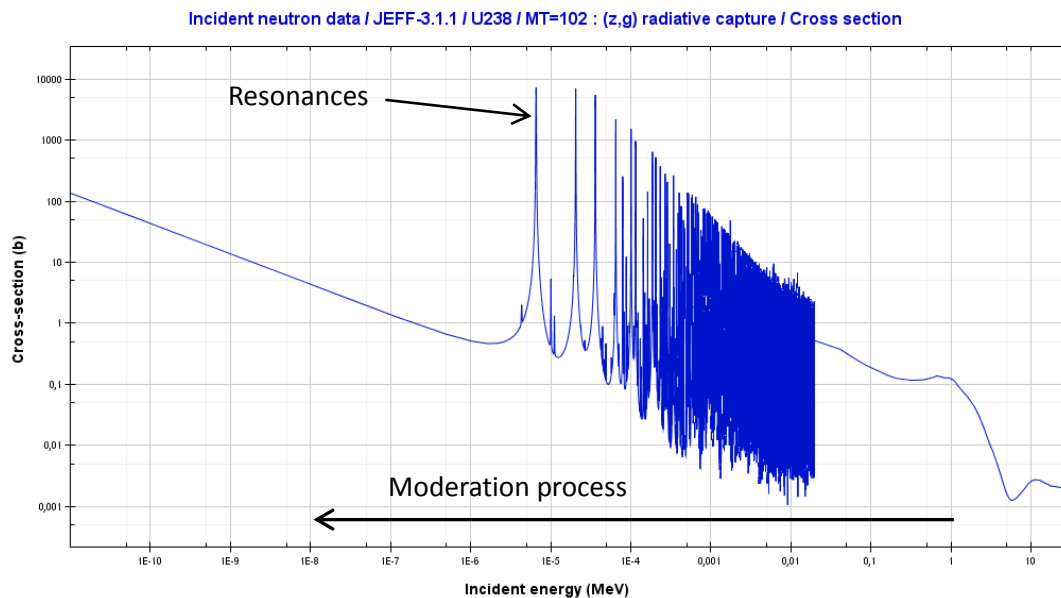


Figure 2.7. ^{238}U absorption resonances

²² Janis 3.4. OECD/NEA Data Bank, 2012. <http://www.oecd-nea.org/janis/>
All cross section graphics of the project are obtained from this source.

When fuel temperature increases, the thermal motion of the heavy metal nuclides increases as well and the range of relative velocities between neutron and nuclides becomes wider, leading to a more flat but broader resonance absorption area. Although the total resonance absorption area remains constant because the number of nuclides does not change, the result of a temperature rise is an increase in the neutron resonant absorption, fortunately for safety interests.

The Fuel Temperature Coefficient (FTC or α_{fuel}) measures the Doppler Effect by the change on reactivity caused by a change in fuel temperature. It is defined in equation (2.1):

$$FTC \left[\frac{pcm}{K} \right] = \frac{\partial \rho}{\partial T_{fuel}} \cdot 10^5 \quad (2.1)$$

Where reactivity (ρ) is related to the effective multiplication factor (k_{eff})²³ as follows:

$$\rho = \frac{k_{eff} - 1}{k_{eff}} \quad (2.2)$$

Of course, FTC is desired to be negative to stabilize core behavior when a change in reactivity occurs. However, a very strong negative FTC is unwanted because when core temperature decreases, for example after reactor shut down, an increase in reactivity is introduced.

The most important aspect of the Nuclear Doppler Effect is that it reacts immediately after a change in the fuel temperature. This means that if a large positive reactivity increase occurs and power increases suddenly (within fractions of a second), the first mechanism that will start adding negative feedback will be the Doppler Effect while other temperature coefficients, such as the moderator coefficient explained below, will not affect the power that rapidly.

In addition, the FTC hardly depends on the composition of the fuel rods, so this parameter must be studied carefully for a feasible replacement of the UO₂ fuel with FCM fuel.

2.2.2. Moderator Temperature Coefficient

In PWRs, when water temperature increases, its thermal cross sections change and its physical density decreases because of the thermal expansion. This change in the water density reduces the amount of moderator per unit volume, which leads to a lack in the moderation process because of reducing the scatter probability, which in turn moves the neutron spectrum toward higher energies. This change in the neutron flux energies reduces the fission probability with ²³⁵U and increases the parasitic absorptions of ²³⁸U, especially in the range where the absorption cross section does not follow the $1/v$ dependence, tending to keep the MTC negative (see Figure 2.8).

²³ k_{eff} is the ratio of the number of neutrons in one generation to the number of neutrons in the previous generation.

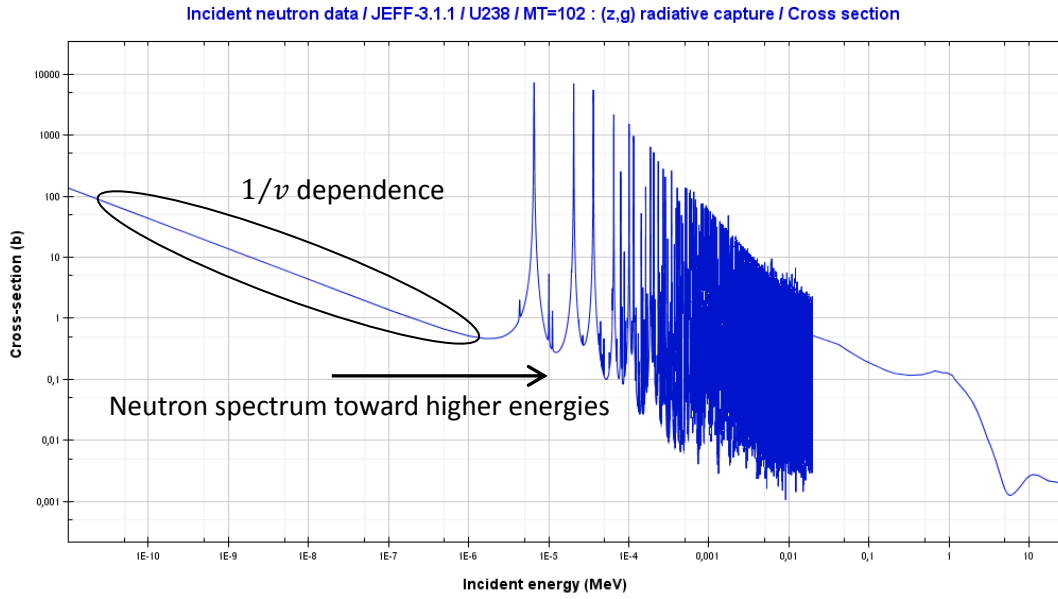


Figure 2.8. $1/v$ dependence of the ^{238}U absorption cross section

The Moderator Temperature Coefficient (MTC or α_{mod}) measures the change on reactivity caused by a change in moderator temperature. It is defined in equation (2.3):

$$MTC \left[\frac{pcm}{K} \right] = \frac{\partial \rho}{\partial T_{mod}} \cdot 10^5 \quad (2.3)$$

This coefficient is much stronger in fluid moderators than in solid ones, so becomes very important in the safety analysis of a PWR.

It must be taken into account that MTC can be positive or negative depending on the moderator to fuel ratio and the presence of highly absorbents in the water, such as boron. For high concentrations of boron, a temperature increase in the water also reduces the amount of boron per unit volume, reducing its absorption capability and might leading to a total positive MTC coefficient.

2.2.3. Void coefficient

Although the BWR reactor is not studied in this thesis, it is also important to notice that in this type of reactor the MTC coefficient becomes useless because a power increase involves a change in the void fraction and not a change in the water temperature as in PWRs, i.e. the heat rise transforms liquid water into steam phase. Hence, another safety parameter comes into the picture: the **Void Coefficient (α_v)**, which defines a rate of change in the reactivity resulting of the formation of steam after a power level increase (2.4).

$$\alpha_v [pcm] = \frac{\partial \rho}{\partial x} \cdot 10^5 \quad (2.4)$$

Where (x) is the water void fraction inside the core.

As well as the MTC, α_V is desired to be negative in order to operate the NPP in safety conditions. In current BWRs, as in most of the world's operating power reactors, water circuit acts as both moderator and coolant. Hence, their α_V value is negative because the transformation of liquid water into steam leads to an important decrease of the moderation, reducing the reactivity and thus the reactor power.

However, in other kind of reactors such as the RBMK (Chernobyl), the NPP is operated with a positive void coefficient. A positive α_V increases reactivity when the void fraction increases, increasing power and leading to more steam generation, further increasing the void fraction. This unstable behavior can produce an uncontrollable power increase if it is not properly regulated, leading to a severe accident such as in Chernobyl unit 4 [18].

2.2.4. Void worth

The coolant void worth (CVR) expresses the reactivity introduced when the coolant of the reactor is removed. It can be calculated according to equation (2.5):

$$CVR [pcm] = (k_{eff (without\ coolant)} - k_{eff (with\ coolant)}) \cdot 10^5 \quad (2.5)$$

This safety parameter is tightly related to the void coefficient and it is very useful to describe the reactor behavior during a loss-of-coolant accident (LOCA), where off-normal conditions might lead to an increase of reactivity besides losing the capability of heat removal. This happens because the lack of moderation moves the neutron spectrum towards higher energies, increasing fission probability of transuranic elements (TRU)²⁴, which have higher fission probabilities at this energy range. As happens for the MTC, CVR is strongly dependent on the boron concentration and burnup, which is highly related to the amount of TRU generated.

²⁴ TRU are radionuclides that have atomic numbers greater than that of uranium (92). All of them are radioactive nuclides and are mainly produced in nuclear reactors by neutron capture, being generated as long as fuel burnup increases.

Chapter 3

Methodology

This thesis is focused on checking the behavior of the FCM fuel inside a PWR by analyzing one of the main important aspects in the nuclear field: the neutronics within its core. In order to perform this analysis, three basic elements are needed: a mathematical model for the transport of subatomic particles through matter, a numerical method capable to solve its equations and a computational tool to execute the methodology.

The aim of this section is to present these elements, starting from the Boltzmann equation, a mathematical model used to study the non-equilibrium behavior of a collection of particles and commonly applied to neutronics analysis. After a comparison between some methodologies and computational codes, the Monte Carlo method will be introduced, a methodology capable to solve an integral form of the Boltzmann equation even in complex geometries, basically by the application of the laws of probability and statistics to the neutron transport field [19]. Finally, the SERPENT code will be described, the simulation tool used in this thesis to analyze the behavior of FCM fuel in PWRs.

3.1. Neutron transport

The neutron transport mathematics used as background in the Monte Carlo method will be introduced below, by describing neutron definition, Boltzmann neutron transport equation and the final solution for the Monte Carlo method.

3.1.1. Neutron definition

Neutron can be completely defined by designating its location r , its direction of travel Ω and its energy E , at time t . Apart from the time variable, coordinates from a six-dimensional phase space are needed to fully describe the particle; three position, two direction and one energy variable (see Figure 3.1).

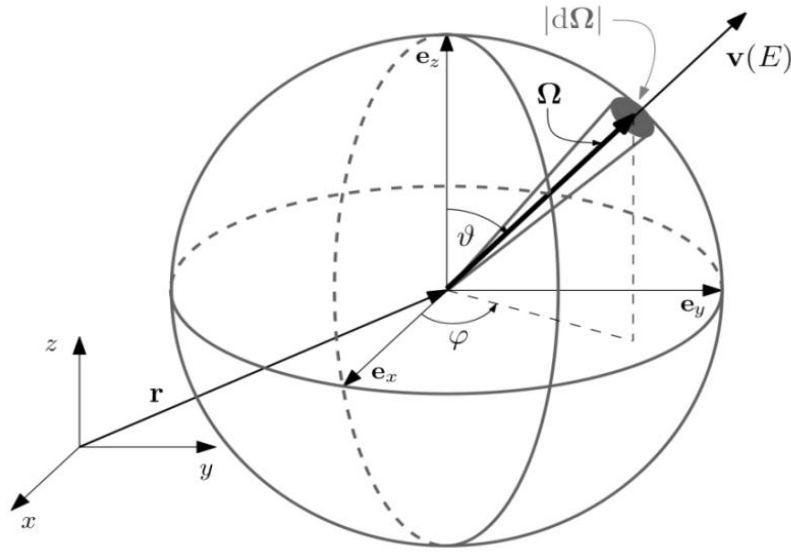


Figure 3.1. Neutron's phase space [20]

Where,

- $r = (x, y, z)$ specifies the position of the particle in the domain $V \subset R^3$
- Ω specifies the direction of motion (a vector from point r to the surface described by a unit sphere centered at r), measured by its polar angle ϑ and its azimuthal angle φ .
- $E = \frac{1}{2}mv^2$, specifies neutron energy corresponding to its speed v (m is the mass of neutron).

After specification of one neutron, it is possible to define the basic physical quantity used to describe a population of neutrons, the *neutron angular density* $N(r, \Omega, E, t)$. However, it is of interest to define the physical variables that represent the motion of this population of neutrons, which will be used in the neutron transport equation. In this sense, two magnitudes come into the picture:

- The **angular flux** $\psi(r, \Omega, E, t)$, defined as the motion of a population of neutrons located in a unit volume, traveling in any direction from a unit solid angle, with energies within a unit range, per unit time.

$$\psi(r, \Omega, E, t) = N(r, \Omega, E, t) \cdot v(E) \quad (3.1)$$

Where,

- N is the density of neutrons in volume dr about r , traveling in direction $d\Omega$ about Ω , with energy dE about E and at time dt about t .
- v is neutron's speed (corresponding to neutron's energy E).

- The **total flux or scalar flux** $\phi(r, E, t)$, which is defined as the integral of the angular flux over the entire solid angle. Hence, flux represents the motion of a population of neutrons located in unit volume, with energies within a unit range, per unit time, regardless of their flight direction:

$$\phi(r, E, t) = \int_{4\pi} \psi(r, \Omega, E, t) \cdot d\Omega \quad (3.2)$$

Where 4π is the entire solid angle.

3.1.2. Neutron transport equation

The neutron transport equation is derived from the fundamental principle of conservation of neutrons within an arbitrary element of the neutron's phase-space shown before. In this phase-space the change of neutron density must be the difference between the gain rate and the loss rate:

$$\frac{\partial N(r, \Omega, E, t)}{\partial t} = \text{gain}(r, \Omega, E, t) - \text{loss}(r, \Omega, E, t) \quad (3.3)$$

The transport equation is explained below (3.4) in terms of angular flux [21]:

$$\begin{aligned} \frac{1}{v(E)} \frac{\partial \psi(r, \Omega, E, t)}{\partial t} = & S(r, E, \Omega, t) - \Omega \cdot \nabla \psi(r, \Omega, E, t) - \Sigma_t(r, E) \psi(r, \Omega, E, t) + \\ & + \int_{4\pi} \int_0^\infty \Sigma_s(r, \Omega' \rightarrow \Omega, E' \rightarrow E, t) \psi(r, \Omega', E', t) d\Omega' dE' + \end{aligned} \quad (3.4)$$

Where,

$$\frac{1}{v(E)} \frac{\partial \psi(r, \Omega, E, t)}{\partial t}$$

- Time rate of change of neutron density.

$$S(r, E, \Omega, t)$$

- External source that does not depend on ψ .

$$\Omega \cdot \nabla \psi(r, \Omega, E, t) = \Omega_x \frac{\partial \psi(r, \Omega, E, t)}{\partial x} + \Omega_y \frac{\partial \psi(r, \Omega, E, t)}{\partial y} + \Omega_z \frac{\partial \psi(r, \Omega, E, t)}{\partial z}$$

- Leakage out of the elementary volume in direction Ω .

$$\Sigma_t \psi(r, \Omega, E, t)$$

- Neutrons lost from the elementary phase-space volume due to an interaction. Σ_t is the *total macroscopic cross-section*, which does not depend on the angle of hitting due to the assumption of isotropic core.

$$\int_{4\pi} \int_0^{\infty} \Sigma_s(r, \Omega' \rightarrow \Omega, E' \rightarrow E, t) \psi(r, \Omega', E', t) d\Omega' dE'$$

- Neutrons moving in an arbitrary direction with an arbitrary speed (r, Ω', E', t) that scatter into the elementary phase-space volume (r, Ω, E, t) . In this case Σ_s is the *differential scattering cross section*, which is the cross section for scattering into the volume of interest from the energy E' to E and from the direction Ω' to Ω .

Finally, next assumptions must be taken into account to make the equation (3.4) adequate to define neutron transport [22]:

- A static, homogeneous and isotropic medium is considered.
- Next event depends only on current (r, v, E) , not on previous events.
- The neutron density is considered sufficiently low to neglect neutron-neutron collisions, simplifying the neutron transport equation by making it linear.
- Relativistic effects are neglected.
- No forces are applied to the particles (i.e. straight flight between events).
- Material properties are not affected by particle reactions.

Being a statistical equation, the mathematical model of neutron transport describes only the average behavior of the neutron population; so the Monte Carlo method (by modeling the motion of individual neutrons) might produce a different answer from average behavior in local regions.

3.1.3. Integral form of the transport equation and final solution

The desired form of the Boltzmann transport equation is obtained by integrating the angular flux $\psi(r, \Omega, E, t)$ over all phase space as shown in equation (3.5) [21]:

$$\begin{aligned} \psi(r, \Omega, E, t) = & \int_0^{\infty} e^{-\beta} \left[\iint \Sigma_s(r - s\Omega; \Omega', E' \rightarrow \Omega, E) \psi(r - s\Omega, \Omega', E', t - s/v) d\Omega' dE' \right] ds + \\ & + \int_0^{\infty} e^{-\beta} S(r - s\Omega, \Omega, E, t - s/v) ds \end{aligned} \quad (3.5)$$

Where,

$$\beta = \int_0^s \Sigma_t(r - s'\Omega, E) ds' \quad (3.6)$$

- β is the optical thickness.

$$r = r' + s\Omega \quad (3.7)$$

- s is the coordinate along a line in direction Ω through r (see Figure 3.2).

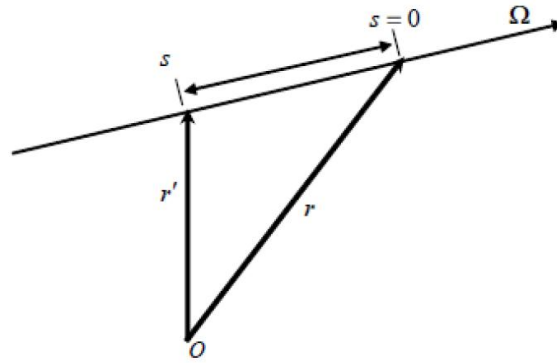


Figure 3.2. Neutron motion along Ω [23]

By this integral equation, the angular flux at an elementary phase-space volume point can be expressed as integrals over all sources and neutron flight paths that lead to that concrete phase-space conditions.

In operator notation, the integral equation can be written as:

$$\psi = \mathbf{K}\psi + S' \quad (3.8)$$

Where,

- \mathbf{K} is the integral operator, which represents all collided neutrons
- S' is the attenuated source, which represents no collided neutrons.

Finally, it is possible to obtain a solution for this equation by defining the following series:

$$\psi_0 = S' , \quad \psi_1 = \mathbf{K}\psi_0 , \quad \psi_2 = \mathbf{K}\psi_1 , \quad \dots , \quad \psi_{n+1} = \mathbf{K}\psi_n \quad (3.9)$$

Where,

- ψ_0 is the angular flux that no collides before arriving at the requested volume.
- ψ_1 is the angular flux that collides once before arriving at the requested volume.
- ψ_2 is the angular flux that collides twice before arriving at the requested volume, etc.

When series converges, a von Neumann series solution is obtained (3.10):

$$\psi = \sum_{n=0}^{\infty} \psi_n \quad (3.10)$$

The Monte Carlo method provides estimations for ψ_0, ψ_1, \dots by tracking the source particles that have undergone no collisions, one collision, etc.; thus estimating a von Neumann series solution to the integral formulation of Boltzmann transport equation.

3.2. Simulation tools

The neutron transport calculation can be carried out by various methodologies and by using different types of simulation tools that define the geometry and materials properties of the system. Although each code has its particular methodology, two big differentiated groups of computer codes are used in neutron transport calculation: the deterministic codes and probabilistic codes.

3.2.1. Deterministic codes

Deterministic codes are characterized by analytically solving the neutron transport equations. Many codes such as PARTISN, PERTRAN, DENOVO, DRAGON or ATTILA are included in this group [24] and use different methods to solve the equations (e.g. ATTILA uses the Finite Element Method (FEM) [25]); but not probabilistic methods as Monte Carlo. One advantage of these analytically procedures is that neutron fluxes, reaction rates and other responses are calculated everywhere in the system, which allows not needing additional runs in case of requiring more information from the obtained solution. In addition, low computing resources are required to run the calculation (although a large disc space is needed to store all the information) and a short computer time is needed to find the solutions [26].

However, deterministic codes use analytically procedures and becomes necessary to approximate complex geometries by structured meshes (such as rectangular or cylindrical meshes), which could lead to a not accurate geometry definition and significant errors in results. Furthermore, neutron energy and angular direction are discretized to run the calculation and be able to solve neutron transport equations, moving neutron energy and direction away from its continuous nature [27].

3.2.2. Probabilistic codes

On the other hand, probabilistic codes use a stochastic process, such as the Monte Carlo method, instead of using analytically processes to obtain the desired solution. Thanks to this methodology, the use of a simplified structured mesh to define the geometry is not necessary and complex geometries can be modeled accurately, which is an important advantage compared to deterministic codes. Moreover, neutron energy and direction are associated to probability distribution functions and random numbers, allowing a more accurate resolution for these continuous magnitudes. However, responses are not obtained everywhere in the system but in pre-selected locations [27], and larger computing resources are needed to run the probabilistic simulations, such as computational memory, which increase calculation time.

MCNP5/MCNPX, SERPENT, MONACO/MAVRIC, TRIPOLI, VIM or TART are some examples of codes included in this group [28] although they have some differences regarding to the methodologies they work with. Some codes (e.g. TART code) use a *dynamic method* and other codes (e.g. MCNP or SERPENT codes) use an *alpha static method* to carry out the calculation, both usually producing accurate answers.

The *dynamic method* is a time dependent calculation where the neutron population is allowed to grow over a period of time, even far away from criticality, where loss terms and source terms of the neutron transport equation are proportional to neutron flux. On the other hand, *static methods* are characterized by starting from an arbitrary source distribution and, generation by generation, making the system critical (i.e. equalizing neutron production and neutron loss) [29]. For the Monte Carlo method, one of the methodologies used to simulate this stationary self-sustaining chain reaction is the *k-eigenvalue method*, where criticality is achieved every cycle by artificially modifying the neutron transport equation dividing the source term by the k_{eff} -eigenvalue in order to balance source and loss terms [30].

Due to this procedure, the static codes become restricted only to systems that are very close to criticality, such as the current PWRs this thesis deals with, which makes them a good option for this project. The SERPENT probabilistic code based on the Monte Carlo method is the simulation tool used in this thesis, so both methodology and code characteristics will be explained in this section.

3.3. The Monte Carlo Method

The Monte Carlo method is a technique of numerical analysis based on the use of sequences of random numbers to obtain sample values for the problem variables, which are obtained by using probability distributions for such variables [21]. Because of this random sequence of physical processes, Monte Carlo solutions have less truncation errors than deterministic methods, but do have stochastic uncertainties in the solution that must be taken into account [31]. The solution obtained for the integral transport equation by using the Monte Carlo method is calculated by analyzing the results from sample values and the estimates of these uncertainties.

The Monte Carlo method solves neutron transport problems by modeling the particle flight paths and the various interactions between neutrons and materials. The simulation of this path is called a *random walk*, and can be understood as a mathematical realization of one of the physically possible paths that a neutron could follow through the material. In this random walk neutron will interact with material nuclei in one of three ways: *scattering*, *fission* or *absorption*. The simulation of these interactions is possible by evaluating the random variables associated to these physical processes, producing a set of neutron collision points as well as information about its consequences. The SERPENT code used in this thesis performs two different types of Monte Carlo estimations: analog and implicit estimations, which are described below.

3.3.1. The analog Monte Carlo estimation

In this type of estimation, Monte Carlo method simulates neutron “history”, from birth to death. As shown in Figure 3.3, the neutron is created and initialized with a starting location, direction and energy; which are randomly sampled from specified probability distributions. Afterwards, the length of free straight flight is also randomly sampled from the interaction

probability density function specified by the material properties, defining a collision location. The type of collision and the collision properties are sampled in accordance with the cross sections from the appropriate data library, obtaining the latter information:

- Scattering: Position of the collision and new velocity of neutron are obtained.
- Fission: Chain terminated for the neutron. Position of the collision, number of new neutrons and their velocities are obtained.
- Absorption: Chain terminated for the neutron.

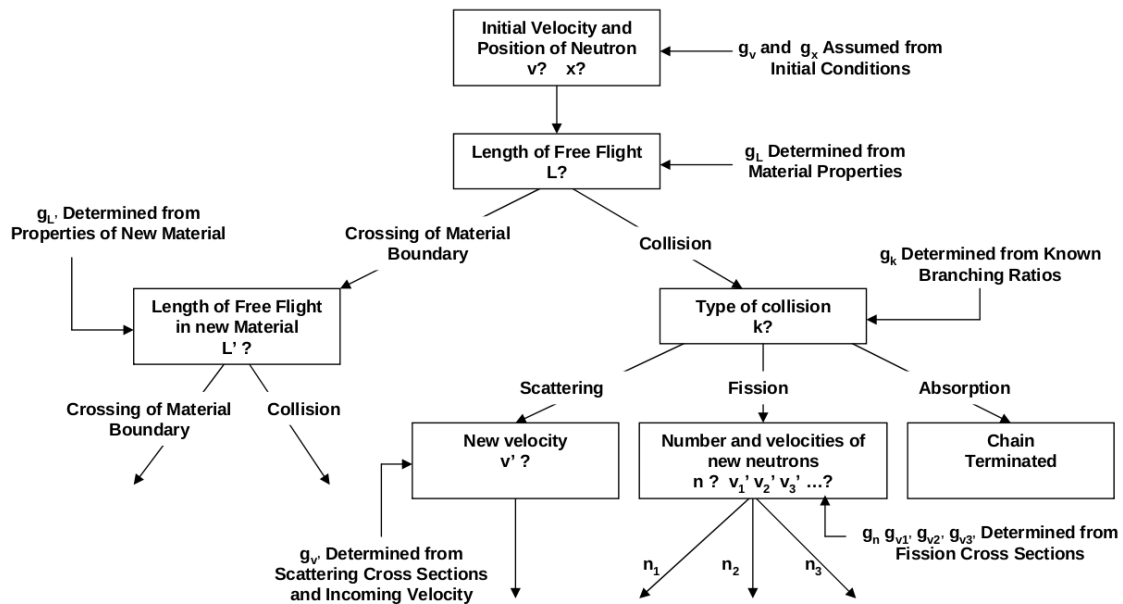


Figure 3.3. Schematic of decisions to generate the “history” of a neutron in the analog Monte Carlo estimation [32]

If the neutron crosses the material boundary, the information of the new material is needed and algorithm is executed again. The next history is completely independent from the previous history and this algorithm continues to run until all neutrons are absorbed or exit the system.

3.3.2. The implicit Monte Carlo estimation

On the other hand, the implicit method is based on modifying the neutron random walk with the aim of reducing the variance in the obtained results. In the implicit estimation a *statistical weight* is assigned to each neutron, which now represents the contribution of several particles (implicit estimation) instead of a single one (analog estimation). This statistical weight determines the importance of the score of a concrete neutron, being normalized every cycle for the source population in order to fix a total average importance of all the scores.

The implicit estimation becomes especially important for absorption reactions, where the statistical weight is reduced instead of terminating neutron history. A cut-off value is assigned in order to finish the neutron random walk when its weight falls below a certain limit. This reduction is done according to the fractional absorption probability, as equation (3.11) shows:

$$W' = W \left(1 - \frac{\Sigma_a}{\Sigma_t} \right) \quad (3.11)$$

Where,

- W and W' are the statistical weight before and after de collision.
- Σ_a and Σ_t are the absorption cross section and the total cross section, respectively.

By using the implicit estimation more information is obtained from one neutron, reducing the uncertainty in the results and producing more interactions in zones that are less accessible to neutrons. However, a benchmarking between the analog and implicit estimation is done in Chapter 5 in order to compare their results, checking if the use of the implicit estimation is that profitable as a priori seems to be and decide which of both methodologies is followed for the rest of simulations.

3.4. The SERPENT code

SERPENT is a three-dimensional continuous-energy Monte Carlo reactor physics burnup calculation code, whose development started at the VTT Technical Research Centre of Finland in 2004 under the working title “Probabilistic Scattering Game” (PSG) [33]. The SERPENT code is written in standard ANSI-C language²⁵ and reads continuous-energy interaction data from ACE format²⁶ cross section libraries, such as the *JEFF-3.1.1.xsdata* cross section library used in this thesis. To run the neutronics simulation it is necessary to model the geometry, materials, burnup parameters and other required options by using the SERPENT code.

The description of the geometry is one of the main parts of the simulation. SERPENT uses a model based on universes, where geometry is divided into separate independent levels nested one inside the other. By dividing the whole geometry into easier smaller parts and by using regular geometry structures and square and hexagonal lattices commonly encountered in reactor applications, SERPENT code allows simulating complex geometries (practically any 2D or 3D fuel pin, fuel assemblies or whole reactor configurations), which can be filled with the desired homogeneous material or other universes.

Materials can be modeled by defining its density, its nuclide fraction composition and its temperature. Cross sections of these nuclides are associated to a cross section library, which divides the information in fixed nuclide temperatures (300K, 600K, 900K, 1200K, 1500K and 1800K for *JEFF-3.1.1.xsdata* cross section library). However, by using SERPENT options it is possible to define intermediate temperatures for the nuclides, whose cross sections are obtained by interpolating the tabulated data.

²⁵ ANSI-C is the American National Standards Institute revision of C, a high-level programming language developed at Bell Labs that is able to manipulate the computer at a low level like assembly language.

²⁶ ACE file is a type of compressed archive which is created by the WinACE utility. It uses a proprietary compression algorithm that offers a high compression ratio and fast compression speed. The peak of its popularity was 1999–2001, when it provided slightly better compression rates than RAR, which has since become more popular.

SERPENT is also used for burnup calculation. The code uses an internal calculation routine for solving the Bateman equations, which describe abundances and activities in a decay chain as a function of time based on decay rates and initial abundances. The burnup calculation allows describing changes in the material compositions and radioactive decay, however, additional input is needed to run burnup calculation and be able to identify the depleted materials and set up irradiation history, such as the *JEFF-3.1.1.dec* decay data library and the *JEFF-3.1.1.nfy* fission yield data library used in this thesis. Finally, other options may be introduced depending on the desired output files, such as detectors, external sources, geometry plotter, etc.

3.4.1. SERPENT advantages

SERPENT code has one main strong point compared to similar traditional Monte Carlo codes (such as MCNP5/MCNPX codes) that make the transport simulation more efficient: the shorter time needed to run the calculation. Simulation time is one of the main computational codes features, becoming extremely important in large calculations (e.g. burnup calculations), which may require some days or even some weeks to obtain the desired solution. For the SERPENT code, this shorter time simulation is achieved basically by two main code characteristics:

- The possibility of using the **Woodcock delta-tracking method** in combination with conventional *ray-tracking method*.

MCNP5/MCNPX code uses the ray-tracking method, which is characterized by calculating the free path length each time neutron enters a new material, using its concrete cross section value. This means that the distance to the nearest surface boundary needs to be calculated to find the next collision site, as well as reading the cross section input file every time neutron enters a new material.

On the other hand, SERPENT code can use either ray-tracking method or Woodcock delta-tracking method, which is a rejection probability sampling technique that allows neutron to continue its path over material boundaries without stopping the track at each boundary surface [34]. For sampling path lengths in the Woodcock delta-tracking method the same cross section is used for all materials, which is called the *majorant cross section*. The majorant cross section is equal to or greater than the maximum of all material total cross sections for a concrete energy, so a virtual collision cross section needs to be added to each material total cross section in order to achieve the same majorant probability of interaction [30]:

$$\Sigma_m(E) = \Sigma_t(r, E) + \Sigma_0(r, E) \quad (3.12)$$

Where,

- $\Sigma_t(r, E)$ is the physical total cross section of the material.
- $\Sigma_0(r, E)$ is the virtual cross section added to achieve the majorant cross section value.
- $\Sigma_m(E)$ is the majorant cross section, the maximum of all total cross sections in the system and the same one for all nuclides. Notice that this makes Σ_m independent of the spatial coordinates.

This procedure generates “real” and “virtual” interaction probabilities for each material, which lead to “real” and “virtual” collisions that must be taken into account to obtain the correct solution. However, the probability of sampling a virtual collision (P_0) is known because of depending on Σ_t and Σ_m values, which are already known [30]:

$$P_0 = \frac{\Sigma_0}{\Sigma_m} = 1 - \frac{\Sigma_t}{\Sigma_m} \quad (3.13)$$

Therefore, by using the same majorant cross section for all materials, the calculation of the distance to the nearest boundary surface is not needed, so flight path is not interrupted every time neutron crosses a new material boundary and less computing calculations are needed. However, it loses its efficiency in presence of localized heavy absorbers (control rods, burnable absorber pins, etc.) because the majorant cross section becomes dominated by their high absorption cross sections, even if they represent a small fraction of the total volume of the system. In these cases, when the probability of sampling a physical (real) collision falls below a user-defined threshold, the code switches to the conventional surface-to-surface ray-tracking method.

- A single **unionized energy grid** for all nuclides is used to achieve major speed-up in calculation by minimizing the number of grid search iterations.

In other codes as MCNP5/MCNPX, inside the continuous-energy ACE format data each nuclide is associated to its own energy grid in order to calculate a desired cross section if needed. A linear interpolation is used to calculate the cross section σ at an energy E that lies between two tabulated energy points, E_{j-1} and E_j :

$$\frac{\sigma(E) - \sigma(E_{j-1})}{\sigma(E_j) - \sigma(E_{j-1})} = \frac{E - E_{j-1}}{E_j - E_{j-1}} \quad (3.14)$$

This methodology requires an iterative energy grid search for each nuclide (typically composed by 20.000 to 70.000 energy points for actinide cross sections [30]), increasing CPU time significantly, which becomes especially important when the neutron enters a new material and the calculation of material total cross section is needed again, carried out by summing over all the constituent nuclides.

On the other hand, SERPENT code uses the same grid for all nuclides (*master grid*), so the search of E_j and E_{j-1} has to be performed only once until the neutron scatters to a new energy. However, this unionized energy grid format requires more computer memory compared to other continuous-energy Monte Carlo codes because it is wasted on storing a large number of redundant data points when cross sections are reconstructed for each new energy value. This might be a problem in the case of needing a large master grid, e.g. in burnup calculations, although the amount of memory is usually not a limiting factor for current computers.

Chapter 4

Fuel Assembly Models

4.1. 17x17 Westinghouse fuel assembly

The 17x17 Westinghouse configuration of 2.775 MWt is the LWR fuel assembly modeled in this thesis in order to replace its current UO_2 fuel with FCM fuel. It is a square shaped fuel assembly that contains 264 fuel pins, 24 guide tubes for control rods and one central guide tube for instrumentation (see Figure 4.1), which are arranged in a square lattice [35]. This section is focused on describing the batch model for its SERPENT simulation, including geometry definition, materials composition and other used parameters.

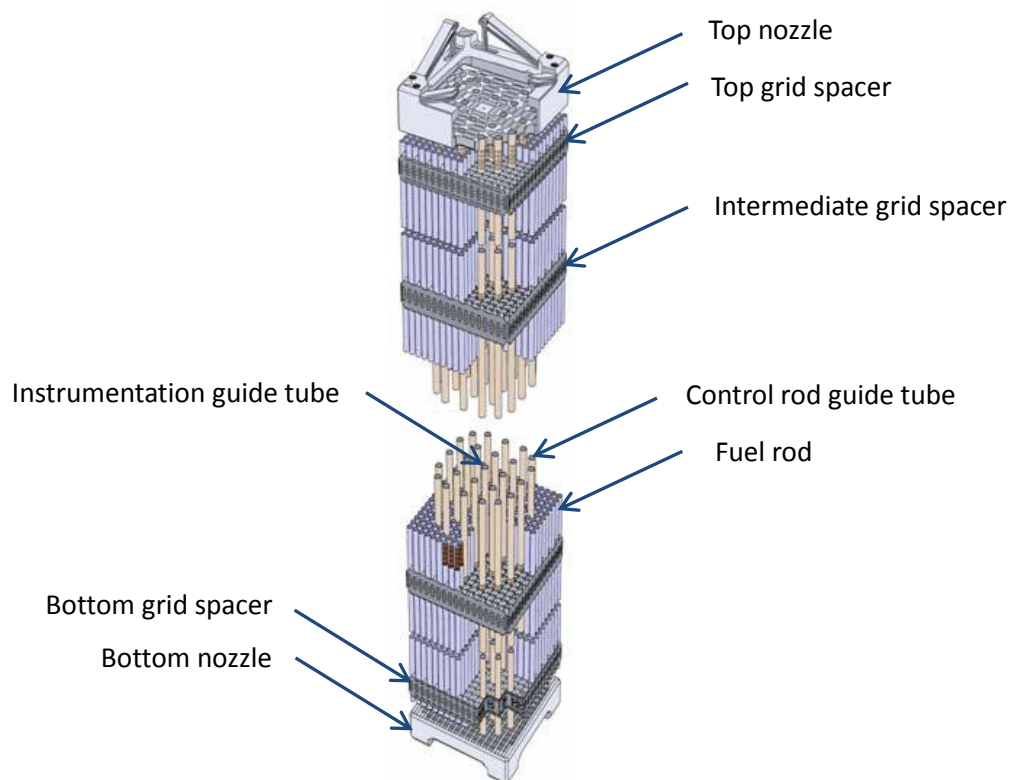


Figure 4.1. 17x17 Westinghouse fuel assembly

Geometry definition

The geometry definition is the first step on the fuel assembly modeling in SERPENT. Fuel pins, guide tubes and overall dimensions of the 17x17 Westinghouse fuel assembly are summarized in Table 4.1 and plotted in Figure 4.2, Figure 4.3 and Figure 4.4. One important note is that in this standard geometry description control rods are not simulated, so both instrumentation and control rod guide tubes are completely filled with water.

Element	Parameter	Value
Fuel rod (Figure 4.2)	Number of fuel rods	264
	Clad outer diameter (cm)	0,9518
	Pellet diameter (cm)	0,8050
	Gap thickness (cm)	0,0093
	Clad thickness (cm)	0,0641
	Fuel rod active length (cm)	367,20
Guide tube (Figure 4.3)	Number of guide tubes	25
	Clad outer diameter (cm)	1,2260
	Clad thickness (cm)	0,0421
Fuel assembly (Figure 4.4)	Rod pitch (cm)	1,266
	Overall dimensions (cm x cm)	21,522 x 21,522

Table 4.1. 17x17 FA dimensions [35, 36]

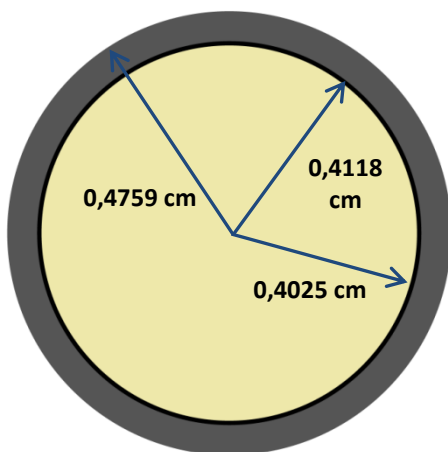


Figure 4.2. 17x17 FA fuel rod geometry

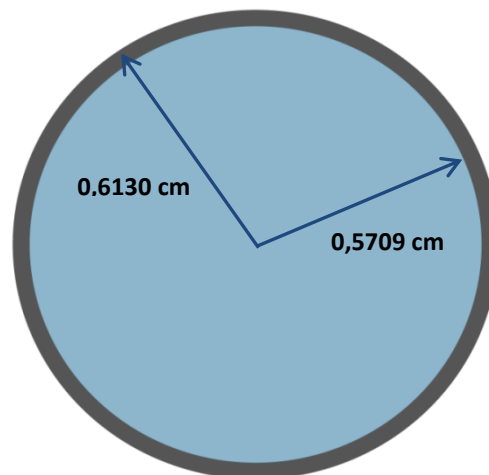


Figure 4.3. 17x17 FA guide tube geometry

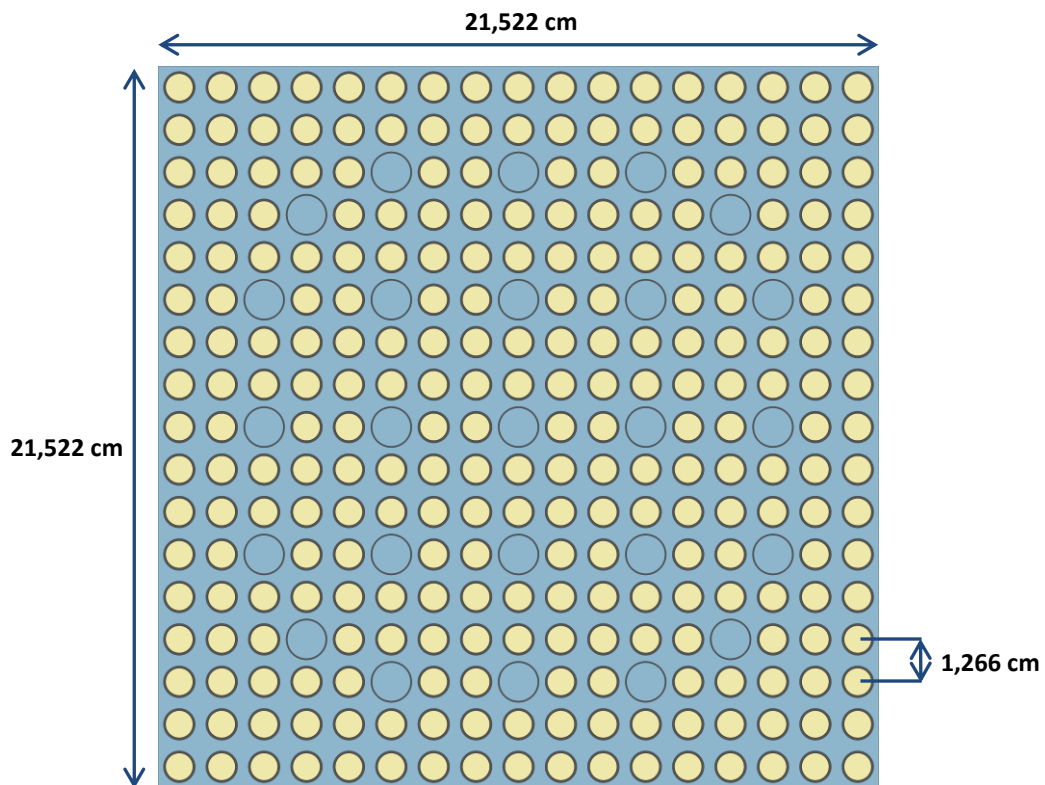


Figure 4.4. 17x17 FA Z=0 cross-cut

Materials definition

After defining geometry parameters, each region of the fuel assembly geometry is filled with the corresponding material, as shown in Figure 4.5. The composition of the used materials, as well as the properties and parameters needed for their simulation are explained below:

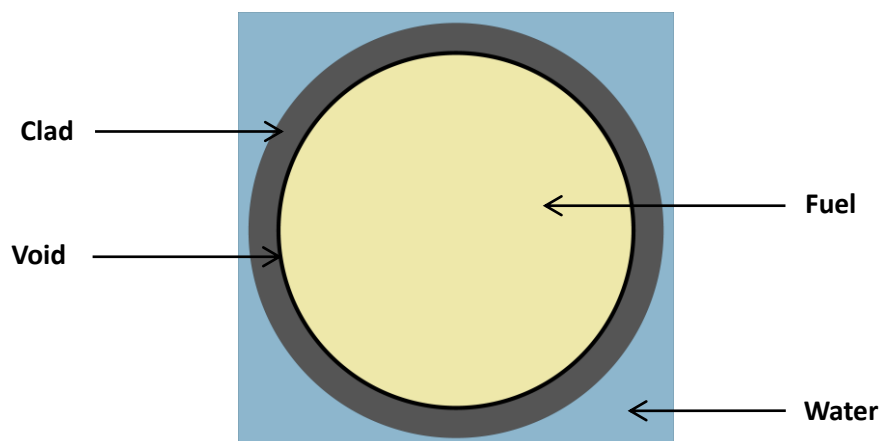


Figure 4.5. 17x17 FA fuel pin materials

- Fuel:** 4% enriched UO_2 fuel with $10,412 \text{ g/cm}^3$ density has been used in this fuel assembly [37], which is a typical enrichment for this standard configuration of 2.775 MWt. Aside from fuel density and fuel composition, it is necessary to define its temperature in order to work with accurate cross sections values during the simulation. According to the temperature distribution over the section of the pellet (see Figure 4.6), an average temperature of 1200K (927°C) has been considered.

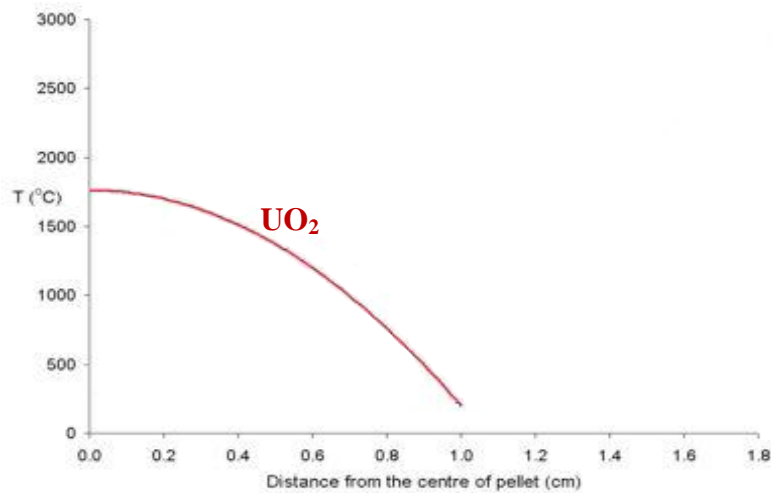


Figure 4.6. Temperature distribution over UO_2 pellet section [10]

- Water:** When defining the light water (H_2O) it is important to notice that its density is significantly variable with its temperature (see Figure 4.7). As explained in Chapter 1, in PWRs water enters the vessel at $\sim 560\text{K}$ and exits at $\sim 590\text{K}$ temperature, so according to these water work temperatures an average temperature of 573K (300°C) has been considered for the simulation, whose corresponding density at this temperature is $725,55\text{g/cm}^3$ (see Table 4.2)²⁷.

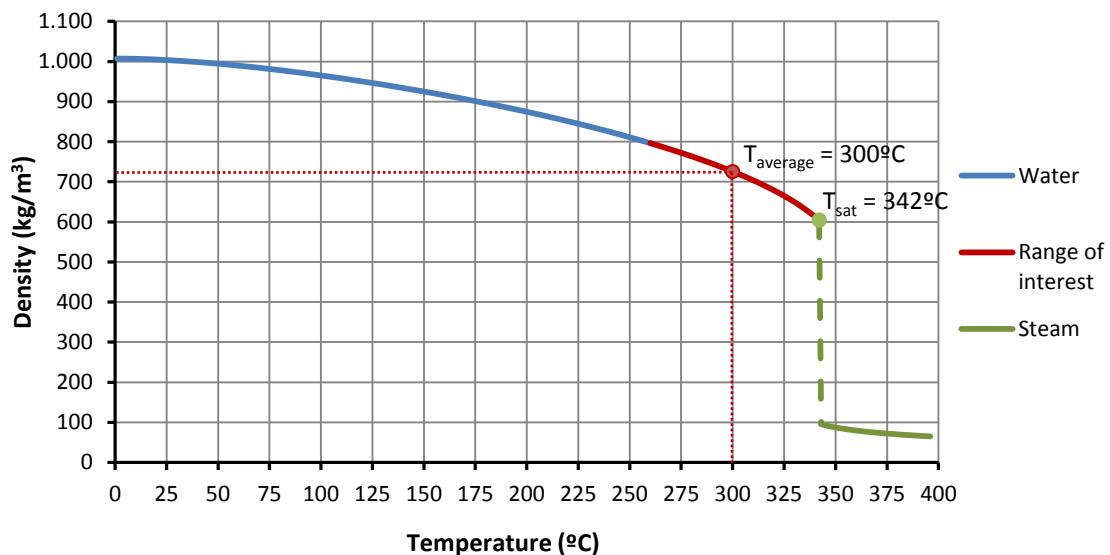


Figure 4.7. Density – Temperature water curve for 150kg/cm^2 pressure

²⁷ Figure 4.7 and Table 4.2 show density values for a concrete work pressure (150kg/cm^2). Pressure must be taken into account to obtain a correct density value because at these work temperatures water compressibility is not negligible.

Temperature (°C)	Density (Kg/m ³)
260	796,20
268	783,67
276	770,46
284	756,46
292	741,56
300	725,55
308	708,20
316	689,11
324	667,73
332	643,07

Table 4.2. Water density values for 150kg/cm² pressure (Range of interest)²⁸

- **Clad:** ZirloTM is the Zirconium alloy used for the cladding material, whose density is 6,5g/cm³ and nuclei composition is summarized in Table 4.3 [38]. In order to choose the concrete clad composition to run the simulation, an average quantity for each nuclide has been used. Regarding to the temperature parameter, a 600K temperature has been considered to complete clad definition, same as water temperature.

Nuclei	Composition	Used values
Nb	0,5 – 2 %	1,30%
Sn	0,9 – 1,5 %	1,20%
Fe,Cr,Mo,V,Cu,Ni,W	0,09 – 0,11 %	0,1% (only Fe)
Zr	Other	97,40%

Table 4.3. ZirloTM nuclei composition and used values

Other conditions

Finally, apart from the geometry and the materials characteristics, three important conditions have been included in order to define accurately the fuel assembly. They are commented below:

- A *periodic boundary condition* for the fuel assembly external surfaces. Using this option, when the neutron encounters a periodic boundary, it is moved to the opposite surface of the geometry [33]. This is an adequate boundary condition because of working at a fuel assembly level, which could receive neutrons from the surrounding fuel assemblies.
- A *thermal scattering cross section* used for the Hydrogen in water, because some significant errors would be introduced by modeling important bound moderator nuclides using free-atom cross sections. This option is mainly applied to Hydrogen in water and Carbon in graphite [33].

²⁸ Magnus Holmgren, *X STEAM FOR MATLAB*, January 2006. www.x-eng.com

- A *quadrant symmetry condition* for the overall fuel assembly geometry. Statistical errors and time of simulation can be reduced by taking advantage of the symmetry condition, which divides the desired universe into similar portions, simplifying the treated geometry.

4.2. 13x13 FCM fuel assembly

A new fuel assembly has been described in order to develop a feasible fuel replacement for the 17x17 Westinghouse configuration. The new fuel assembly uses FCM fuel instead of UO_2 fuel but needs to have very similar and compatible characteristics with the original. It is essential to study power generation, thermo-hydraulics and neutronics compatibilities with the original Westinghouse configuration, as well as to achieve comparable levels of linear fissile density and reactivity behavior [39].

In this thesis a 13x13 FCM UN fuel assembly has been selected to replace the original 17x17 UO_2 configuration. The new batch is focused on the use of UN fuel because its density is significantly higher than the alternatives (40-50% higher than the UO_2 fuel and 30-40% higher than the UCO fuel), allowing lower enrichment requirements compared to them. However, it must be said that UO_2 and UCO kernel fuel with TRISO coatings has been successfully produced for years whereas UN kernel fuel is still in development. Moreover, and thanks to the higher conductivity of the FCM fuel, a less number of wider fuel rods can be used in the new fuel assembly compared to the original, which is an advantage mainly because of two reasons:

- A larger diameter of the compact has advantage in self-shielding, which increases cycle length and reduces the need of a large amount of poison absorbents especially at the beginning of the cycle. This is very important since the new configuration uses high enriched fuels, which have a poorer self-shielding property compared to others because of having a higher fissile material - heavy metal mass rate, leading to be more reactive.
- A larger diameter of the compact has also advantage in achieving higher TRISO particles packing fraction by less wall effect. This is important in order to increase fuel pin density power without increasing even more fuel enrichment, which is expensive and has technological limitations.

After fixing the number of fuel rods that configure the new fuel assembly and the type of fuel used in it, the aim of this compatibility study is to calculate the fuel rod diameter and the UN enrichment for the 13x13 FCM fuel assembly, in order to obtain similar thermo-hydraulic and power characteristics as the original configuration.

4.2.1. Compatibility study

Thermo-hydraulic compatibility study

The first important consideration with the aim of configuring the 13x13 fuel assembly is to assume that the specific enthalpy rise in the whole fuel assembly water channel is equal to that of the existing 17x17 fuel assembly. This means that 1kg of coolant absorbs the same amount of energy in both configurations, achieving a similar exit temperature, which is very important in order to maintain the heat transferring conditions between the primary circuit and the secondary circuit in a PWR. In addition, working in the same range of temperatures as the original fuel assembly helps to ensure no boiling transition for the same operative pressure value.

The specific enthalpy rise (Δh) in the fuel assembly water channel is related to the total heat generation of the whole fuel assembly (q) as follows:

$$q \left[\frac{kJ}{s} \right] = \Delta h \left[\frac{kJ}{kg} \right] \rho v A \quad (4.1)$$

Where,

- $\rho \left[\frac{kg}{cm^3} \right]$ is the coolant density
- $v \left[\frac{cm}{s} \right]$ is the coolant speed
- $A \left[cm^2 \right]$ is the wet area

Notice that $\rho v A = \text{water flow} \left[\frac{cm^3}{s} \right]$

In a NPP, all systems are dimensioned for a concrete power generation, so a feasible fuel replacement must conserve the thermal power produced in one fuel assembly (2.775 MWt in this case). According to equation (4.1), the only possible way to keep the reactor thermal power constant, as well as the same specific enthalpy rise of the coolant, is by using a **constant water flow**.

Secondly, the water flow in the 13x13 new configuration is desired to experience the same heat transfer and friction effects as the original fuel assembly. To achieve these conditions, a new hydraulic parameter comes to the picture, the *hydraulic diameter*. The concept of hydraulic diameter is introduced to obtain a hydraulically equivalent circular channel for flows which have non-circular cross sectional flow area (such as one fuel assembly).

As explained further on in this study, a thermo-hydraulic compatibility (i.e. same heat transfer and friction effects) between two configurations which have the same water flow is achieved by having a **same hydraulic diameter**. The definition of hydraulic diameter (D_h) is expressed in equation (4.2):

$$D_h [cm] = \frac{4 \cdot A}{P_w} \quad (4.2)$$

Where,

- $A [cm^2]$ is the water cross sectional area
- $P_w [cm]$ is the wetted perimeter of the cross sectional area

Equation (4.2) shows that D_h is a relationship between the section the water flows through and its heat transfer contact perimeter. As explained by using Figure 4.8 and Figure 4.9, this relationship is the same in both fuel assembly and fuel rod levels, since they are proportional geometries.

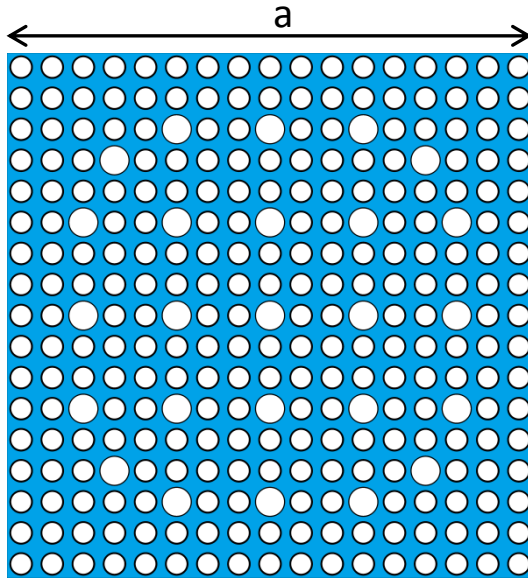


Figure 4.8. Total fuel assembly water channel

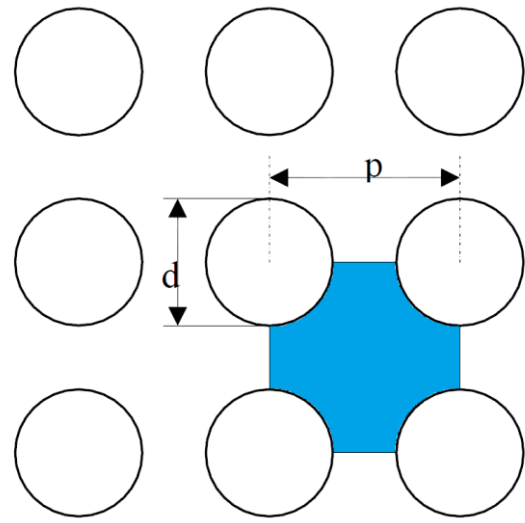


Figure 4.9. One fuel pin water channel

$$D_{h(17 \times 17)} = \frac{4 \cdot \left(a^2 - 17 \cdot 17 \cdot \frac{\pi \cdot d^2}{4} \right)}{17 \cdot 17 \cdot \pi \cdot d} = 1,192 \text{ cm} \quad D_{h(17 \times 17)} = \frac{4 \cdot \left(p^2 - \frac{\pi \cdot d^2}{4} \right)}{\pi \cdot d} = 1,192 \text{ cm}$$

Therefore, to achieve a same D_h in both configurations, a same D_h for one fuel pin water channel must be achieved. By imposing this condition, the new clad outer diameter ($d_{(13 \times 13)}$) is calculated:

$$D_{h(13 \times 13)} = 1,192 \text{ cm} = \frac{4 \cdot \left(1,6555^2 - \frac{\pi \cdot d_{clad(13 \times 13)}^2}{4} \right)}{\pi \cdot d_{clad(13 \times 13)}} \rightarrow d_{clad(13 \times 13)} = 1,365 \text{ cm}$$

The very idea of imposing equal hydraulic diameters in both configurations is that, for the same fluid mass flow, both coolants must pass touching the same area of rod wall surface per unit time, experiencing the same heat transfer and friction effects:

The water flow (\dot{m}) of both configurations can be written as follows:

$$\begin{aligned}\dot{m}_{17x17} &= \rho_{17x17} \cdot v_{17x17} \cdot \left(p_{17x17}^2 - \frac{\pi \cdot d_{clad(17x17)}^2}{4} \right) \\ \dot{m}_{13x13} &= \rho_{13x13} \cdot v_{13x13} \cdot \left(p_{13x13}^2 - \frac{\pi \cdot d_{clad(13x13)}^2}{4} \right)\end{aligned}\quad (4.3)$$

In addition, water density is assumed as a constant parameter and same water flow for both configurations is applied as deduced before:

$$\begin{aligned}\dot{m}_{17x17} &= \dot{m}_{13x13} \\ \rho_{17x17} &= \rho_{13x13}\end{aligned}\quad (4.4)$$

Hence, by using equation (5.3) and equation (5.4) it is possible to achieve a relationship between the coolant velocities in both fuel assemblies:

$$v_{13x13} \left[\frac{cm}{s} \right] = \frac{p_{17x17}^2 - \frac{\pi \cdot d_{clad(17x17)}^2}{4}}{p_{13x13}^2 - \frac{\pi \cdot d_{clad(13x13)}^2}{4}} \cdot v_{17x17} = 0,69768 \cdot v_{17x17}$$

Therefore, it can be proved that by using the same hydraulic diameter a same rod wall surface area is contacting the coolant per second in both cases, achieving the desired thermo-hydraulic compatibility:

$$\begin{aligned}\frac{\text{wall surface area}}{s}_{17x17} \left[\frac{cm^2}{s} \right] &= v_{17x17} \left[\frac{cm}{s} \right] \cdot P_{w\ 17x17} [cm] = v_{17x17} \cdot 0,9518\pi \\ \frac{\text{wall surface area}}{s}_{13x13} \left[\frac{cm^2}{s} \right] &= v_{13x13} \left[\frac{cm}{s} \right] \cdot P_{w\ 13x13} [cm] = 0,69768 \cdot v_{17x17} \cdot 1,365\pi = \\ &= v_{17x17} \cdot 0,9518\pi\end{aligned}$$

Lastly, rod diameter can be calculated by knowing clad and gap thicknesses in this new configuration, which are reduced to 0,053cm and 0,0085cm respectively [40] due to the new work conditions where fission products are not released to the gap. Hence, the new pellet diameter obtained is:

$$d_{fuel(13x13)} = 1,242\ cm$$

Power compatibility study

The power compatibility study for the 13x13 fuel assembly has been done considering the same fissile material quantity as for the existing 17x17 fuel assembly, condition that will determine UN enrichment as explained below. It is important to notice that, since the 13x13 configuration uses FCM fuel instead of UO₂ fuel, the UN enrichment will strongly depend on TRISO particle geometry configuration. Particularly, it will depend on TRISO kernel diameter (KD) and packing fraction parameter (PF), this latter defined as follows:

$$PF [\%] = \frac{V_{TRISO}}{V_{total}} \cdot 100 \quad (4.5)$$

Where,

- V_{TRISO} is the volume occupied by TRISO particles
- V_{total} is the total volume of the fuel rod

Theoretical packing of mono-sized spheres approaches 74%; however, during the compacting process the maximum achievable packing fraction reduces significantly because of the wall effect, decreasing while reducing fuel rod and TRISO particles diameters. Therefore, larger packing fractions than 50% will be not considered.

To perform the power compatibility study it is important to notice that a concrete PF - KD combination define two important parameters for the FCM fuel rod configuration. First, it fixes the number of TRISO particles inside the fuel pin because of defining the concrete TRISO particle dimensions and a concrete volume rate (see Table 4.4). Secondly, it also fixes the total UN fuel volume, which means to obtain a concrete UN enrichment in each case if the same fissile material quantity is wanted (see Table 4.5).

KD / PF	Number of TRISO particles				
	30%	35%	40%	45%	50%
400 μm	810.647	945.755	1.080.862	1.215.970	1.351.078
500 μm	537.124	626.645	716.165	805.686	895.207
600 μm	374.033	436.372	498.711	561.050	623.389
700 μm	270.820	315.956	361.093	406.229	451.366

Table 4.4. Number of TRISO particles inside a fuel rod depending on KD – PF configuration

KD / PF	UN enrichment (%)				
	30%	35%	40%	45%	50%
400 μm	31,29	26,82	23,46	20,86	18,77
500 μm	24,18	20,72	18,13	16,12	14,51
600 μm	20,09	17,22	15,07	13,39	12,05
700 μm	17,47	14,98	13,11	11,65	10,48

Table 4.5. UN enrichment depending on KD – PF configuration

Information of Table 4.5 has been plotted in Figure 4.10, appreciating that UN enrichment decreases as KD and PF increase.

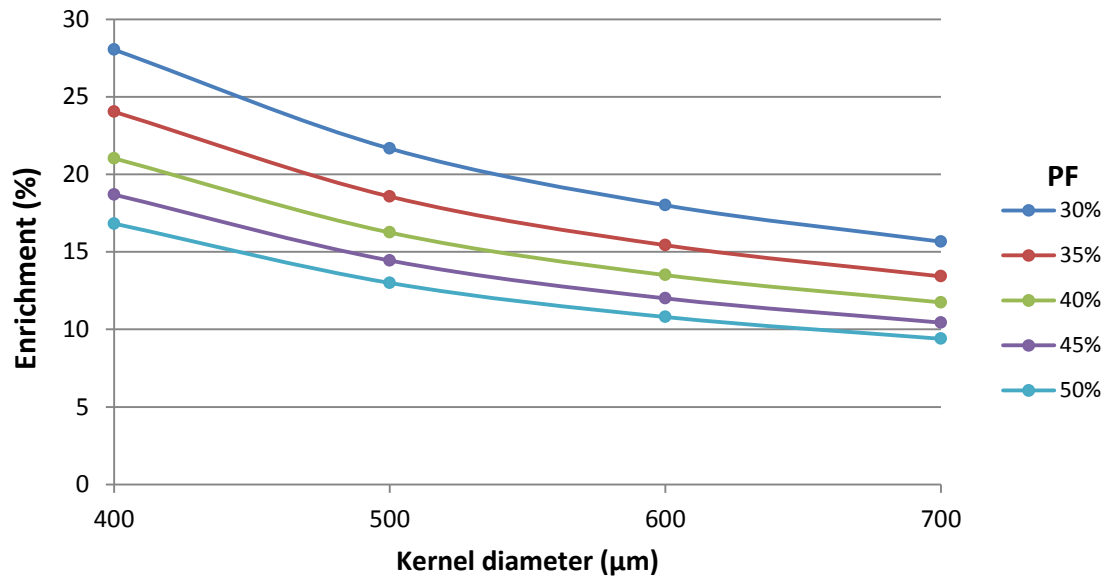


Figure 4.10. UN enrichment depending on KD – PF configuration

An advantage of having a small kernel KD is the possibility to achieve a higher burnup than using larger diameters by better neutron moderation and lower self-shielding. However, it decreases significantly the cycle length, increases the absorbent requirements to keep the system critical at BOL and requires a higher UN enrichment to reach the amount of fissile material of the original configuration.

Taking into account that burnup is already highly increased by using FCM fuel instead of UO_2 regardless of the KD and the PF, the largest KD is selected in this thesis with the aim of having a fuel more similar to UO_2 in the commented aspects, *i.e.* $KD=700\mu\text{m}$.

Moreover, as shown in Figure 4.11, the required enrichment reduces as long as PF increases. However, this reduction effect becomes less important for higher packing fraction values, making worthier a PF=35% in front of a PF=30%, than a PF=50% in front of a PF=45%.

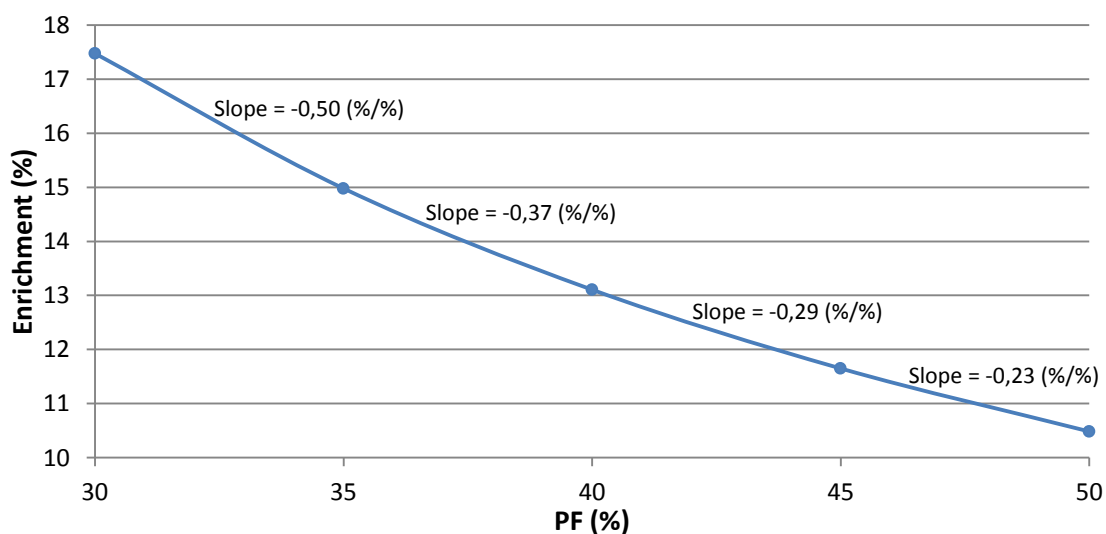


Figure 4.11. UN enrichment depending on PF value for $KD=700\mu\text{m}$

Therefore, an intermediate PF value has been selected, trying to not achieve a very high enrichment value as well as ensuring the FCM fuel pellet fabrication by not considering very high packing fractions, i.e. $PF=40\%$. In accordance, although current development objectives are focused on obtaining higher than 60% packing fraction values, to date the development work has produced TRISO compacted pellets in a SiC matrix with a particle packing fraction of about 40%. Last but not least, it is important to notice that the obtained enrichment requirement is about 13%, below the 20% proliferation level limit [41].

4.2.2. TRISO particles modeling

SERPENT code allows various methodologies of dispersing TRISO particles in a surrounding matrix, needing two steps in any case. First step is to model TRISO particle geometry, and second step is to disperse them inside the desired matrix. TRISO geometry definition is a common first step for all methodologies, and is achieved by using a concrete SERPENT capability to model spherical particles. To define them it is only necessary to describe its diameter, the successive layers thicknesses, and the materials they are composed of.

However, various methods can be used in order to disperse the modeled TRISO particles inside a matrix, which are qualitatively explained below. Further on, some simulations will be done using these methods in order to compare them, checking if same results are obtained or there are significant differences depending on the modeling type.

- **Infinite 3D lattices.** TRISO particles can be defined in a 3D matrix by modeling regular cubical or hexagonal prismatic 3D arrangements (see Figure 4.12 and Figure 4.13). The only programming input required to model these arrays is the distance between the TRISO particles, which makes this method an easy way to define them.

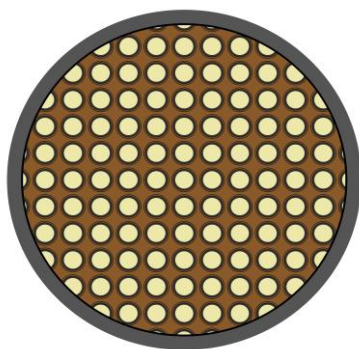


Figure 4.12. Regular cubical 3D lattice TRISO particles distribution



Figure 4.13. Hexagonal prismatic 3D lattice TRISO particles distribution

However, two inconvenient result from this modeling. In first place, the regular arrangement fails to account for the random distribution of particles because they are ordered one next to each other. Secondly, when a cylindrical fuel rod is filled with a regular cubical or a hexagonal prismatic lattice, some TRISO particles may be cut by the outer boundary. To avoid these problems, SERPENT code has two other geometry models specifically designed for TRISO particles.

- **Implicit particle fuel model.** This model is based on sampling new TRISO particles on the neutron path during its random walk. However, this method has not been considered in this thesis because SERPENT manual [33] warns that the results obtained using the SERPENT 1.1.14 version are highly dependent on packing fraction values and have some significant differences compared to the most accurate methodology to define the TRISO particles, the explicit model explained below.
- **Explicit particle/pebble bed fuel model.** This model consists on distributing the TRISO particles by reading their concrete position coordinates from an external file. The main advantages are the possibility to achieve a random distribution and to avoid the cut particles problematic by correctly designing the external file (see Figure 4.14).

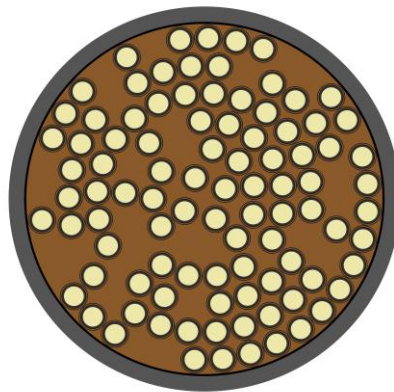


Figure 4.14. Random TRISO particles distribution using explicit particle fuel model

However, the main disadvantage is the time of simulation, which increases significantly. This factor makes very important to analyze whether the results obtained using the explicit model have significant differences compared to the results obtained using the infinite 3D lattice.

4.2.3. 13x13 FCM fuel assembly final design

Geometry definition

The new 13x13 FCM fuel assembly is also a square shaped fuel assembly with the same overall dimensions as the 17x17 configuration, a necessary condition to maintain the dimensions of the whole core. The new fuel assembly contains 160 fuel pins and 9 guide tubes that are completely filled with water in this standard geometry description. Guide tube dimensions are approximated to be the same as the fuel pin dimensions in order to run the simulation, which does not have a relevant importance regarding to the neutronics. Fuel assembly dimensions are summarized in Table 4.6 and plotted in Figure 4.15, Figure 4.16 and Figure 4.17.

Element	Parameter	Value
Fuel rod (Figure 4.15)	Number of fuel rods	160
	Clad outer diameter (cm)	1,363
	Pellet diameter (cm)	1,24
	Gap thickness (cm)	0,0085
	Clad thickness (cm)	0,053
	Fuel rod active length (cm)	367,20
Guide tube (Figure 4.16)	Number of guide tubes	9
	Clad outer diameter (cm)	1,363
	Clad thickness (cm)	0,053
Fuel assembly (Figure 4.17)	Rod pitch (cm)	1,6555
	Overall dimensions (cm x cm)	21,402 x 21,402

Table 4.6. 13x13 FCM FA dimensions

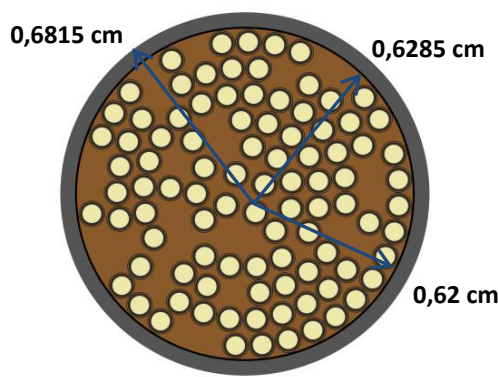


Figure 4.15. 13x13 FA fuel pin geometry

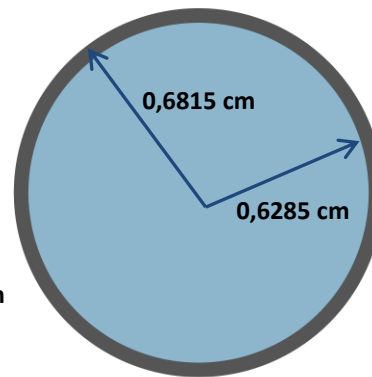


Figure 4.16. 13x13 FA guide tube geometry

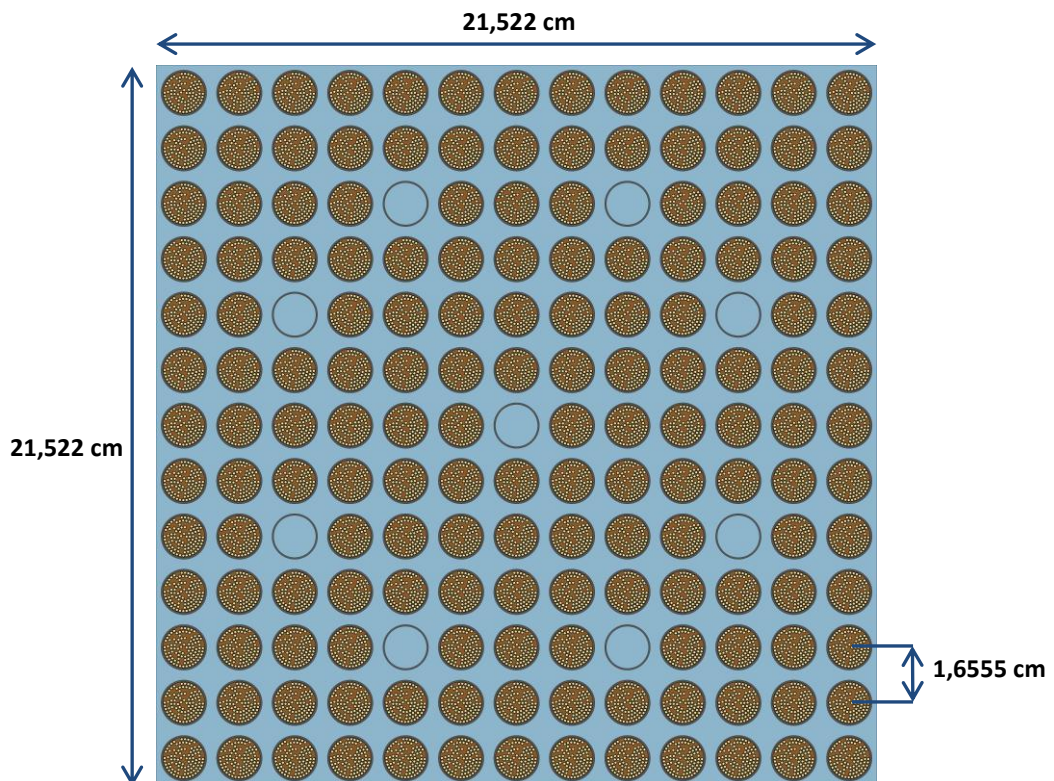


Figure 4.17. 13x13 FCM FA Z=0 cross-cut

Materials definition

Each region of the fuel assembly geometry has been filled with the corresponding material, as shown in Figure 4.18. Materials composition and its properties are explained below:

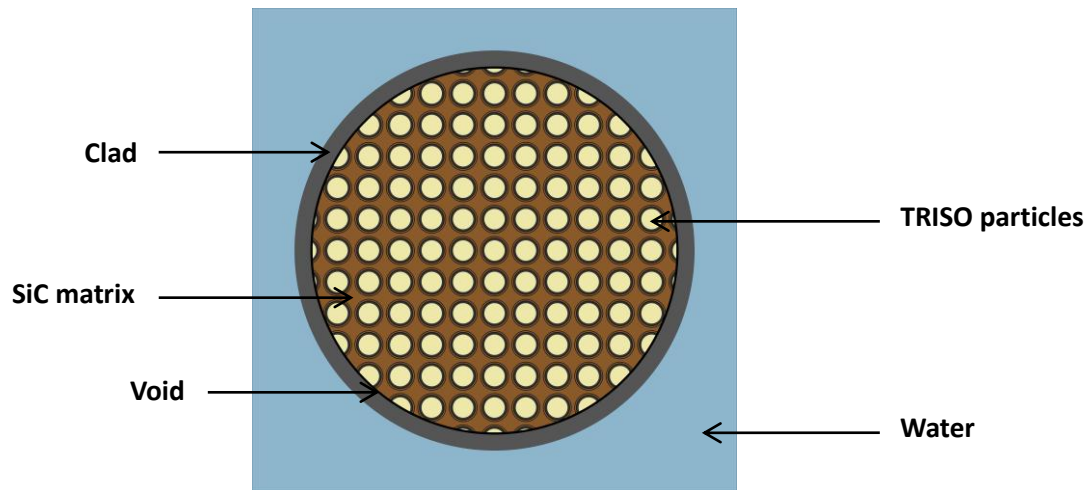


Figure 4.18. Materials of 13x13 FCM FA

- **FCM Fuel:** It is composed by TRISO particles with UN kernel ($14,32 \text{ g/cm}^3$ density), which are embedded inside a SiC matrix of $3,18 \text{ g/cm}^3$ density. Table 4.7 summarizes TRISO particles dimensions, layer thicknesses and the materials they are composed of [40].

TRISO particle	
Kernel diameter	Variable
Buffer layer thickness	50 μm
Inner PyC coating thickness	35 μm
SiC coating thickness	35 μm
Outer PyC coating thickness	20 μm

UN Kernel	
U-235	variable
U-238	variable
N	8,11%
Density	14,32 g/cc

Buffer layer	
C	100%
Density	1,05 g/cc

PyC coatings	
C	100%
Density	1,9 g/cc

SiC coating	
Si	70,05%
C	29,96%
Density	3,18 g/cc

Table 4.7. TRISO particles materials description

In addition, and according to the temperature distribution over the section of the pellet (see Figure 4.19), a simulation temperature of 600K has been considered because of the low operation temperature gradient achieved by the UN higher thermal conductivity.

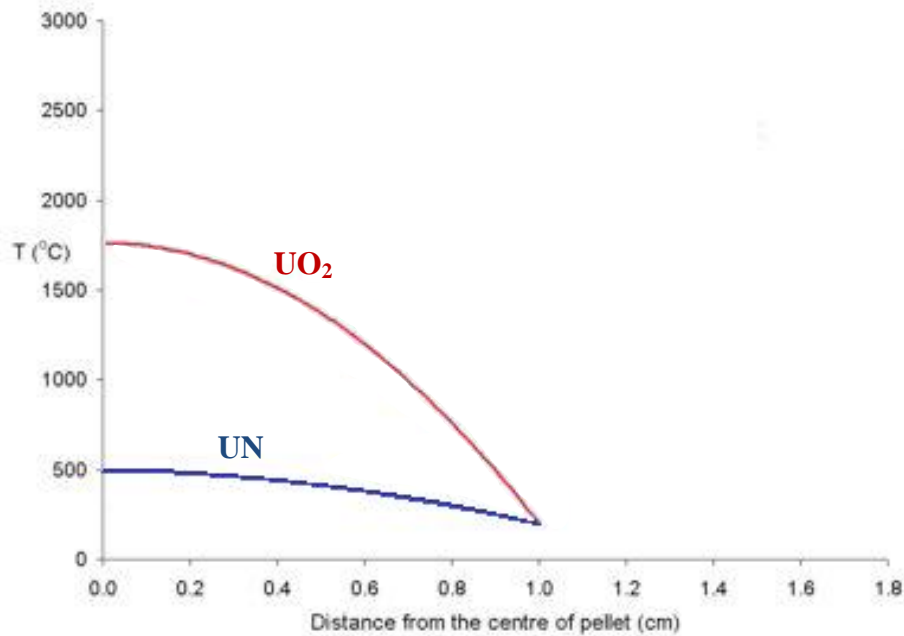


Figure 4.19. Temperature distribution over a UN pellet section [10]

- **Clad and Water:** Both are defined the same as in the original 17x17 Westinghouse fuel assembly. In first place, water works at the same temperature and experiments the same enthalpy rise in both configurations as explained before. Secondly, although the use of a SiC clad would be possible by using FCM fuel, a Zirlo™ clad will be simulated in order to focus the results on fuel configuration aspects.

Other conditions

The *periodic boundary condition* for the fuel assembly external surfaces and the *thermal scattering cross section* used for the hydrogen in water are also included in the new configuration. However, it is important to notice that the *symmetry condition* should only be used depending on the distribution of the TRISO particles. Symmetry can be used for 3D regular arrays but it must be careful depending on the TRISO particle distribution determined by the external file if using the explicit particle fuel model.

Chapter 5

Simulation

5.1. Simulation parameters analysis

Before running all the required simulations to obtain the desired safety information about the FCM fuel neutronics behavior, it is necessary to define some simulation parameters; such as the Monte Carlo estimation method, the number of cycles, the neutron population per cycle or the number of burnup steps selected for these simulations. A concrete definition of these variables is very important because significant changes in the results are introduced depending on their value. Two main statistical parameters have been used in order to perform these analyses: The standard deviation of the average ($\sigma_{\bar{x}}$) and the Figure of Merit (FOM), which will be briefly introduced below.

- **Standard deviation of the average ($\sigma_{\bar{x}}$):** To talk about the standard deviation, first it is necessary to emphasize the difference between the *accuracy* and *precision* concepts [32]. **Accuracy** measures the proximity of the expected value (\bar{x}) to the true physical quantity (μ_x) is desired to be estimated. The difference between them is usually unknown and is called *the systematic error or bias* (see Figure 5.1):

$$\text{systematic error/ bias} = \mu_x - \bar{x} \quad (5.1)$$

Where \bar{x} is the average of scores of the number of sampled histories (N), i.e.:

$$\bar{x} = \frac{1}{N} \sum_{i=1}^N x_i \quad (5.2)$$

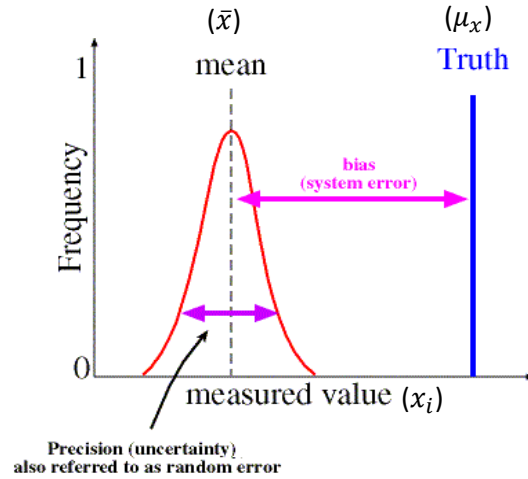


Figure 5.1. Difference between accuracy and precision²⁹

On the other hand **precision** refers to the uncertainty of the Monte Carlo statistical method, i.e. a random error. The precision is determined by the variation in the different scores x_i and is measured by the *standard deviation* (σ) of the sampled histories, which is defined in equation (5.3) for a large population (N):

$$\sigma^2 \equiv \frac{1}{N-1} \sum_{i=1}^N (x_i - \bar{x})^2 \cong \overline{x^2} - \bar{x}^2 \quad (5.3)$$

Where,

$$\overline{x^2} \equiv \frac{1}{N} \sum_{i=1}^N x_i^2 \quad (5.4)$$

However, the important parameter regarding to uncertainty in the solution is the *standard deviation of the average* ($\sigma_{\bar{x}}$), which is the one given by the output file and the one useful to compare the results between various simulations. It is expressed in equation (5.5):

$$\sigma_{\bar{x}}^2 = \frac{1}{N} \sigma^2 \rightarrow \sigma_{\bar{x}} \sqrt{\frac{\overline{x^2} - \bar{x}^2}{N}} \propto \frac{1}{\sqrt{N}} \quad (5.5)$$

In a normal distribution, $\sigma_{\bar{x}}$ defines the error for the average value of the samples (\bar{x}) depending on the confidence of the result, determining various confidence intervals (CI) as shown below (see Figure 5.2):

$$\begin{aligned} CI \ 68\% &\rightarrow [\bar{x} - \sigma_{\bar{x}} \leq \bar{x} \leq \bar{x} + \sigma_{\bar{x}}] \\ CI \ 95\% &\rightarrow [\bar{x} - 1,96\sigma_{\bar{x}} \leq \bar{x} \leq \bar{x} + 1,96\sigma_{\bar{x}}] \\ CI \ 99\% &\rightarrow [\bar{x} - 2,58\sigma_{\bar{x}} \leq \bar{x} \leq \bar{x} + 2,58\sigma_{\bar{x}}] \end{aligned}$$

²⁹ Lyndon State College Atmospheric Sciences.

http://apollo.lsc.vsc.edu/classes/remote/lecture_notes/measurements/bias_random_errors.html

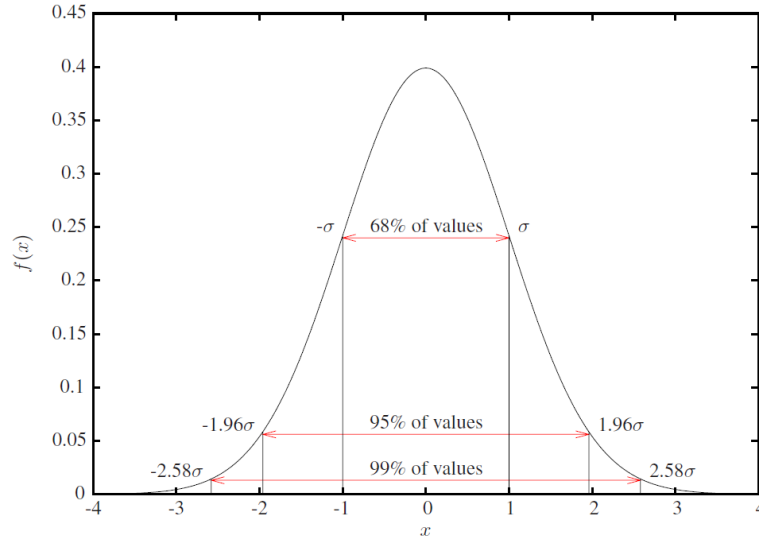


Figure 5.2. The normal distribution and the 68%, 95% and 99% confidence intervals [30]

- **Figure of merit:** It is a numerical quantity based on one or more characteristics of a device, system or method, representing a measure of efficiency or effectiveness. This statistic is also applied for the Monte Carlo method, and is defined in equation (5.6):

$$FOM = \frac{1}{R^2 T} \quad (5.6)$$

Where,

$$R = \frac{\sigma_{\bar{x}}}{\bar{x}} \propto \frac{1}{\sqrt{N}} \quad (5.7)$$

- R is the relative error ($R^2 \propto 1/N$).
- T is the simulation time (proportional to the number of histories, $T \propto N$).

According to the mentioned proportionalities: $R^2 \propto 1/N$ and $T \propto N$, FOM should remain relatively constant after some first transient cycles of simulation. This statistic is very useful to see if the Monte Carlo simulation gives an expected response, as well as to see how many cycles of how many neutrons are needed to achieve the desired constant shape in the FOM.

5.1.1. Analog and implicit estimations comparison

As explained in Chapter 3, the implicit estimation of k_{eff} seems to be better than the analog estimation since more information is obtained per neutron, reducing the uncertainty in the solution. However, some benchmarking simulations have been done in order to check the behavior of both methodologies, with the aim of deciding which one will be used from now on. The simulation is done for the 13x13 FCM fuel assembly by running **1500 cycles** of **10000 neutrons population**, and both analog and implicit estimations will be compared by using the two statistical parameters introduced before: the FOM and the $\sigma_{\bar{x}}$.

▪ Analog k_{eff} estimation

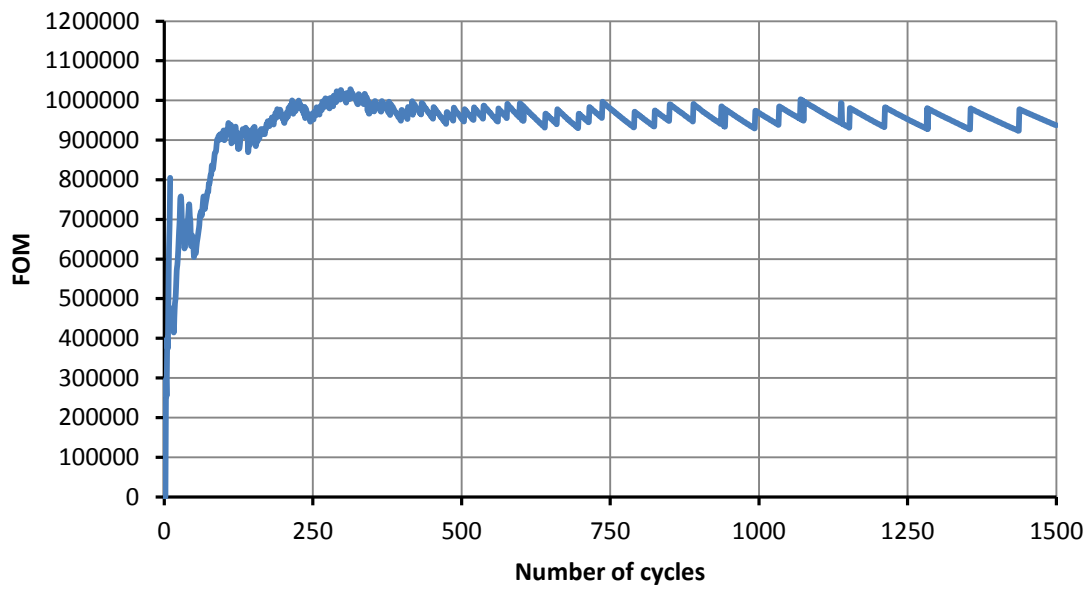


Figure 5.3. FOM using Analog k_{eff} estimation

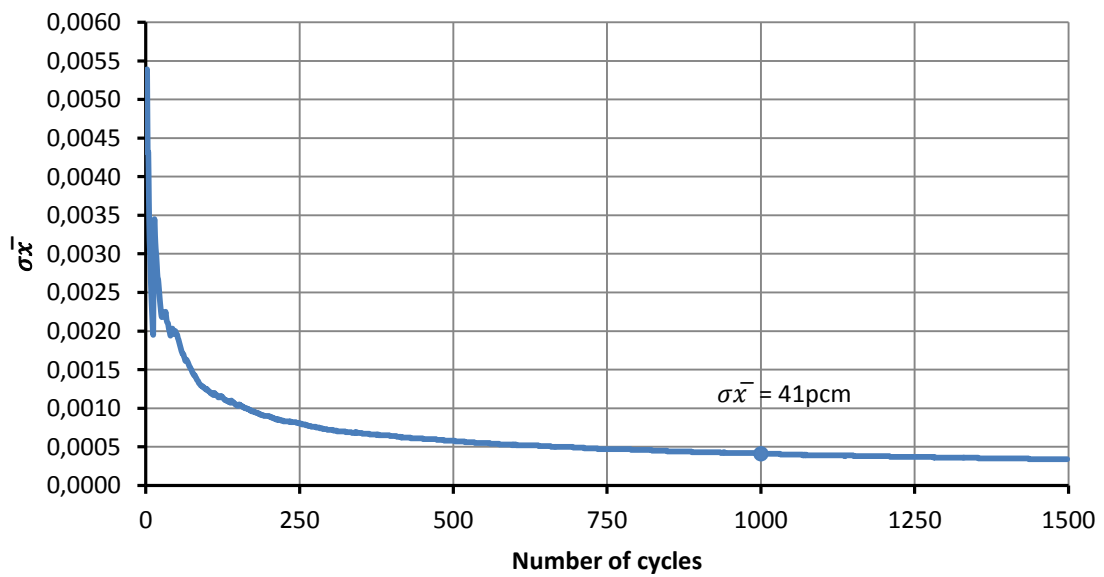


Figure 5.4. $\sigma_{\bar{x}}$ using Analog k_{eff} estimation

- Implicit k_{eff} estimation

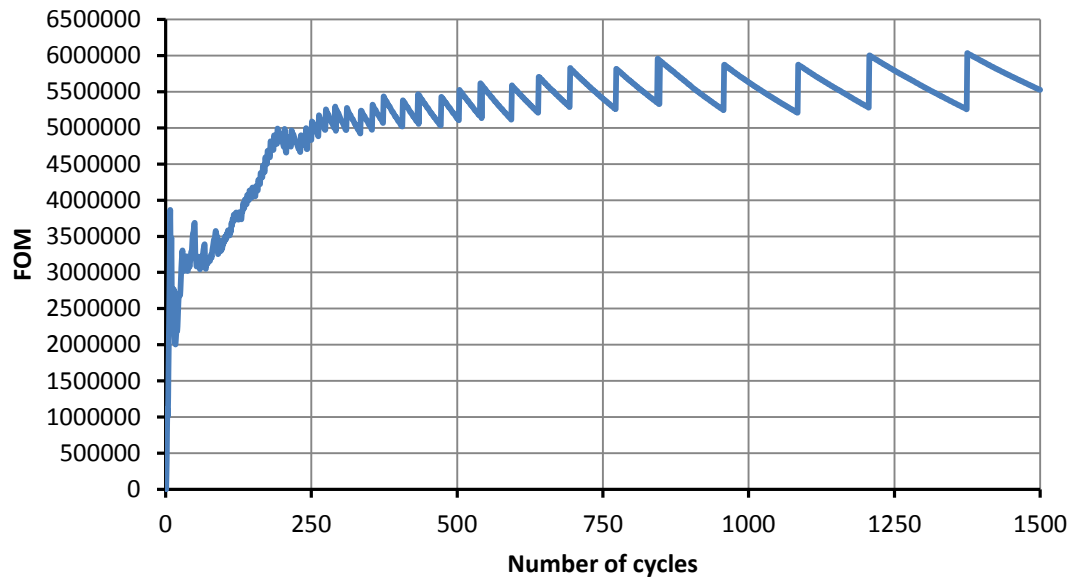


Figure 5.5. FOM using Implicit k_{eff} estimation

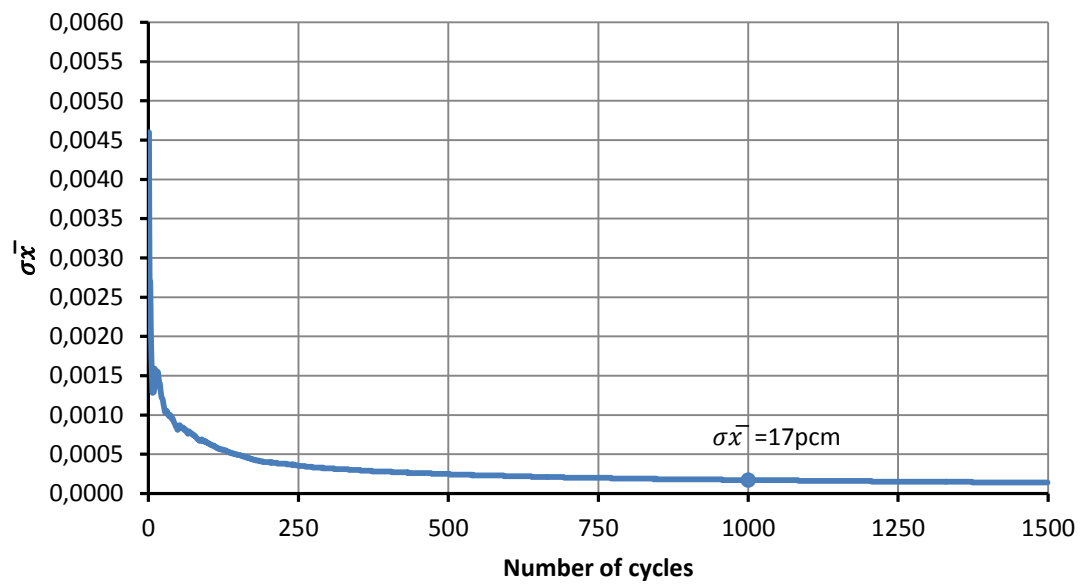


Figure 5.6. $\sigma_{\bar{x}}$ using Implicit k_{eff} estimation

As shown in Figure 5.3 and Figure 5.5, SERPENT achieves a constant FOM rapidly, which means that it does not need so many cycles to become effectiveness. As expected, this constant shape is achieved in both cases; however, the analog estimation FOM curve requires less cycles to obtain its maximum value and seems to be more stable than the implicit estimation. On the other hand, the use of the implicit estimation reduces significantly the uncertainty in the solution and increases the maximum FOM value.

The FOM curve performs a slightly rippled shape, but this is an expected behavior that does not compromise the stability or the methodology efficiency, being only a matter of the precision with which the uncertainty has been given by the output. The difference between two uncertainty values is not that precise in these simulations (1pcm) to change its value very frequently in time, so when it changes the FOM curve shows a detectable discrete jump.

Table 5.1 gathers the relevant information extracted from the Figures 5.3, 5.4, 5.5 and 5.6.

	Analog k_{eff} estimation	Implicit k_{eff} estimation
FOM maximum value stabilizes?	Yes (very stable)	Yes (stable)
Number of cycles required to achieve the maximum FOM value	500 cycles	900 cycles
Maximum FOM value	950.000	5.500.000
$\sigma_{\bar{x}}$ after 1000 cycles	41pcm	17pcm

Table 5.1. Comparison between analog and implicit k_{eff} estimations

In the view of these results, the implicit k_{eff} estimation is considered to be more interesting because, although it does not stabilizes as fast as the analog k_{eff} estimation, does it in a FOM value (effectiveness) more than 5 times higher and achieving a $\sigma_{\bar{x}}$ lower than a half. In addition, although a minimum of 900 cycles will be required to run the simulations, this is not an exaggerated value, which would be also needed by using the analog k_{eff} estimation if looking for some good precision in the results. Therefore, a **1000 cycles** simulation is considered adequate to obtain a solution using implicit k_{eff} estimation.

5.1.2. Number of cycles and neutron population

A good accuracy is only achieved by working with a faithful model, so the systematic error cannot be decreased by changing any of the simulation parameters. However, precision (unlike accuracy) is enhanced by reducing $\sigma_{\bar{x}}$, which is mainly determined by the number of sampled histories (N) used to run the simulation (i.e. the number of cycles and the neutron population).

Although error in the response decreases by using a large amount of neutrons, time of calculation is significantly increased as well. Hence, in order to decide an appropriate neutron population, some simulations of the 13x13 FCM fuel assembly have been done using 1000 cycles and different number of neutron population, which are compared by using the FOM and the $\sigma_{\bar{x}}$ obtained in their response.

- Number of cycles: **1000**
Neutron population per cycle: **25000**
Time of simulation: **35min**

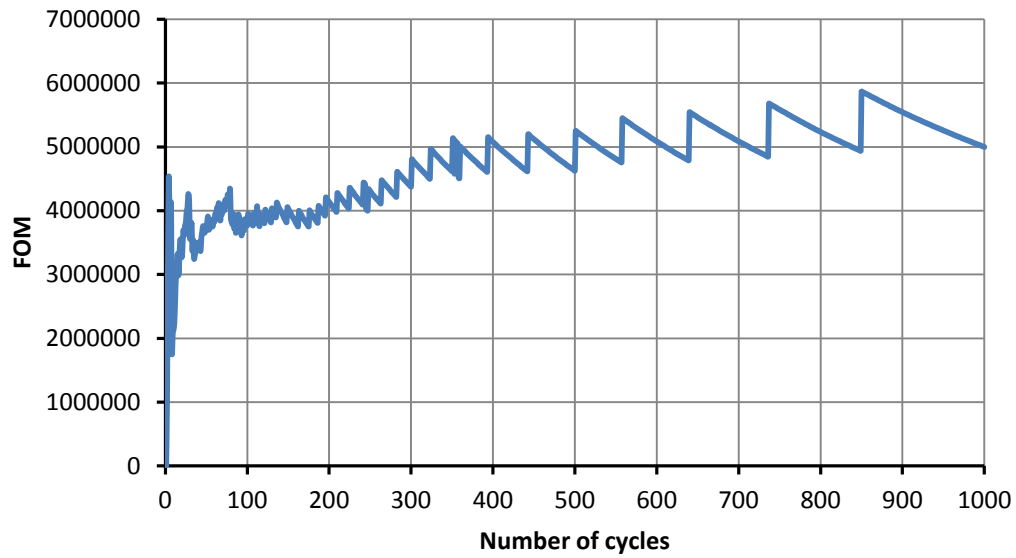


Figure 5.7. FOM for 1000 cycles and 25000 neutron population

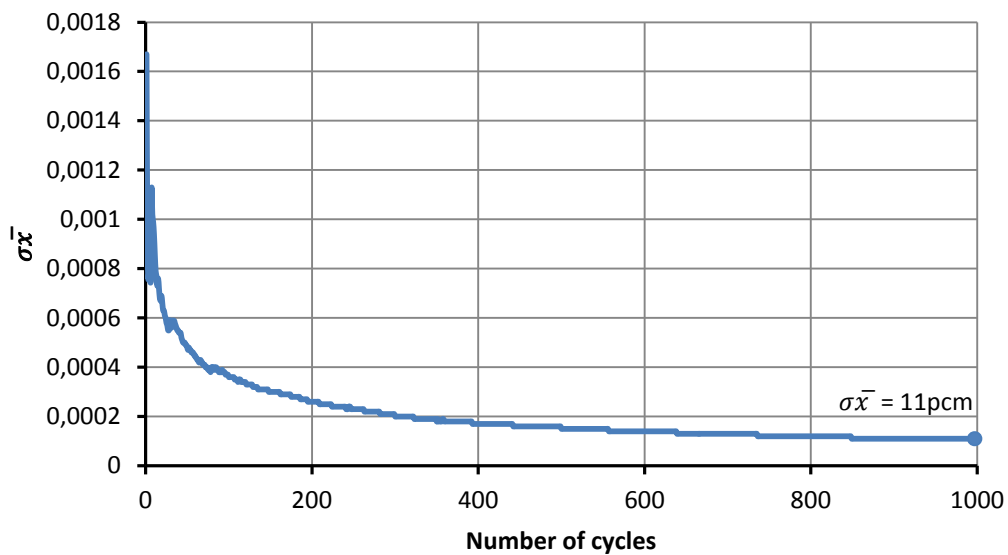


Figure 5.8. $\sigma_{\bar{x}}$ for 1000 cycles and 25000 neutron population

- Number of cycles: **1000**
Neutron population per cycle: **50000**
Time of simulation: **1h 10min**

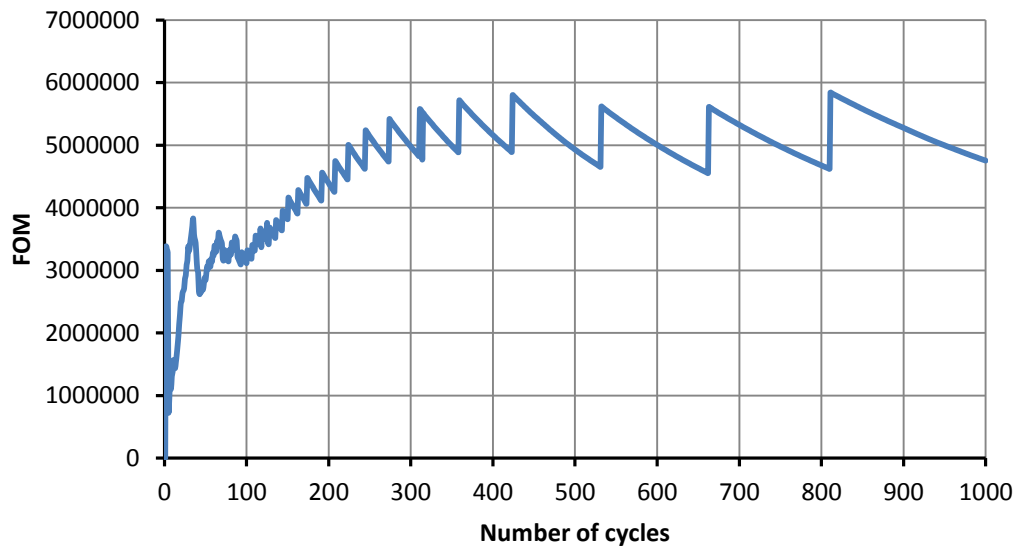


Figure 5.9. FOM for 1000 cycles and 50000 neutron population

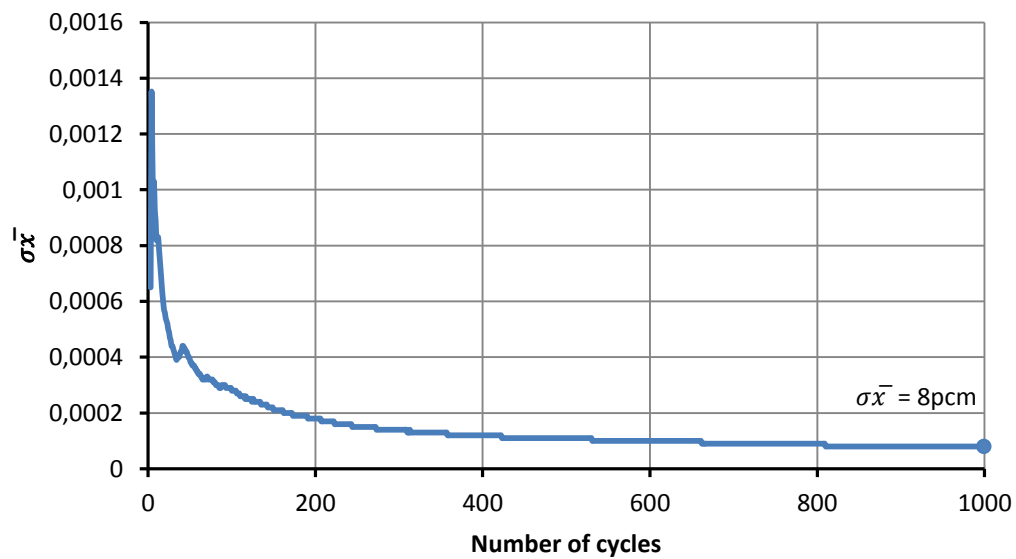


Figure 5.10. $\sigma_{\bar{x}}$ for 1000 cycles and 50000 neutron population

- Number of cycles: **1000**
Neutron population per cycle: **80000**
Time of simulation: **1h 52min**

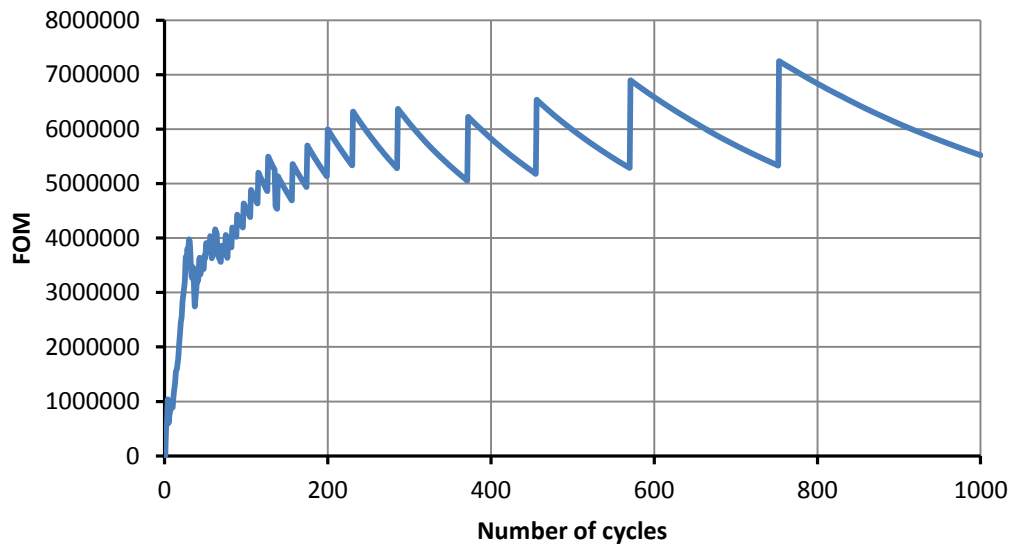


Figure 5.11. FOM for 1000 cycles and 80000 neutron population

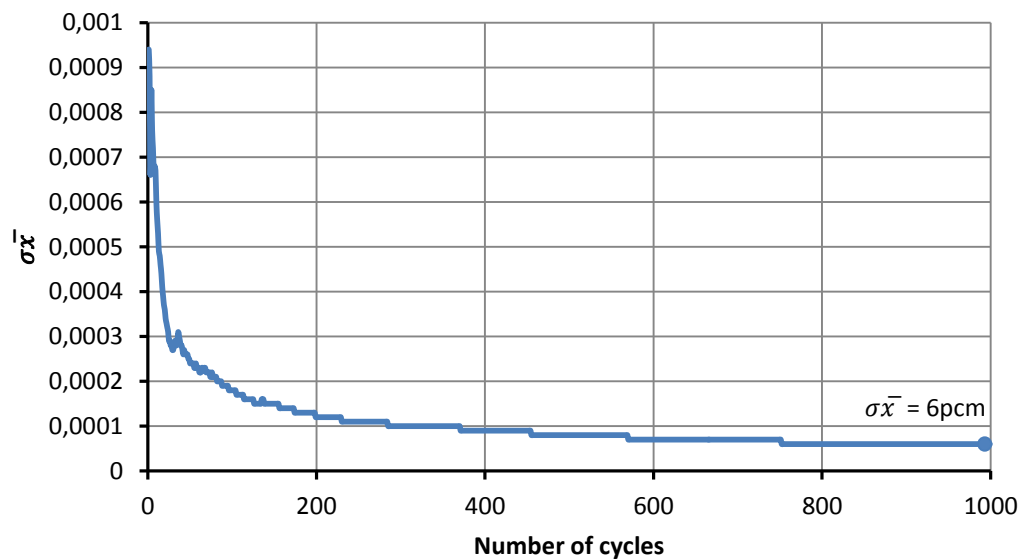


Figure 5.12. $\sigma_{\bar{x}}$ for 1000 cycles and 80000 neutron population

- Number of cycles: **1000**
Neutron population per cycle: **100000**
Time of simulation: **2h 17min**

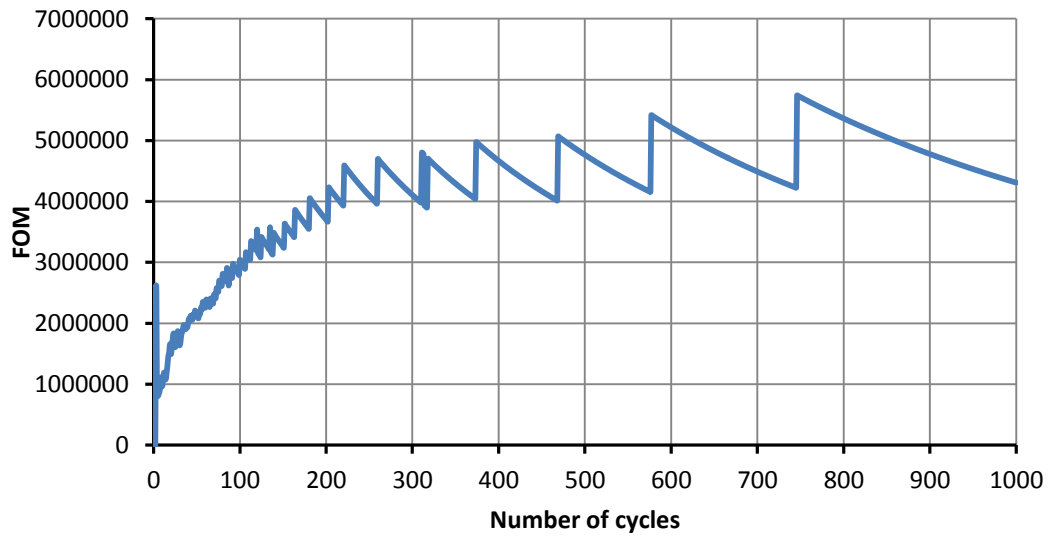


Figure 5.13. FOM for 1000 cycles and 100000 neutron population

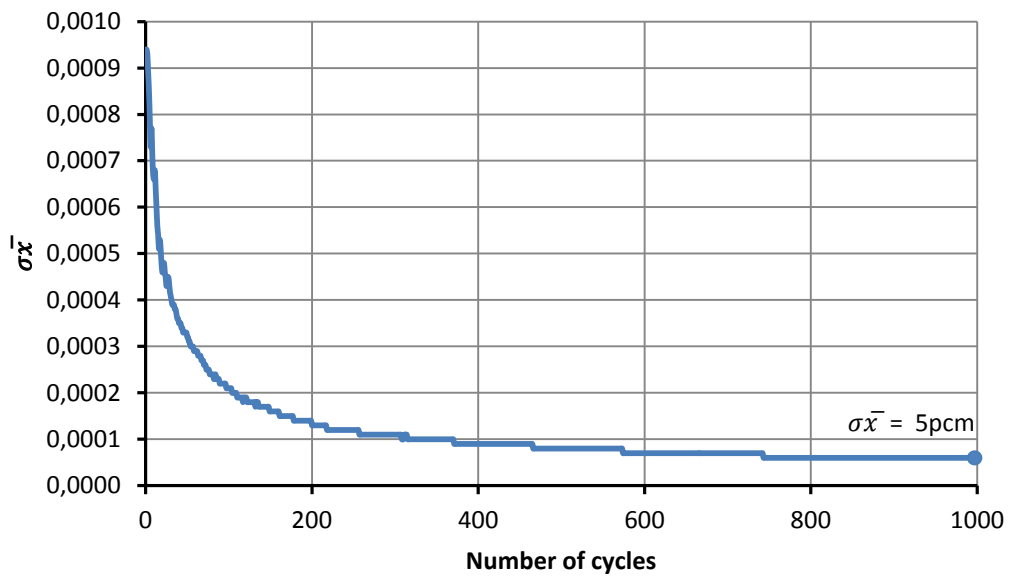


Figure 5.14. $\sigma_{\bar{x}}$ for 1000 cycles and 100000 neutron population

As shown in Figures 5.7, 5.9, 5.11 and 5.13 the FOM shape ripple becomes more significant for higher neutron population due to the reduced value of the uncertainties; however, in all cases FOM seems to stabilize in a maximum value. In regard to the error, it decreases rapidly, experiencing the larger change during the first 200 cycles, which matches with the rapid FOM value increase. However, as shown in the uncertainty labels, the precision in the results changes depending on the neutron population per cycle. Then it is necessary to define the concrete error we are willing to commit and choose the neutron population according to it, but always considering more than 900 cycles to achieve the highest FOM possible.

An **80000 neutron population** has been considered attending to achieve around 5pcm – 6pcm uncertainty in the steady-state calculation, with the aim of not obtaining higher than 10pcm uncertainties in the last steps of the burnup calculation and avoiding extremely long time calculations according to the project scope.

Finally, it's necessary to determine the number of inactive cycles, which are run before the 1000 selected active cycles. The information obtained from these inactive cycles is not used to calculate any of the results, but they are run in order to allow the initial fission source distribution to converge before starting to collect the results [33].

A large number of inactive cycles are usually needed for full-core calculations; however, this thesis is focused on fuel assembly level calculations where inactive cycles are not that important. Hence, before entering into a specific methodology to calculate the number of inactive cycles, two benchmarking simulations have been done by using 20 and 200 inactive cycles respectively, obtaining no variation in the results. In the view of this, **50 inactive cycles** have been selected, which is enough to distribute the initial fission source and not to increase uselessly the time of simulation.

5.1.3. Burnup parameters

In order to run the burnup calculation some input information must be introduced, such as the calculation method type or the number of steps the burnup calculation is divided into. These parameters are extremely influent on the obtained results, so it is interesting to run some benchmarking calculations with the aim of describing as correct as possible the desired burnup simulation.

To show the variation in the results depending on the input parameters, five simulations using the default *Chebyshev Rational Approximation Method* (CRAM) have been done, changing the number and length of the steps. The k_{eff} results obtained from these simulations are summarized in Table 5.2.

1 step		3 steps		3 steps		7 steps		11 steps	
Burnup $\left(\frac{\text{MWd}}{\text{kgHM}}\right)$	K_{eff}								
0	1.50564	0	1.50494	0	1.50516	0	1.50490	0	1.50541
120	1.06392	5	1.42554	15	1.38536	1	1.44563	1	1.44564
		30	1.32424	50	1.24761	5	1.42456	5	1.42432
		120	1.01519	120	0.983269	15	1.38329	10	1.40371
						30	1.32033	15	1.38264
						50	1.23745	30	1.31953
						85	1.09168	50	1.23698
						120	0.91729	70	1.14959
								85	1.07496
								95	1.01849
								110	0.92936
								120	0.85947

Table 5.2. Different number and length steps burnup calculation

As showed, the k_{eff} changes significantly depending on the number of steps and depending on the length step used. However, another previous comparison has been done in order to check if these differences are influenced by the methodology used to run the burnup calculation.

The SERPENT code has two methods for solving the Bateman equations describing the changes in the isotopic compositions caused by neutron-induced reactions and radioactive decay [33]: The Transmutation Trajectory Analysis (TTA), which calculates the analytical solution of linearized transmutation chains, and the Chebyshev Rational Approximation Method (CRAM), which calculates a matrix exponential solution. Same simulations have been done by using both methodologies in order to check if they produce different results (see Table 5.3).

TTA method							
1 step		3 steps		3 steps		7 steps	
Burnup $\left(\frac{\text{MWd}}{\text{kgHM}}\right)$	K_{eff}	Burnup $\left(\frac{\text{MWd}}{\text{kgHM}}\right)$	K_{eff}	Burnup $\left(\frac{\text{MWd}}{\text{kgHM}}\right)$	K_{eff}	Burnup $\left(\frac{\text{MWd}}{\text{kgHM}}\right)$	K_{eff}
0	1.50541	0	1.50565	0	1.50546	0	1.50553
120	1.06416	5	1.42558	15	1.38566	1	1.44545
		30	1.32403	50	1.24757	5	1.42462
		120	1.01545	120	0.983289	15	1.38303
						30	1.32027
						50	1.23749
						85	1.09174
						120	0.917320

CRAM method							
1 step		3 steps		3 steps		7 steps	
Burnup $\left(\frac{\text{MWd}}{\text{kgHM}}\right)$	K_{eff}	Burnup $\left(\frac{\text{MWd}}{\text{kgHM}}\right)$	K_{eff}	Burnup $\left(\frac{\text{MWd}}{\text{kgHM}}\right)$	K_{eff}	Burnup $\left(\frac{\text{MWd}}{\text{kgHM}}\right)$	K_{eff}
0	1.50538	0	1.50550	0	1.50556	0	1.50541
120	1.06385	5	1.42541	15	1.38556	1	1.44558
		30	1.32420	50	1.24784	5	1.42459
		120	1.01532	120	0.983190	15	1.38324
						30	1.32044
						50	1.23743
						85	1.09180
						120	0.917285

Table 5.3. Comparison between TTA method and CRAM method

Table 5.3 shows no significant differences between both methodologies, obtaining similar results for the same burnup step case. However, the simulation using CRAM method is a bit faster than using TTA method, so the default CRAM method will be used from now on.

On the other hand, the significant influence of the number and length of the steps in the burnup calculation could be because of their significant impact on the accumulation of certain isotopes. The materials compositions and the transmutation cross sections are time-independent throughout each discrete time step, so the use of long burnup steps may produce significant errors in the results. In order to minimize this error the burnup calculation has been divided into equal length steps and the total number of steps has been increased (see Table 5.4 and 5.5). The aim of these simulations is to see if the k_{eff} converges for more detailed burnup calculations and decide the burnup step configuration will be used.

5 equal steps		10 equal steps		15 equal steps		20 equal steps	
<i>Burnup</i> $\left(\frac{MWd}{kgHM}\right)$	K_{eff}	<i>Burnup</i> $\left(\frac{MWd}{kgHM}\right)$	K_{eff}	<i>Burnup</i> $\left(\frac{MWd}{kgHM}\right)$	K_{eff}	<i>Burnup</i> $\left(\frac{MWd}{kgHM}\right)$	K_{eff}
0	1.50531	0	1.50543	0	1.50560	0	1.50549
24	1.35015	12	1.39727	8	1.41357	6	1.42160
48	1.25173	24	1.34597	16	1.37909	12	1.39568
72	1.14934	36	1.29504	24	1.34448	18	1.36995
96	1.03390	48	1.24336	32	1.31028	24	1.34413
120	0.899261	60	1.18998	40	1.27553	30	1.31823
		72	1.13294	48	1.23994	36	1.29191
		84	1.07204	56	1.20384	42	1.26528
		96	1.00490	64	1.16619	48	1.23861
		108	0.930596	72	1.12695	54	1.21100
		120	0.849260	80	1.08504	60	1.18289
				88	1.04042	66	1.15386
				96	0.993037	72	1.12338
				104	0.942029	78	1.09207
				112	0.886777	84	1.05844
				120	0.828322	90	1.02366
						96	0.986589
						102	0.947629
						108	0.906217
						114	0.862644
						120	0.816711

Table 5.4. Burnup calculation for k_{eff} convergence (5 to 20 equal steps)

30 equal steps		40 equal steps		60 equal steps			
$Burnup$ $\left(\frac{MWd}{kgHM}\right)$	K_{eff}	$Burnup$ $\left(\frac{MWd}{kgHM}\right)$	K_{eff}	$Burnup$ $\left(\frac{MWd}{kgHM}\right)$	K_{eff}	$Burnup$ $\left(\frac{MWd}{kgHM}\right)$	K_{eff}
0	1.50564	0	1.50541	0	1.50546	62	1.16829
4	1.42920	3	1.43361	2	1.43847	64	1.15805
8	1.41237	6	1.42033	4	1.42833	66	1.14778
12	1.39548	9	1.40807	6	1.42017	68	1.13745
16	1.37816	12	1.39521	8	1.41187	70	1.12728
20	1.36104	15	1.38212	10	1.40339	72	1.11652
24	1.34314	18	1.36967	12	1.39487	74	1.10579
28	1.32594	21	1.35619	14	1.38611	76	1.09477
32	1.30844	24	1.34284	16	1.37749	78	1.08358
36	1.29045	27	1.32962	18	1.36909	80	1.07226
40	1.27269	30	1.31653	20	1.36046	82	1.06105
44	1.25476	33	1.30332	22	1.35156	84	1.04884
48	1.23656	36	1.28990	24	1.34254	86	1.03663
52	1.21814	39	1.27663	26	1.33367	88	1.02451
56	1.19969	42	1.26331	28	1.32504	90	1.01217
60	1.18054	45	1.24978	30	1.31627	92	0.999575
64	1.16073	48	1.23593	32	1.30747	94	0.986228
68	1.14096	51	1.22212	34	1.29831	96	0.972922
72	1.12033	54	1.20764	36	1.28956	98	0.959257
76	1.09869	57	1.19347	38	1.28054	100	0.945487
80	1.07662	60	1.17917	40	1.27161	102	0.931503
84	1.05393	63	1.16437	42	1.26214	104	0.916954
88	1.03028	66	1.14950	44	1.25320	106	0.902037
92	1.00602	69	1.13415	46	1.24401	108	0.886943
96	0.979853	72	1.11817	48	1.23492	110	0.871620
100	0.953428	75	1.10237	50	1.22579	112	0.856086
104	0.925617	78	1.08583	52	1.21615	114	0.840006
108	0.896827	81	1.06867	54	1.20675	116	0.823818
112	0.866970	84	1.05136	56	1.19728	118	0.807502
116	0.836192	87	1.03385	58	1.18746	120	0.790976
120	0.804447	90	1.01518	60	1.17809		
		93	0.996065				
		96	0.976785				
		99	0.956256				
		102	0.935562				
		105	0.914229				
		108	0.892127				
		111	0.869385				
		114	0.846048				
		117	0.822081				
		120	0.798103				

Table 5.5. Burnup calculation for k_{eff} convergence (30 to 60 equal steps)

First important aspect to notice is that the accumulated error is reduced by using equal length steps instead of using any other step configuration, even for the same number of steps. Secondly, Table 5.4 and Table 5.5 show that for more detailed burnup calculations the accumulated error is reduced and k_{eff} seems to converge. In order to decide the step configuration for future burnup calculations, these results are plotted in Table 5.6 and Figure 5.15 to show how k_{eff} changes by adding more steps and detailing the burnup calculation.

Number of steps	Step length $\left(\frac{MWd}{kgHM}\right)$	k_{eff} (last step)
5	24	0,899261
10	12	0,84926
15	8	0,828322
20	6	0,816711
30	4	0,804447
40	3	0,798103
60	2	0,790976

Table 5.6. Number of steps and step length comparison

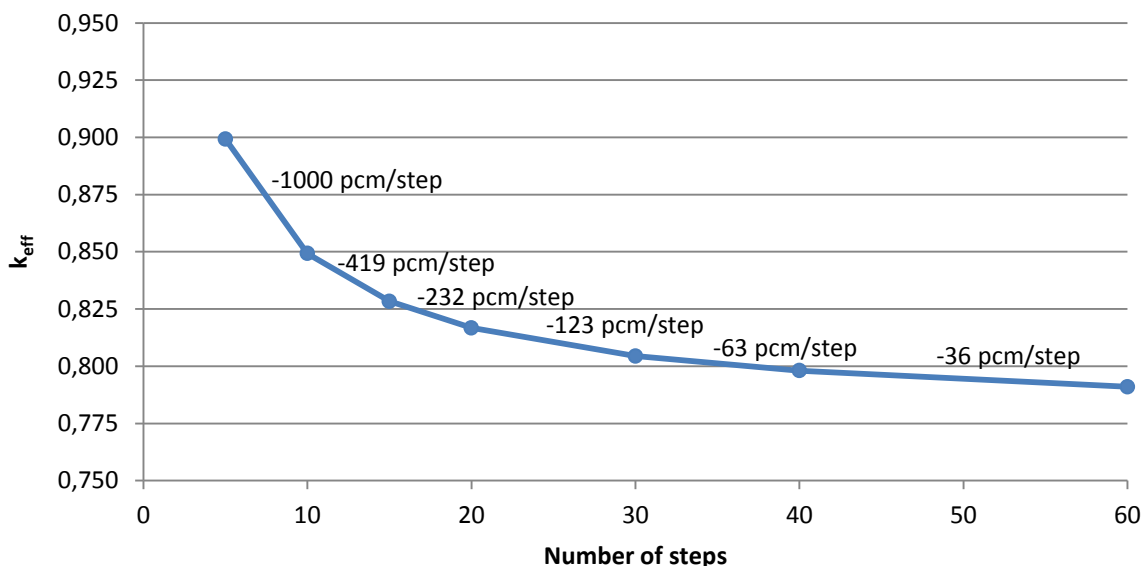


Figure 5.15. Number of steps influence on last step result

As long as the burnup calculation becomes more detailed, the change in the k_{eff} per added step is reduced because the step length becomes closer between the simulations. It must be also taken into account that calculation time increases linearly with the number of steps, so for a large number of steps the k_{eff} will almost converge whereas simulation time will increase significantly. It has been decided to use a **3MWd/kgHM** step length for the burnup calculations, which gives an almost converged k_{eff} value without overly increasing time calculation according to the project scope.

5.2. TRISO particles modeling comparison

The aim of this section is to analyze whether the results obtained using the explicit particle/pebble bed fuel model to define the TRISO particles have significant differences compared to the results obtained using the infinite 3D lattice. As explained in Chapter 4, the regular 3D arrangement (see Figure 5.16) can be described in the input file, but the explicit model requires an extra file describing the concrete coordinates of the TRISO particles inside the geometry.

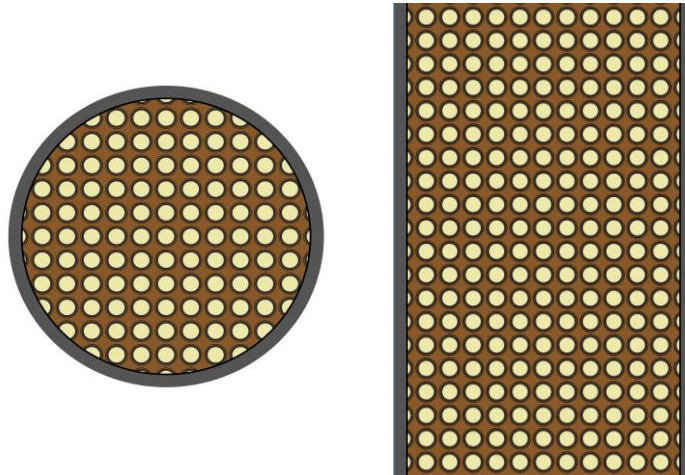


Figure 5.16. Regular distribution of TRISO using an infinite 3D lattice

This coordinates distribution is wanted to be random in order to be as close to a reality as possible. However, this first idea fails because when approximately the 10% of the TRISO particles remain to be located during the random distribution process, it becomes impossible to add any more particle without touching the already located TRISO particles or the geometry boundaries. This is due to the packing fraction value (40%), which represents an important distribution density of TRISO particles. Thus, TRISO particles require to be slightly ordered to be located inside the fuel pin geometry. The strategy adopted to avoid this problem is to completely fill the fuel pin with the maximum amount of TRISO particles possible, and afterwards randomly extract some of them until achieving the desired 40% packing fraction (see Figure 5.17).

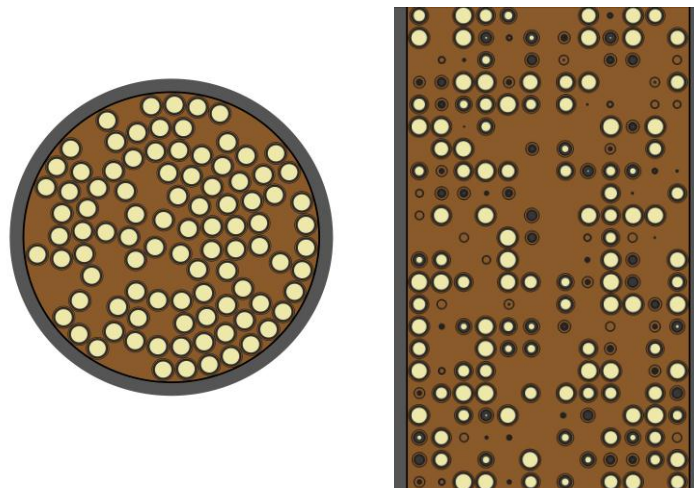


Figure 5.17. Random distribution of TRISO using explicit model

By using this methodology a more random TRISO particles distribution is achieved compared to the infinite 3D lattice methodology and, in addition, the problem of cutting the particles by the outer boundary is avoided.

It is desired to check if this detailed description of the geometry produces significant differences in the results. With this objective, a same standard burnup calculation has been simulated by using the 3D lattice modeling and the explicit particle model, achieving their reactivity values along burnup as shown in Figure 5.18 and Table 5.7.

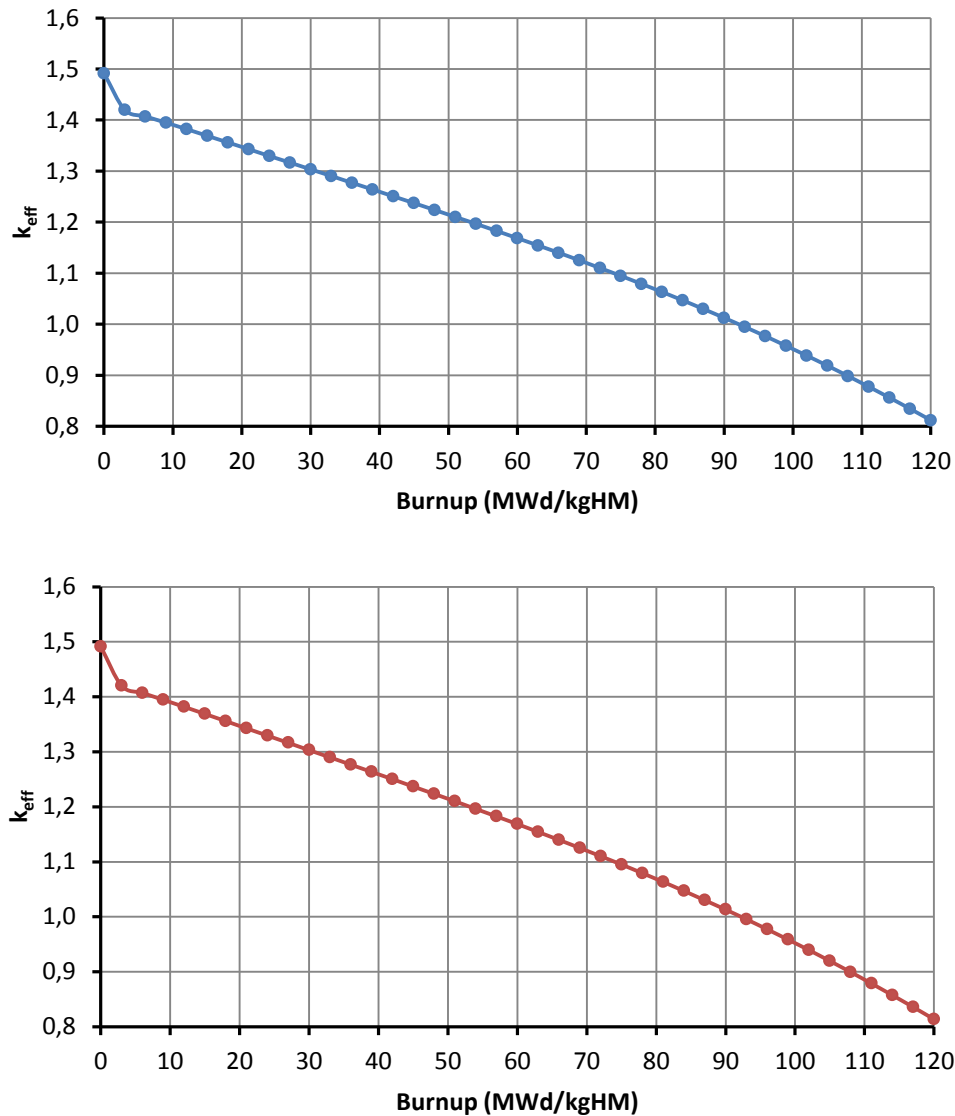


Figure 5.18. 3D lattice and explicit model reactivity curves comparison

In the light of the reactivity curves, similar k_{eff} values are obtained from both types of TRISO particles description at a fuel assembly level. However, the calculation time increases significantly (about 30%) if the detailed explicit model is used, so a regular 3D array will be used from now on. Anyway, it is important to notice that only the reactivity curves have been benchmarked, so a more exhaustive comparison could be interesting for future analyses.

EFPD (days)	Burnup ($\frac{MWd}{kgHM}$)	3D lattice		Explicit model	
		k_{eff}	$\sigma_{\bar{x}}$ (pcm)	k_{eff}	$\sigma_{\bar{x}}$ (pcm)
0,00	0	1,491380	±4	1,491100	±4
23,18	3	1,420120	±4	1,420110	±4
46,37	6	1,407170	±4	1,407050	±4
69,55	9	1,394780	±4	1,394530	±4
92,73	12	1,382110	±4	1,381760	±4
115,92	15	1,369030	±4	1,368840	±4
139,10	18	1,356030	±4	1,355750	±4
162,29	21	1,342940	±4	1,342520	±4
185,47	24	1,329610	±4	1,329410	±4
208,65	27	1,316600	±4	1,316290	±4
231,84	30	1,303400	±4	1,303010	±4
255,02	33	1,290320	±4	1,289950	±4
278,20	36	1,277010	±4	1,276670	±4
301,39	39	1,263890	±4	1,263450	±4
324,57	42	1,250540	±5	1,250300	±4
347,76	45	1,237270	±4	1,236760	±5
370,94	48	1,223770	±5	1,223520	±5
394,12	51	1,210200	±5	1,210040	±5
417,31	54	1,196590	±5	1,196190	±5
440,49	57	1,182710	±5	1,182440	±5
463,67	60	1,168560	±5	1,168560	±5
486,86	63	1,154350	±5	1,154240	±5
510,04	66	1,140040	±5	1,139770	±5
533,23	69	1,125180	±5	1,125140	±5
556,41	72	1,110100	±5	1,110130	±5
579,59	75	1,094850	±5	1,095020	±5
602,78	78	1,079130	±5	1,079360	±5
625,96	81	1,063170	±5	1,063400	±5
649,14	84	1,046770	±5	1,046870	±5
672,33	87	1,029850	±5	1,030080	±5
695,51	90	1,012650	±5	1,013050	±5
718,69	93	0,994759	±5	0,995399	±5
741,88	96	0,976578	±6	0,977158	±6
765,06	99	0,957747	±6	0,958480	±6
788,25	102	0,938493	±5	0,939472	±5
811,43	105	0,918787	±6	0,919704	±6
834,61	108	0,898432	±6	0,899523	±6
857,80	111	0,877550	±6	0,878757	±6
880,98	114	0,856211	±6	0,857498	±6
904,16	117	0,834356	±6	0,835905	±6
927,35	120	0,812056	±6	0,813815	±6

Table 5.7. 3D lattice and explicit model comparison

Chapter 6

Results and discussion

In this section, all the results from the simulations are included and discussed in two separate sections: The reactivity curves analysis and the safety parameters analysis. The latter includes the calculations for the already introduced MTC, FTC and CVR safety parameters.

6.1. Reactivity curves

The first benchmarking step between the 17x17 Westinghouse UO₂ fuel assembly and the designed 13x13 FCM fuel assembly is a reactivity analysis along the fuel cycle (see Table 6.1). For the original configuration, this analysis is run from the steady state calculation until fuel is typically discharged from the reactor, i.e. 50 MWd/kgHM; whereas for the FCM fuel assembly calculation it has been run until the typical discharge value of the LEU TRISO particles used in HTGR, i.e. 120 MWd/kgHM [15]. Same step length has been used for both burnup calculations, i.e. 3MWd/kgHM, as calculated in Chapter 5.

Before analyzing k_{eff} behavior in both fuel assemblies, it must be noticed that burnup ratio is highly increased by the use of FCM fuel. As plotted in Figure 6.1, after same effective full-power days (EFPD) higher burnup rates are obtained from the FCM fuel than for the UO₂ configuration, which is due to the difference between the heavy metal (HM)³⁰ mass introduced in them. As explained before, the same total power is produced by both fuel assemblies and same amount of fissile ²³⁵U mass is introduced in them. However, the compatibility study showed that the use of FCM fuel requires higher enrichments, leading to a lower total heavy metal mass and thus increasing burnup rate although working the same EFPD at the same power.

³⁰ It refers to the total Uranium mass (²³⁵U + ²³⁸U)

17x17 Westinghouse FA				13x13 FCM FA			
<i>EFPD</i> (days)	<i>Burnup</i> $\left(\frac{MWd}{kgHM}\right)$	k_{eff}	$\sigma_{\bar{x}}$ (pcm)	<i>EFPD</i> (days)	<i>Burnup</i> $\left(\frac{MWd}{kgHM}\right)$	k_{eff}	$\sigma_{\bar{x}}$ (pcm)
0,00	0	1,33903	±5	0,00	0	1,49138	±4
75,93	3	1,25575	±5	23,18	3	1,42012	±4
151,85	6	1,22046	±5	46,37	6	1,40717	±4
227,78	9	1,18771	±5	69,55	9	1,39478	±4
303,71	12	1,15728	±5	92,73	12	1,38211	±4
379,63	15	1,12897	±5	115,92	15	1,36903	±4
455,56	18	1,10259	±6	139,10	18	1,35603	±4
531,49	21	1,07719	±6	162,29	21	1,34294	±4
607,41	24	1,05296	±6	185,47	24	1,32961	±4
683,34	27	1,02938	±6	208,65	27	1,31660	±4
759,27	30	1,00692	±6	231,84	30	1,30340	±4
835,19	33	0,985036	±6	255,02	33	1,29032	±4
911,12	36	0,963656	±6	278,20	36	1,27701	±4
987,05	39	0,943252	±7	301,39	39	1,26389	±4
1062,97	42	0,923505	±7	324,57	42	1,25054	±5
1138,90	45	0,904777	±7	347,76	45	1,23727	±4
1214,83	48	0,886782	±7	370,94	48	1,22377	±5
1290,75	51	0,869819	±7	394,12	51	1,21020	±5
				417,31	54	1,19659	±5
				440,49	57	1,18271	±5
				463,67	60	1,16856	±5
				486,86	63	1,15435	±5
				510,04	66	1,14004	±5
				533,23	69	1,12518	±5
				556,41	72	1,11010	±5
				579,59	75	1,09485	±5
				602,78	78	1,07913	±5
				625,96	81	1,06317	±5
				649,14	84	1,04677	±5
				672,33	87	1,02985	±5
				695,51	90	1,01265	±5
				718,69	93	0,994759	±5
				741,88	96	0,976578	±6
				765,06	99	0,957747	±6
				788,25	102	0,938493	±5
				811,43	105	0,918787	±6
				834,61	108	0,898432	±6
				857,80	111	0,877550	±6
				880,98	114	0,856211	±6
				904,16	117	0,834356	±6
				927,35	120	0,812056	±6

Table 6.1. Burnup calculation for the 17x17 Westinghouse FA and the 13x13 FCM FA

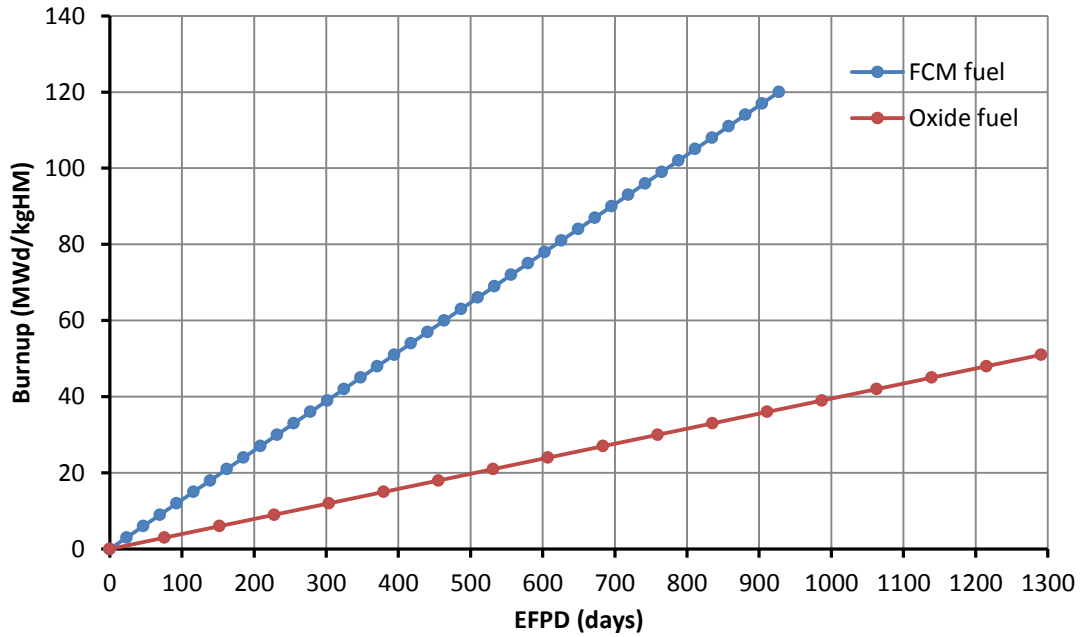


Figure 6.1. Burnup curves versus EFPD

This characteristic is also shown in Figure 6.2 by representing neutron multiplication factor versus burnup. A higher discharge burnup is achieved because the new fuel assembly configuration allows achieving higher potential k_{eff} values for same burnup rates, so fuel can be used in the reactor beyond 50MWd/kgHM, almost until 120MWd/kgHM as in HTGR.

It is also noticed that both curves present a rapid k_{eff} decrease between the two first steps of simulation. This is due to the fast accumulation of generated fission products such as ^{135}Xe or ^{149}Sm , which act as neutron absorbers and decrease k_{eff} .

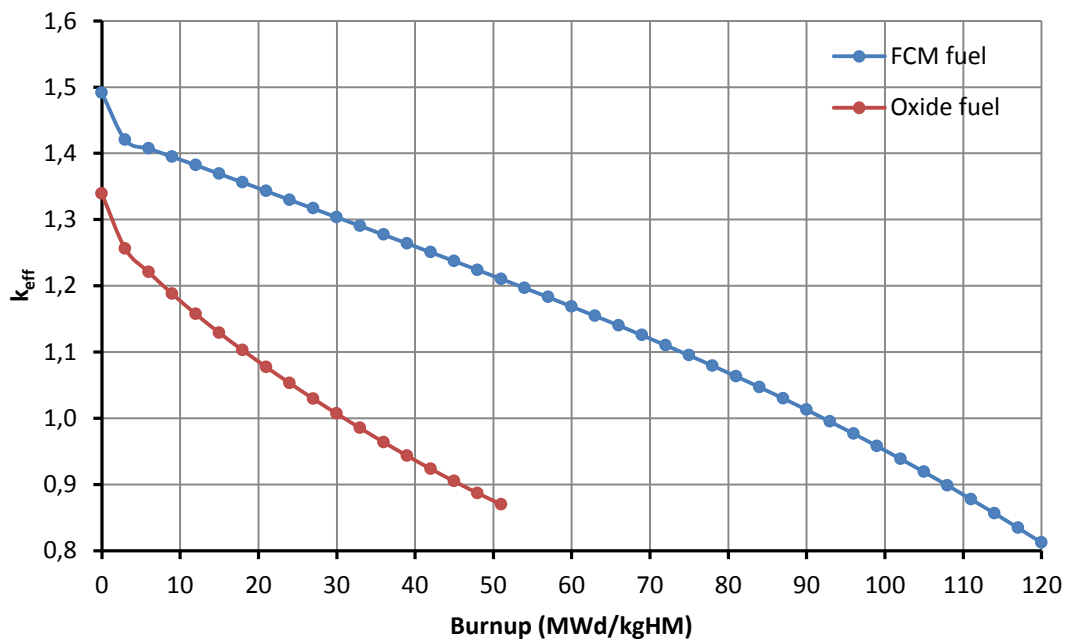


Figure 6.2. Reactivity curves versus burnup

Moreover, a very interesting representation to compare reactivity curves of both fuel assemblies is to plot the k_{eff} versus EFPD with the aim of benchmarking their depletion rate (see Figure 6.3).

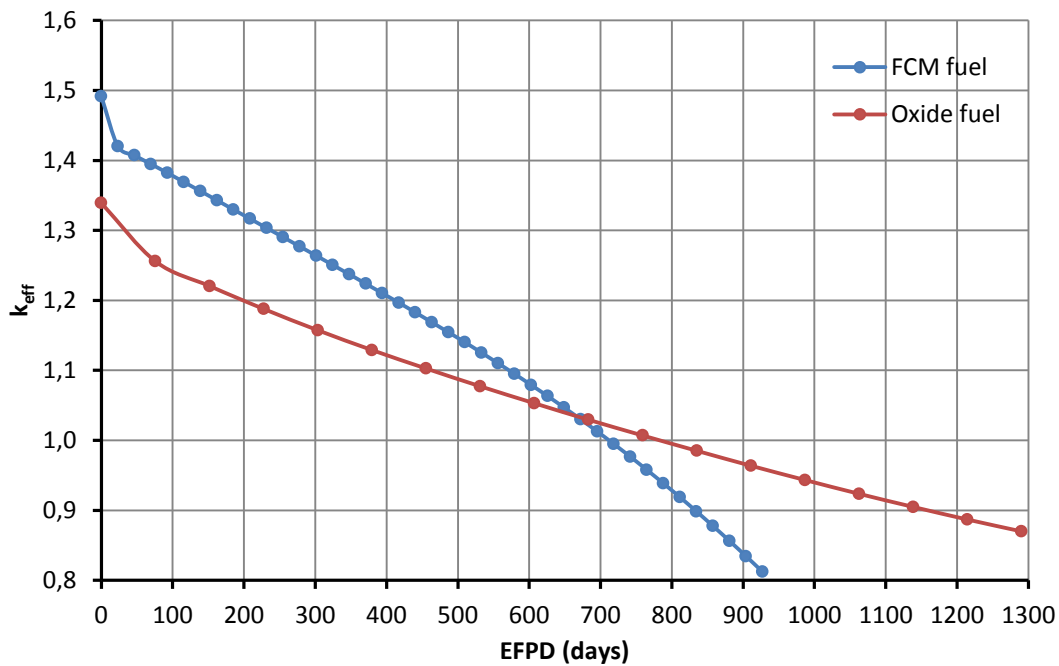


Figure 6.3. Depletion rate comparison

At BOL, significant higher k_{eff} values are obtained from the FCM fuel configuration mainly because of two reasons.

In first place, because the higher fuel enrichment and the non-reactive SiC matrix around TRISO particles leads to a significant lack of self-shielding in the FCM fuel. For the original UO_2 pellet, the already thermalized neutron tends to interact with fuel atoms located close to the external surface of the pellet, making it difficult to arrive to the center part of the fuel without undergoing any interaction in the way. On the case of the FCM fuel, due to SiC neutron transparency and a higher ^{235}U mass per unit fuel volume, the probability of interaction with the inner part of the fuel increases.

The second reason is the significant amount of Carbon (C) in the TRISO particles layers and SiC matrix in FCM fuel, which acts as a moderator and enhances the thermalization process. This effect combined with a lower amount of ^{238}U in the fuel leads to increase the resonance escape probability (ρ) (see Figure 6.4), increasing significantly k_{eff} .

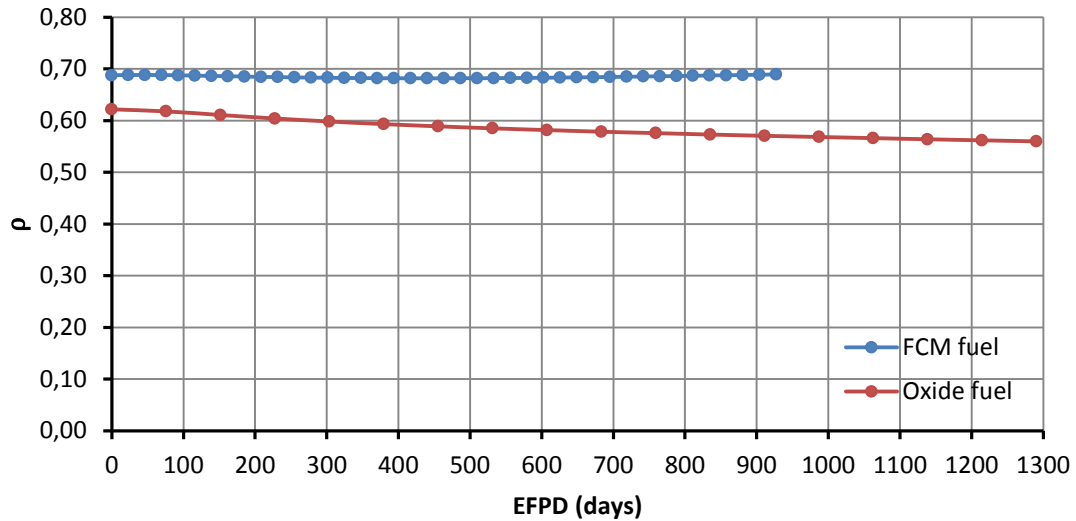


Figure 6.4. Resonance escape probability (ρ) comparison

However, although these characteristics are present during the whole cycle, Figure 6.3 showed that FCM fuel depletion rate is very stiff comparing with the UO_2 fuel, even arriving to obtain a lower k_{eff} after 700 days. This behavior is not expected at first because both fuel assemblies must have produced the same total energy after same number of days as long as working at same power, so FCM fuel should not seem to run out that fast compared to oxide fuel. One of the reasons of this behavior is that FCM fuel depletes faster the fissile ^{235}U isotope along the cycle compared to UO_2 fuel. This happens because ^{235}U fission represents a larger contribution to the total energy for in the FCM fuel configuration than in oxide fuel, reducing rapidly the total amount of fissile material (see Figure 6.5).

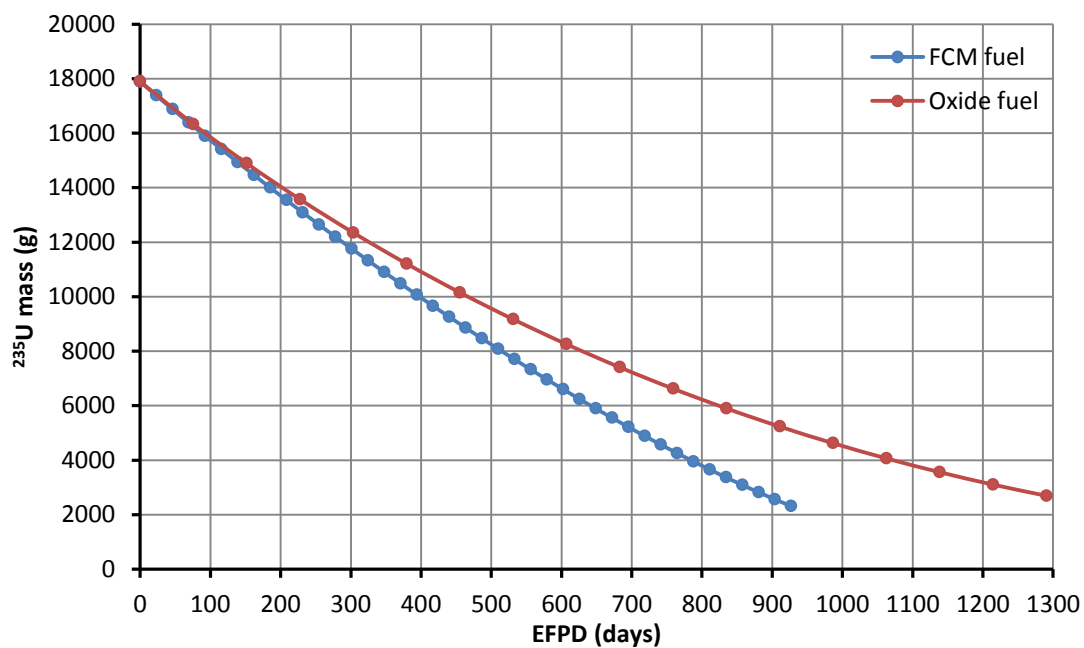


Figure 6.5. ^{235}U depletion

On the other hand, for oxide fuel a larger fraction of the energy comes from the fission of some transuranic elements (TRU) such as ^{239}Pu and ^{241}Pu , leading to not need that much ^{235}U fissions to produce the same energy as the FCM fuel. This is due to the higher quantity of ^{238}U in the oxide fuel composition, which reduces resonance escape probability and increases its neutron capture rate, leading to breed more plutonium than the FCM fuel (see Figure 6.6).

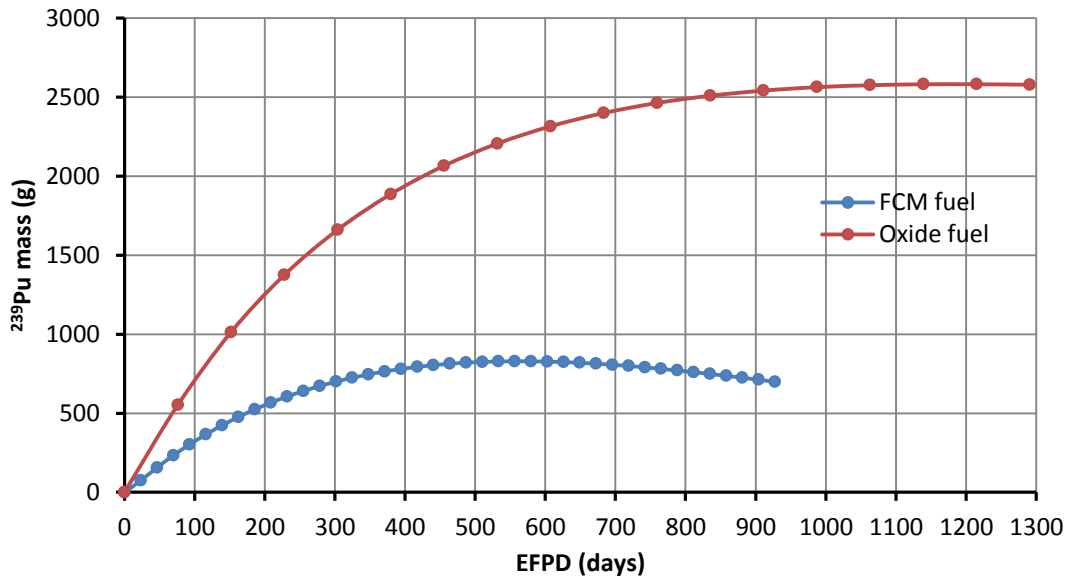


Figure 6.6. ^{239}Pu mass versus EFPD

Summarizing, it can be said that FCM fuel does not breed that much plutonium as the oxide fuel, reducing neutron economy since almost all the energy is produced from ^{235}U fission, and thus leading to reduce cycle length significantly. On the other hand, FCM fuel is very interesting in a non-proliferation point of view and its higher discharged burnup and lower TRU generation is advantageous in the way of reducing nuclear waste at final disposal.

6.2. Safety parameters

6.2.1. MTC

The Moderator Temperature Coefficient (MTC) is the first safety parameter to be analyzed, and the procedure followed for its calculation is explained in more detail than for the other coefficients, which are calculated similarly. MTC measures the change on reactivity caused by a change in moderator temperature, so it is necessary to translate k_{eff} information into reactivity (ρ) terms before calculating MTC (6.1).

$$\rho = \frac{k_{\text{eff}} - 1}{k_{\text{eff}}} \quad (6.1)$$

However, the uncertainty in the k_{eff} solution cannot be directly applied to ρ , and it is necessary to use the Propagation of Error Formula (6.2) in order to calculate its uncertainty $\sigma(\rho)$:

$$\sigma(f(y_i)) = \sqrt{\sum_i \left(\frac{\partial f}{\partial y_i} \cdot \sigma(y_i) \right)^2} \quad (6.2)$$

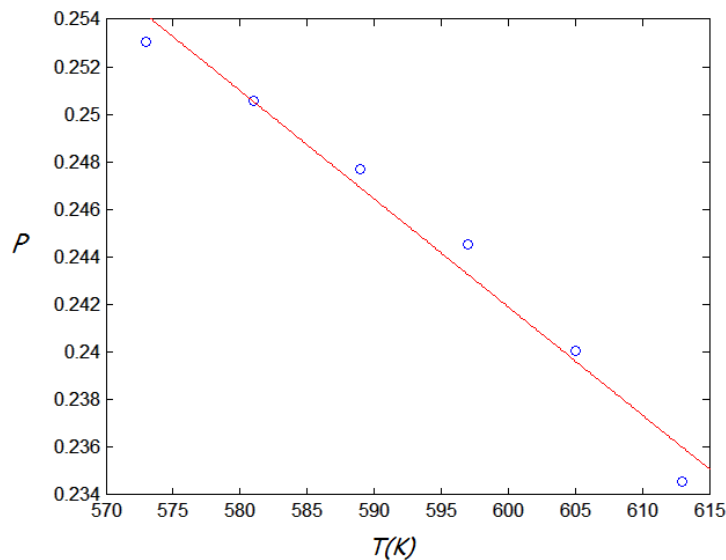
In this case, the Propagation of Error Formula would be applied as follows:

$$\sigma(\rho) = \sigma(f(k_{eff})) = \sqrt{\sum \left(\frac{\partial f(k_{eff})}{\partial k_{eff}} \cdot \sigma(k_{eff}) \right)^2} = \frac{\sigma(k_{eff})}{k_{eff}^2}$$

Where,

$$\rho = f(k_{eff})$$

ρ value is basically influenced by the water density, which varies significantly by a change of its temperature. Hence, it has been considered a range of interest for the MTC calculation, which includes temperatures between 573K (average work temperature) and 613K (saturation temperature). However, ρ variation with water density happens in such a way that makes it difficult to find an appropriate relationship between ρ and water temperatures in the range of interest. Consequently, it has been considered a good approach to calculate MTC as the slope of a linear regression fitted to the k_{eff} values obtained for the temperatures within the range of interest (see Figure 6.7).



Note: The uncertainties of the values are less than the point diameter

Figure 6.7. MTC linear fitting example

It is observed that the behavior of the fitting is almost represented by two temperature values: 573K and 605K. Therefore, and with the aim of reducing the number of burnup simulations to calculate MTC, it has been decided to fit the linear regression to the reactivity values obtained from these two temperatures. The equation of this linear regression is expressed in equation (6.3), in which must be noticed that its slope (a parameter) corresponds to the MTC value.

$$y = ax + b \quad (6.3)$$

However, the points this line fits have uncertainties associated to them, so the task is to calculate a and $\sigma(a)$ for the fitted line taking into account these uncertainties. This is done by minimizing the "S" function expressed in equation (6.4), which uses the Least Square Method but weighing the uncertainties of the points.

$$S = \sum \frac{(y_i - ax_i - b)^2}{\sigma_i^2} \quad (6.4)$$

Finally, by imposing $\frac{\partial S}{\partial a} = 0$, the wanted relationships for a and $\sigma(a)$ can be achieved as expressed in equation (6.5) and equation (6.6) [42].

$$a = \frac{\sum_i \frac{x_i y_i}{\sigma_i^2} \sum_i \frac{1}{\sigma_i^2} - \sum_i \frac{y_i}{\sigma_i^2} \sum_i \frac{x_i}{\sigma_i^2}}{\sum_i \frac{1}{\sigma_i^2} \sum_i \frac{x_i^2}{\sigma_i^2} - \left(\sum_i \frac{x_i}{\sigma_i^2} \right)^2} \quad (6.5)$$

$$\sigma(a) = \sqrt{\frac{\sum_i \frac{1}{\sigma_i^2}}{\sum_i \frac{1}{\sigma_i^2} \sum_i \frac{x_i^2}{\sigma_i^2} - \left(\sum_i \frac{x_i}{\sigma_i^2} \right)^2}} \quad (6.6)$$

After this briefly introduction to the procedure, the obtained MTC and $\sigma(MTC)$ values for all burnup steps and for both fuel assemblies are tabulated in Table 6.2 and plotted in Figure 6.8. These results are showed by dividing the fuel cycle into three time regions, in aid of its later discussion.

17x17 Westinghouse FA				13x13 FCM FA			
<i>EFPD</i> (days)	<i>Burnup</i> ($\frac{MWd}{kgHM}$)	<i>MTC</i> ($\frac{pcm}{K}$)	σ_{MTC} ($\frac{pcm}{K}$)	<i>EFPD</i> (days)	<i>Burnup</i> ($\frac{MWd}{kgHM}$)	<i>MTC</i> ($\frac{pcm}{K}$)	σ_{MTC} ($\frac{pcm}{K}$)
0,00	0	-40,39	±0,13	0,00	0	-23,14	±0,09
75,93	3	-44,52	±0,13	23,18	3	-23,86	±0,09
151,85	6	-48,75	±0,13	46,37	6	-25,17	±0,09
227,78	9	-51,75	±0,18	69,55	9	-26,18	±0,09
303,71	12	-52,96	±0,20	92,73	12	-27,35	±0,09
379,63	15	-53,71	±0,20	115,92	15	-28,43	±0,09
455,56	18	-53,06	±0,22	139,10	18	-29,43	±0,09
531,49	21	-51,37	±0,22	162,29	21	-30,38	±0,09
607,41	24	-49,02	±0,27	185,47	24	-31,26	±0,09
683,34	27	-44,83	±0,27	208,65	27	-32,29	±0,09
759,27	30	-42,05	±0,27	231,84	30	-33,10	±0,11
835,19	33	-37,28	±0,29	255,02	33	-33,93	±0,09
911,12	36	-30,65	±0,31	278,20	36	-34,40	±0,11
987,05	39	-23,68	±0,35	301,39	39	-35,12	±0,13
1062,97	42	-16,63	±0,35	324,57	42	-35,55	±0,13
1138,90	45	-8,83	±0,40	347,76	45	-35,73	±0,13
1214,83	48	0,29	±0,40	370,94	48	-36,02	±0,13
1290,75	51	7,97	±0,40	394,12	51	-35,80	±0,16
				417,31	54	-36,29	±0,16
				440,49	57	-35,89	±0,18
				463,67	60	-34,98	±0,18
				486,86	63	-35,23	±0,18
				510,04	66	-34,87	±0,18
				533,23	69	-33,27	±0,18
				556,41	72	-32,45	±0,18
				579,59	75	-30,88	±0,20
				602,78	78	-28,92	±0,20
				625,96	81	-27,23	±0,20
				649,14	84	-25,11	±0,24
				672,33	87	-21,51	±0,24
				695,51	90	-18,86	±0,24
				718,69	93	-14,48	±0,24
				741,88	96	-9,93	±0,27
				765,06	99	-4,33	±0,31
				788,25	102	1,92	±0,29
				811,43	105	8,64	±0,31
				834,61	108	17,20	±0,31
				857,80	111	27,16	±0,35
				880,98	114	38,39	±0,35
				904,16	117	51,19	±0,38
				927,35	120	66,47	±0,40

Table 6.2. MTC burnup calculation

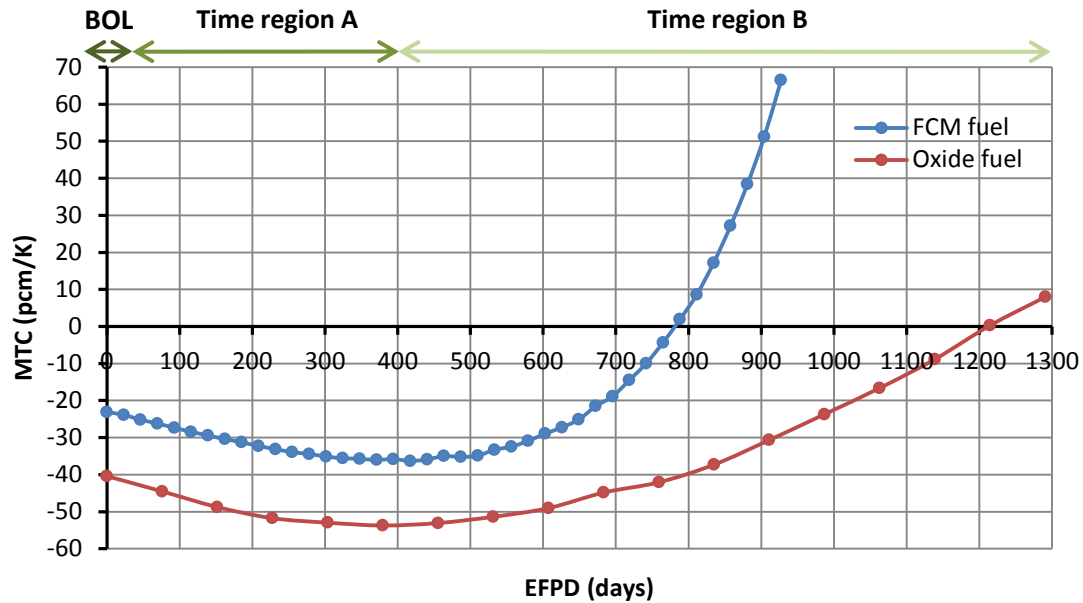


Figure 6.8. MTC burnup calculation

BOL. Regarding to MTC behavior at BOL, it can be observed that it is negative in both cases due to the lack of moderation produced by a decrease in water density, which moves neutron spectrum towards higher energies, hence increasing resonance absorption and decreasing k_{eff} value. However, FCM fuel achieves a less negative MTC value comparing with oxide fuel. This happens because the decrease in moderation is not that significant in the FCM fuel case due to the important amount of C in its composition, which acts as a neutron moderator. In this sense, FCM fuel configuration becomes less sensitive to changes in water temperature since the thermalization process is shared between the water and the C present inside the fuel rod itself.

Time region A. It corresponds to the first 400 days of cycle, where in both cases MTC becomes more negative. This is due to the depletion of ^{235}U , which increases the ^{238}U - ^{235}U ratio and thus enhances ^{238}U resonance absorption (see Figure 6.9). This leads to a larger decrease of the resonance escape probability (ρ) when water temperature increases, leading to a more negative MTC value (e.g. Figure 6.10 for oxide fuel).

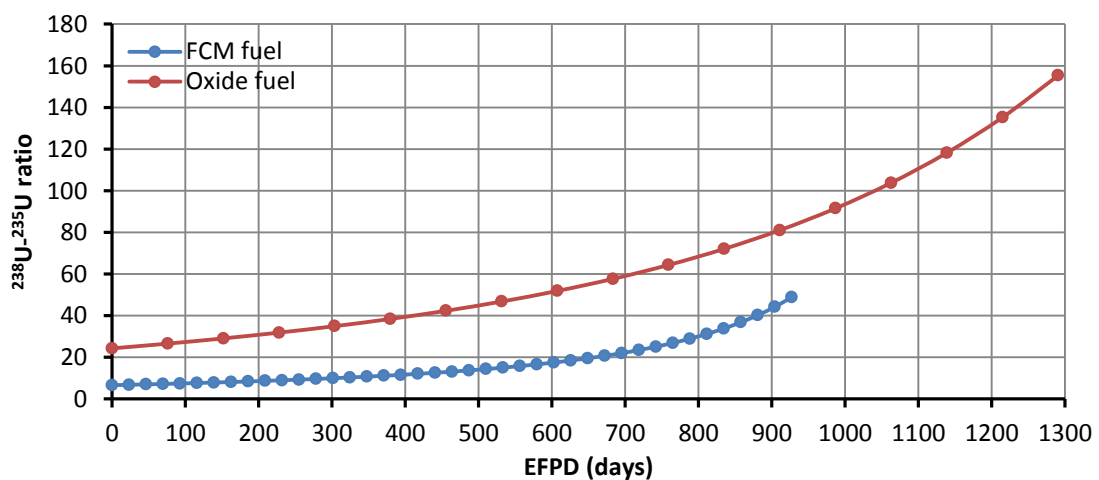


Figure 6.9. ^{238}U - ^{235}U ratio versus time

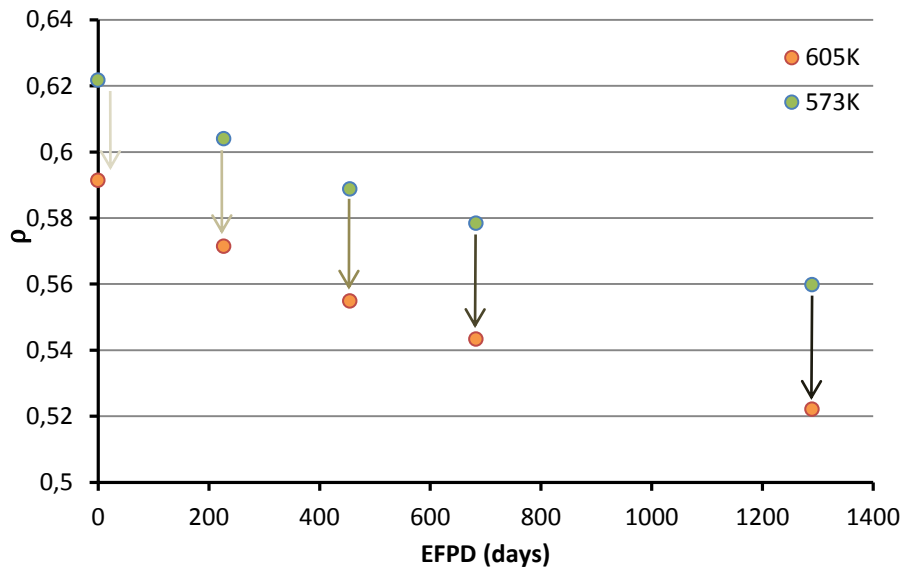


Figure 6.10. Decrease of the resonance escape probability (ρ) comparison

Time region B. Although ^{238}U - ^{235}U ratio effect leads to reduce MTC during along all fuel cycle, it can be noticed that in both cases MTC values become less negative and even positive as approaching to EOL. This is due to the accumulation of absorbent fission products such as ^{135}Xe or ^{149}Sm , which become more important for high burnup. As explained, an increase of the moderator temperature leads to a shift of the neutron spectrum to a higher energy, and the key point is that ^{135}Xe or ^{149}Sm absorption cross sections decrease for higher neutron energies (e.g. Figure 6.11 for ^{135}Xe and Figure 6.12 for ^{149}Sm). Hence, the presence of these fission products results in a positive contribution to MTC.

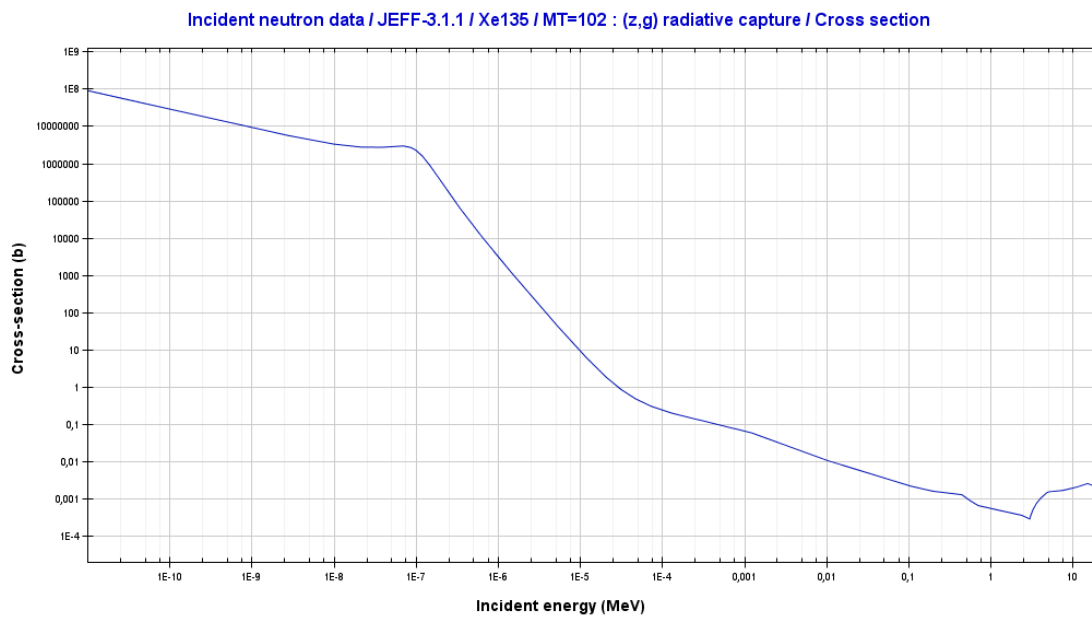


Figure 6.11. ^{135}Xe radiative capture cross section

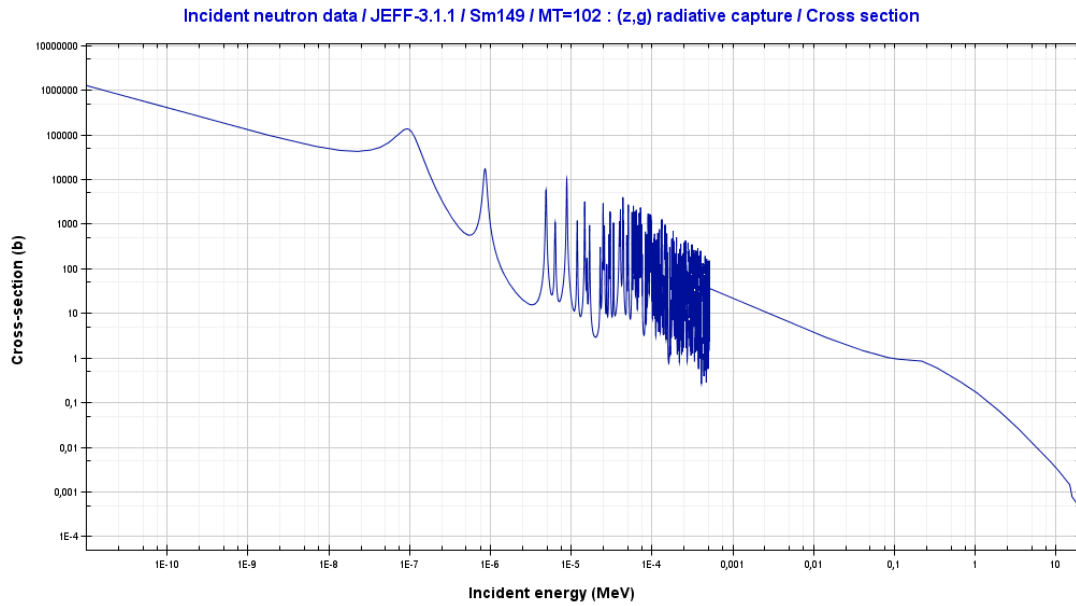


Figure 6.12. ^{149}Sm radiative capture cross section

However, a significant difference between both configurations is noticed since FCM fuel tends to a positive MTC value faster than the oxide fuel. This behavior could be explained by two reasons. In first place, it must be considered that the resonance absorptions are not only due to ^{238}U but also to ^{240}Pu , especially as approaching EOL. As shown in Figure 6.13, the quantity of ^{240}Pu becomes significantly higher by using oxide fuel since more ^{239}Pu is generated; therefore, the negative contribution of ^{240}Pu to MTC allows oxide fuel configuration to not achieve a positive feedback as fast as in FCM fuel.

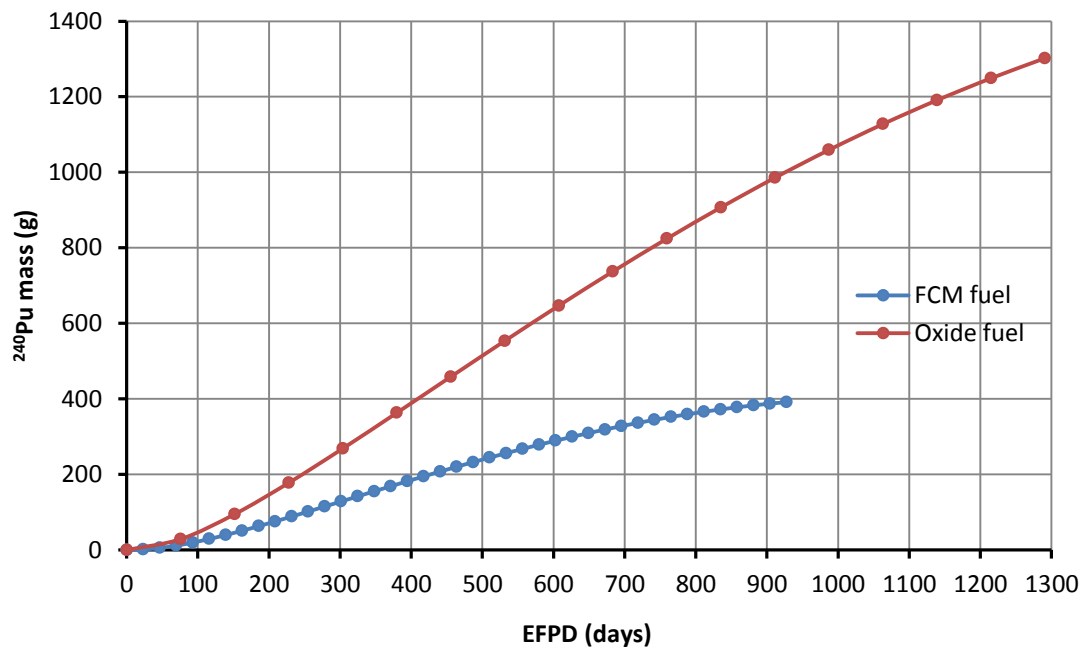


Figure 6.13. ^{240}Pu mass versus time

The second reason, and maybe the most important one, lies in a significant difference between both configurations regarding to already commented ^{135}Xe and ^{149}Sm absorption contributions. For high burnup values, a significant fraction of the fuel has been depleted compared to BOL, which increases the moderator to fuel ratio and thus makes ^{135}Xe and ^{149}Sm positive contribution to the MTC more important at EOL. However, this effect becomes much more important in the case of the FCM fuel because its configuration leads to a higher depletion rate, which significantly thermalizes the neutron spectrum along fuel cycle comparing with oxide fuel. Due to this scenario, fission products are depleted faster in the case of the FCM fuel because of increasing its absorption probability, leading to a higher positive contribution to the MTC. This behavior is exemplified in Figure 6.14, for the case of the ^{149}Sm isotope.

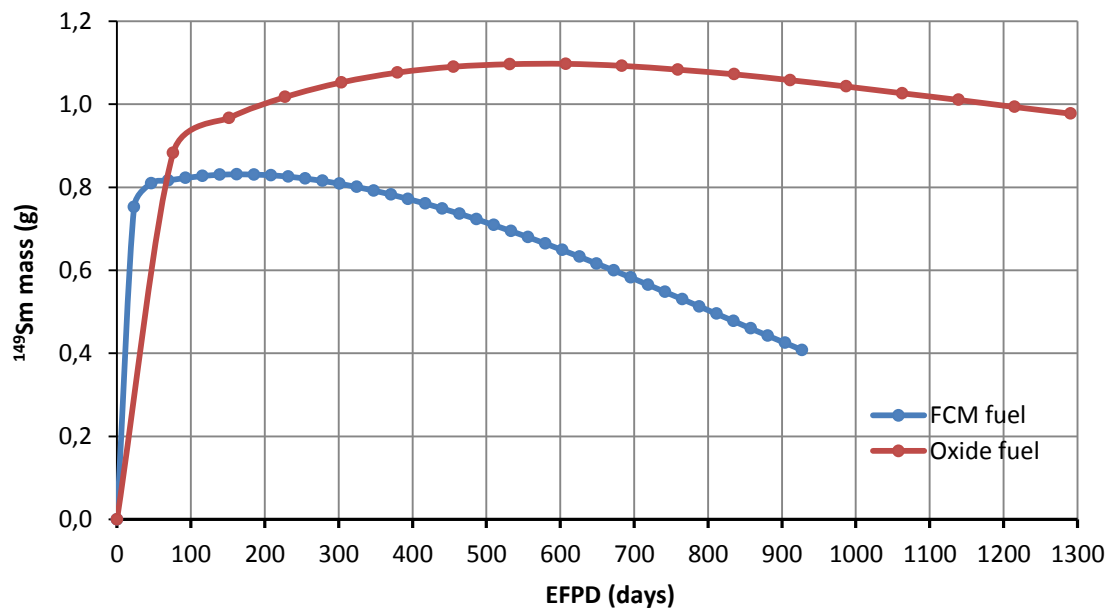


Figure 6.14. ^{149}Sm mass versus time

A very useful parameter in order to see these effects on the MTC curves is the thermal utilization factor (f), which represents the fraction of neutrons absorbed by the fuel over the total neutrons absorbed in the system. Figure 6.15 and Figure 6.16 show for each fuel configuration respectively how much does f change due to an increase of moderator temperature at different moments of the cycle.

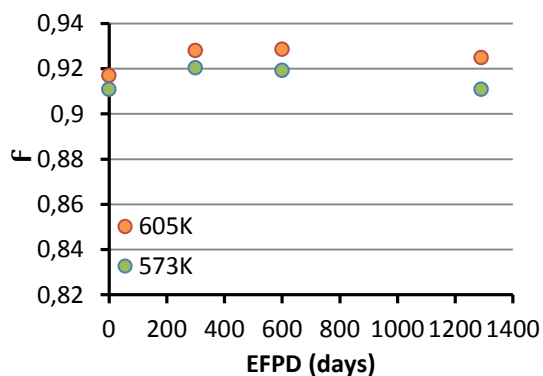


Figure 6.15. Oxide fuel f factor variation

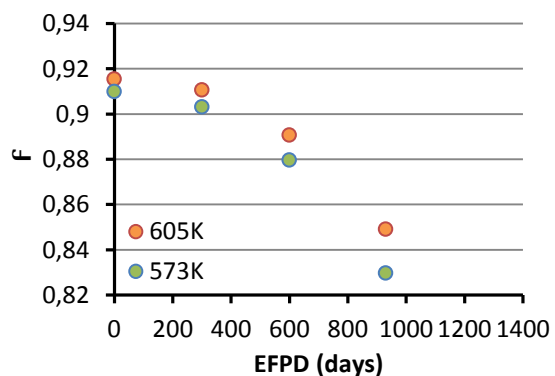


Figure 6.16. FCM fuel f factor variation

It is observed that β values, regardless of the moderator temperature, decrease faster for the FCM fuel than for the oxide fuel due to the higher depletion of ^{235}U . In addition, it can be noticed that for the first 400 days, β experiments the same change after a rise in water temperature in both fuel assemblies. Comparing simultaneously to Figure 6.8, this similarity corresponds to *Time region A*, where a similar behavior of the MTC is obtained from both fuel assemblies. However, from 400 days until EOL, β value increases more in the FCM fuel configuration than in oxide fuel, which is in accordance to the difference obtained between both MTC curves in *Time region B*.

This happens because ^{240}Pu produces the opposite effect to ^{135}Xe and ^{149}Sm in the oxide fuel, smoothing the β increase; whereas ^{135}Xe and ^{149}Sm contribution is enhanced for FCM fuel configuration, tending to increase significantly the β ratio when neutron spectrum moves towards higher energies, especially at EOL.

Finally, it must be commented that the other main influent factor in the MTC value apart from β is the already mentioned resonance scape probability (ρ), which always decreases as a consequence of the increasing ^{238}U resonance absorption after a water temperature rise as shown before. In this sense, it can be conclude that depending on the dominating effect ($\Delta\beta$ or $\nabla\rho$), MTC becomes more or less negative, or even positive.

6.2.2. MTC (1000ppm boron)

A variation of the MTC calculation has been done by dissolving 1000ppm of boron in the water, which represent the typically moderator boron concentration in PWR cycles at a nominal power [43].

The obtained results for *MTC* and $\sigma(MTC)$ are tabulated in Table 6.3, and a MTC comparison between 0ppm and 1000ppm boron concentrations is plotted in Figure 6.17:

17x17 Westinghouse FA				13x13 FCM FA			
<i>EFPD</i> (days)	<i>Burnup</i> ($\frac{MWd}{kgHM}$)	<i>MTC</i> ($\frac{pcm}{K}$)	σ_{MTC} ($\frac{pcm}{K}$)	<i>EFPD</i> (days)	<i>Burnup</i> ($\frac{MWd}{kgHM}$)	<i>MTC</i> ($\frac{pcm}{K}$)	σ_{MTC} ($\frac{pcm}{K}$)
0,00	0	-16,037	±0,13	0,00	0	-1,706	±0,09
75,93	3	-19,041	±0,18	23,18	3	-1,891	±0,09
151,85	6	-22,853	±0,18	46,37	6	-2,622	±0,09
227,78	9	-23,875	±0,20	69,55	9	-3,722	±0,09
303,71	12	-24,266	±0,22	92,73	12	-3,994	±0,09
379,63	15	-23,187	±0,27	115,92	15	-4,731	±0,13
455,56	18	-20,819	±0,27	139,10	18	-5,581	±0,13
531,49	21	-18,341	±0,27	162,29	21	-5,947	±0,13
607,41	24	-14,584	±0,29	185,47	24	-6,119	±0,13
683,34	27	-10,484	±0,31	208,65	27	-6,100	±0,13
759,27	30	-5,056	±0,31	231,84	30	-6,544	±0,18
835,19	33	0,909	±0,31	255,02	33	-6,238	±0,18
911,12	36	7,481	±0,40	278,20	36	-6,400	±0,18
987,05	39	14,569	±0,40	301,39	39	-5,953	±0,18
1062,97	42	22,222	±0,40	324,57	42	-6,091	±0,18
1138,90	45	31,203	±0,44	347,76	45	-5,516	±0,18
1214,83	48	39,241	±0,44	370,94	48	-4,409	±0,18
1290,75	51	48,056	±0,49	394,12	51	-4,122	±0,18
				417,31	54	-2,816	±0,18
				440,49	57	-2,078	±0,18
				463,67	60	-0,334	±0,18
				486,86	63	1,663	±0,22
				510,04	66	3,713	±0,22
				533,23	69	5,844	±0,24
				556,41	72	8,719	±0,24
				579,59	75	10,784	±0,24
				602,78	78	14,237	±0,27
				625,96	81	17,534	±0,31
				649,14	84	21,109	±0,31
				672,33	87	26,184	±0,31
				695,51	90	32,184	±0,31
				718,69	93	37,866	±0,33
				741,88	96	44,200	±0,35
				765,06	99	51,816	±0,35
				788,25	102	60,438	±0,38
				811,43	105	69,312	±0,42
				834,61	108	79,878	±0,40
				857,80	111	91,363	±0,46

Table 6.3. MTC burnup calculation for 1000ppm boron concentration

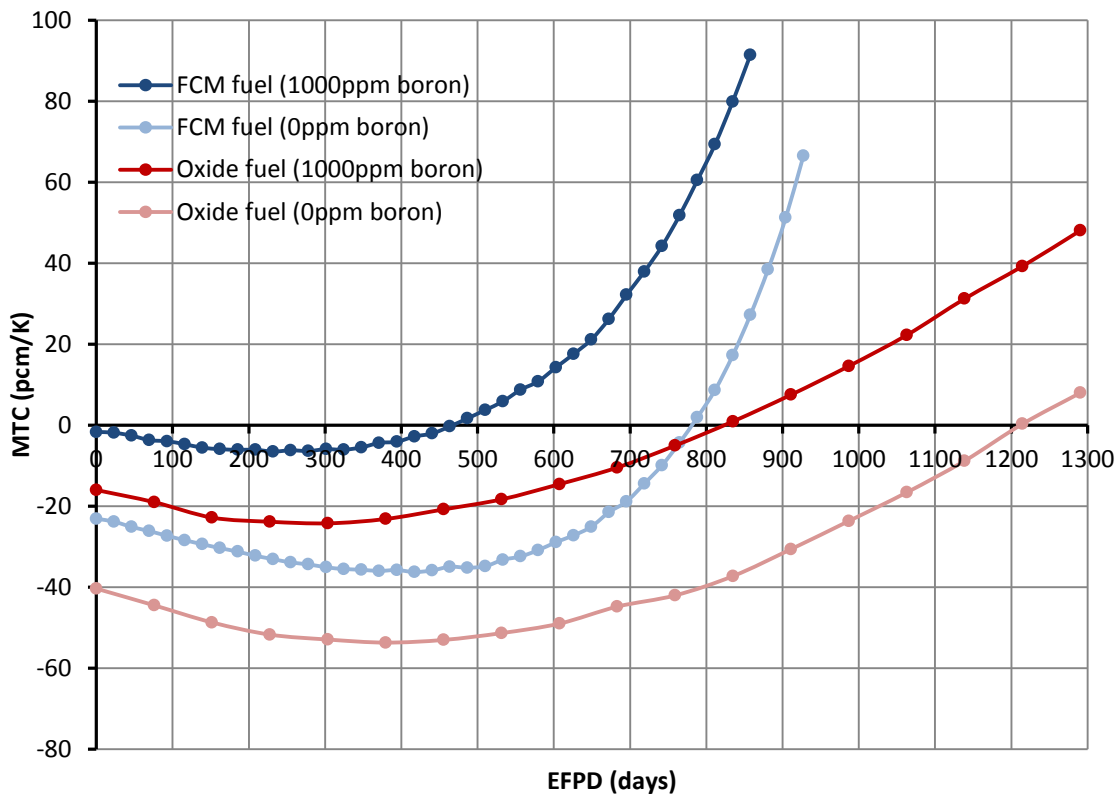
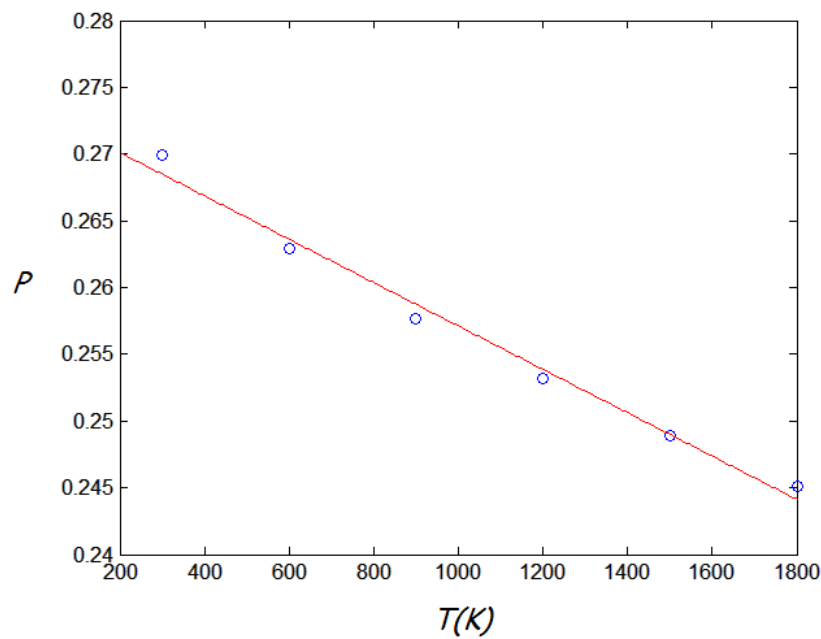


Figure 6.17. MTC comparison for 0ppm and 1000ppm boron concentration

It can be observed for both fuel assemblies that, although MTC performs the same tendency regardless of their boron concentration, the curves are located in a more positive region of the MTC. Since boron is dissolved in the water, a temperature increase also reduces the boron density leading to reduce its absorption contribution. The high absorption cross section of the boron makes this effect very significant, leading to obtain important differences in the MTC depending on its level of concentration. Special careful must be taken in case of using FCM fuel, which has a very small negative MTC at BOL and achieves a positive feedback at mid-cycle.

6.2.3. FTC

Fuel Temperature Coefficient (FTC) has been calculated similarly to MTC, but in this case by running various simulations changing only the fuel temperature, i.e. 300K, 600K, 900K, 1200K, 1500K and 1800K, corresponding to the temperatures *JEFF-3.1.1.xsdata* cross section library is divided into. After $k_{\text{eff}} \rightarrow \rho$ translation, a linear regression has been fitted to each burnup step six-point vector, with the aim of calculating how much does the reactivity change with the fuel temperature. Although reactivity seems to have a slightly curvilinear relationship with fuel temperature, the linear fitting has been considered a good approach since not working with the very extreme temperatures (see Figure 6.18).



Note: The uncertainties of the values are less than the point diameter

Figure 6.18. FTC linear fitting example

After developing the fitting process as for MTC, the obtained results are gathered in Table 6.4. and plotted in Figure 6.19, which shows FTC and σ (FTC) values for both fuel assemblies, again divided into three time regions.

17x17 Westinghouse FA				13x13 FCM FA			
<i>EFPD</i> (days)	<i>Burnup</i> ($\frac{MWd}{kgHM}$)	<i>FTC</i> ($\frac{pcm}{K}$)	σ_{FTC} ($\frac{pcm}{K}$)	<i>EFPD</i> (days)	<i>Burnup</i> ($\frac{MWd}{kgHM}$)	<i>FTC</i> ($\frac{pcm}{K}$)	σ_{FTC} ($\frac{pcm}{K}$)
0,00	0	-1,62	$\pm 0,0024$	0,00	0	-1,48	$\pm 0,0016$
75,93	3	-1,72	$\pm 0,0024$	23,18	3	-1,52	$\pm 0,0016$
151,85	6	-1,81	$\pm 0,0024$	46,37	6	-1,56	$\pm 0,0016$
227,78	9	-1,90	$\pm 0,0028$	69,55	9	-1,58	$\pm 0,0016$
303,71	12	-1,93	$\pm 0,0033$	92,73	12	-1,63	$\pm 0,0016$
379,63	15	-1,97	$\pm 0,0036$	115,92	15	-1,66	$\pm 0,0016$
455,56	18	-1,92	$\pm 0,0037$	139,10	18	-1,70	$\pm 0,0016$
531,49	21	-1,82	$\pm 0,0040$	162,29	21	-1,74	$\pm 0,0016$
607,41	24	-1,72	$\pm 0,0042$	185,47	24	-1,82	$\pm 0,0018$
683,34	27	-1,56	$\pm 0,0045$	208,65	27	-1,81	$\pm 0,0016$
759,27	30	-1,33	$\pm 0,0048$	231,84	30	-1,89	$\pm 0,0018$
835,19	33	-1,12	$\pm 0,0052$	255,02	33	-1,92	$\pm 0,0019$
911,12	36	-0,84	$\pm 0,0055$	278,20	36	-1,93	$\pm 0,0020$
987,05	39	-0,53	$\pm 0,0061$	301,39	39	-1,97	$\pm 0,0020$
1062,97	42	-0,18	$\pm 0,0061$	324,57	42	-1,92	$\pm 0,0024$
1138,90	45	0,18	$\pm 0,0064$	347,76	45	-1,93	$\pm 0,0024$
1214,83	48	0,52	$\pm 0,0072$	370,94	48	-1,96	$\pm 0,0026$
1290,75	51	0,89	$\pm 0,0071$	394,12	51	-1,95	$\pm 0,0028$
				417,31	54	-1,94	$\pm 0,0028$
				440,49	57	-1,93	$\pm 0,0029$
				463,67	60	-1,85	$\pm 0,0032$
				486,86	63	-1,81	$\pm 0,0032$
				510,04	66	-1,77	$\pm 0,0032$
				533,23	69	-1,69	$\pm 0,0032$
				556,41	72	-1,61	$\pm 0,0032$
				579,59	75	-1,52	$\pm 0,0032$
				602,78	78	-1,41	$\pm 0,0033$
				625,96	81	-1,28	$\pm 0,0036$
				649,14	84	-1,12	$\pm 0,0040$
				672,33	87	-0,94	$\pm 0,0044$
				695,51	90	-0,72	$\pm 0,0040$
				718,69	93	-0,50	$\pm 0,0044$
				741,88	96	-0,21	$\pm 0,0048$
				765,06	99	0,11	$\pm 0,0056$
				788,25	102	0,50	$\pm 0,0052$
				811,43	105	0,92	$\pm 0,0056$
				834,61	108	1,43	$\pm 0,0053$
				857,80	111	2,00	$\pm 0,0061$
				880,98	114	2,59	$\pm 0,0064$
				904,16	117	3,29	$\pm 0,0068$
				927,35	120	4,11	$\pm 0,0069$

Table 6.4. FTC burnup calculation

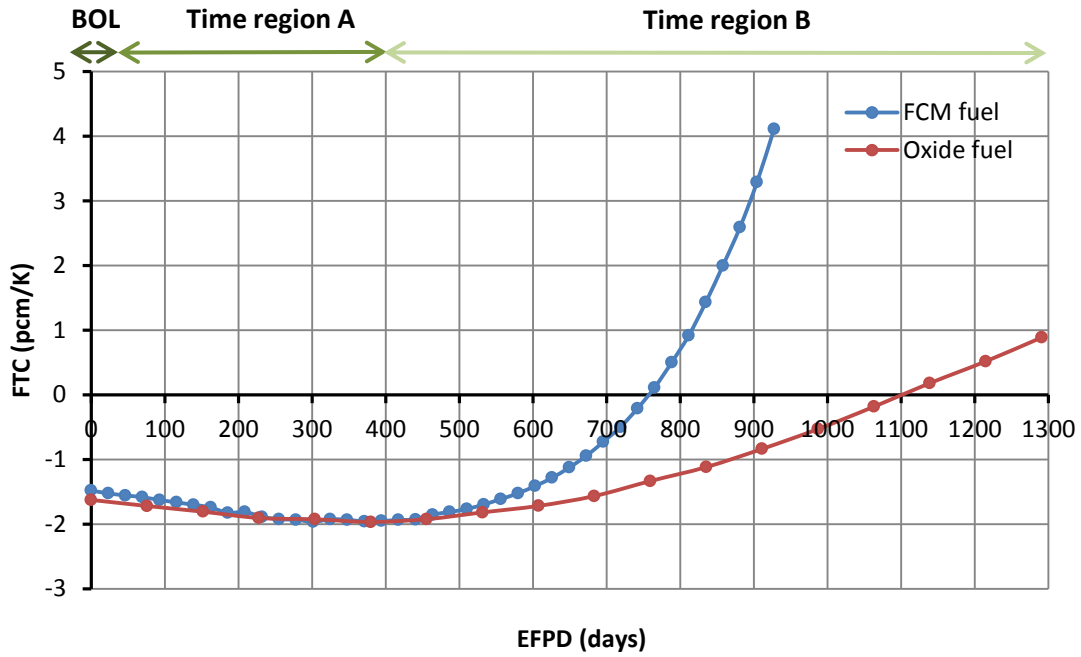


Figure 6.19. FTC comparison

BOL: It can be noticed that FTC presents negative values for both configurations, similarly to MTC behavior, because the fact of increasing the fuel temperature also shifts the Maxwell neutron spectrum to higher energies. This is due to the increase of the resonance capture probability by a widening in the ^{238}U absorption resonances (Doppler Effect), which leads to decrease the resonance scape probability (ρ), reducing the number of thermalized neutrons and thus hardening neutron spectrum [44].

On the other hand, it can be observed that at BOL the behavior of both fuel assemblies is much more similar for the FTC than for the MTC. At first, FCM fuel should present a more significant less negative FTC value compared to the oxide fuel because its lower total initial amount of ^{238}U reduces the total negative contribution of the Doppler Effect. However, this effect is counteracted by the low *slowing down power* (SDP) of the C present in FCM fuel, which contributes to make FTC more negative. The SDP expresses the average loss in the logarithm of the energy per unit distance of travel in the moderator:

$$SDP [cm^{-1}] = \xi \cdot \Sigma_s \quad (6.7)$$

Where,

$$\xi = \ln \frac{E}{E'} \quad (6.8)$$

- ξ is the average logarithmic energy decrement per collision. E and E' are the energies of the neutron before and after the collision respectively.
- Σ_s is the *scattering macroscopic cross-section* of the moderator (cm^{-1}).

As explained before, the moderation process by the use of FCM fuel is shared between the light water and the C present in the non-reactive part of the fuel rod, whereas for oxide fuel all the thermalization is carried out by the light water. In order to understand why this difference is that important for the FTC, Table 6.5 shows the difference between C and H₂O moderation effectiveness [45].

Moderator	ξ	Collisions to thermalize	SDP (cm ⁻¹)
H ₂ O	0,920	20	1,530
Carbon (graphite)	0,158	115	0,064

Table 6.5. SDP for H₂O and carbon moderators

As observed, Carbon does not reduce that much energy per collision as H₂O, so more collisions are needed to thermalize the fast neutron. This effect is extremely influent in the FTC, because the low SDP value of C makes the fast neutron scatter into a larger number of energetic levels, increasing significantly the resonance absorption probability in presence of Doppler Effect and thus producing a negative contribution to the FTC value.

Time region A: FTC becomes more negative in both cases due to the depletion of ²³⁵U, which increases the ²³⁸U-²³⁵U ratio as explained before for the MTC. In addition, this factor makes more important the effect of the low SDP of C in the FCM fuel configuration, even leading to achieve a similar FTC value as for oxide fuel.

Time region B: Approaching EOL, ²⁴⁰Pu and specially ¹³⁵Xe and ¹⁴⁹Sm contributions are dominants in front of any other effect, leading to obtain a similar behavior between FTC and MTC in this part of the cycle.

As a general comment, it must be noticed that absolute values of FTC are significantly lower than MTC values due to the stronger lack of thermalization after a temperature rise in the water, which affects directly the moderator element. However, this does not reduce FTC importance in front of MTC, because FTC is the first mechanism to act after a sudden increase in the power, so a negative value is essential regarding to safety aspects.

6.2.4. Void worth

Void worth coefficient (CVR) is calculated by the difference between the obtained k_{eff} from a standard system configuration with coolant and from the completely voided system. Hence, $\sigma(CVR)$ is directly calculated as follows:

$$\begin{aligned}\sigma(CVR) &= \sqrt{\left(\frac{\partial CVR}{\partial k_{eff (without)}} \cdot \sigma(k_{eff (without)})\right)^2 + \left(\frac{\partial CVR}{\partial k_{eff (with)}} \cdot \sigma(k_{eff (with)})\right)^2} = \\ &= \sqrt{\left(\sigma(k_{eff (without)})\right)^2 + \left(\sigma(k_{eff (with)})\right)^2}\end{aligned}$$

Where,

$$CVR [pcm] = (k_{eff (without coolant)} - k_{eff (with coolant)}) \cdot 10^5 \quad (6.9)$$

The CVR calculation is very interesting because it is a useful parameter to describe the change in the reactivity of a reactor after a LOCA, when water is removed from the core. However, to perform a good CVR analysis it is absolutely necessary to take into account the neutron leakage factor, which becomes essential when there is no moderator in the core. Therefore, an adequate scenario to analyze CVR is to accurately describe the whole core and introduce “black” boundary conditions³¹ around it, in order to perform a more realistic analysis by taking into account the neutron leakage.

However, this thesis is focused on benchmarking FCM fuel and oxide fuel configurations at a fuel assembly level, in which does not make sense to introduce black boundary conditions because almost all the neutrons would be rapidly killed by the boundary under absence of moderator conditions. Hence, the reflective boundary condition (no leakage) has been maintained for this analysis, so it must be noticed that the results lose their veracity as absolute values, and must be just taken in a way of comparing the behavior of both fuel assemblies. The obtained results for CVR and $\sigma(CVR)$ are gathered in Table 6.6 and plotted in Figure 6.20.

³¹ It is one of the boundary conditions that can be used in SERPENT. When the neutron encounters the “black” boundary it is “killed”; i.e. the chain is terminated for the neutron [33].

17x17 Westinghouse FA				13x13 FCM FA			
<i>EFPD</i> (days)	<i>Burnup</i> ($\frac{MWd}{kgHM}$)	<i>CVR</i> (pcm)	σ_{CVR} (pcm)	<i>EFPD</i> (days)	<i>Burnup</i> ($\frac{MWd}{kgHM}$)	<i>CVR</i> (pcm)	σ_{CVR} (pcm)
0,00	0	-74622	±10	0,00	0	-64858	±8
75,93	3	-61897	±9	23,18	3	-58492	±8
151,85	6	-54418	±9	46,37	6	-57678	±8
227,78	9	-47754	±9	69,55	9	-56923	±8
303,71	12	-41801	±9	92,73	12	-56142	±8
379,63	15	-36378	±9	115,92	15	-55335	±8
455,56	18	-31469	±10	139,10	18	-54494	±8
531,49	21	-26880	±9	162,29	21	-53644	±8
607,41	24	-22610	±10	185,47	24	-52789	±8
683,34	27	-18588	±9	208,65	27	-51941	±8
759,27	30	-14818	±10	231,84	30	-51078	±8
835,19	33	-11246	±9	255,02	33	-50219	±8
911,12	36	-7824	±9	278,20	36	-49325	±8
987,05	39	-4620	±10	301,39	39	-48452	±8
1062,97	42	-1559	±10	324,57	42	-47536	±9
1138,90	45	1313	±11	347,76	45	-46630	±8
1214,83	48	4040	±10	370,94	48	-45681	±9
1290,75	51	6575	±10	394,12	51	-44742	±9
				417,31	54	-43754	±9
				440,49	57	-42761	±9
				463,67	60	-41705	±9
				486,86	63	-40654	±9
				510,04	66	-39585	±9
				533,23	69	-38439	±9
				556,41	72	-37265	±9
				579,59	75	-36074	±9
				602,78	78	-34814	±9
				625,96	81	-33528	±9
				649,14	84	-32193	±9
				672,33	87	-30791	±9
				695,51	90	-29341	±9
				718,69	93	-27822	±9
				741,88	96	-26265	±9
				765,06	99	-24644	±9
				788,25	102	-22947	±9
				811,43	105	-21228	±9
				834,61	108	-19426	±9
				857,80	111	-17546	±9
				880,98	114	-15624	±10
				904,16	117	-13632	±9
				927,35	120	-11604	±9

Table 6.6. CVR burnup calculation

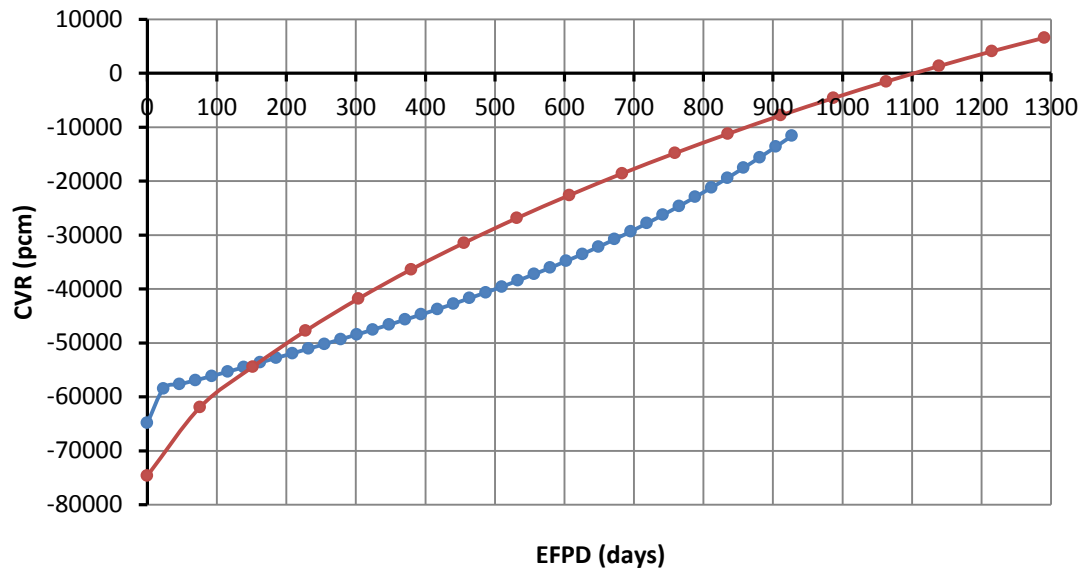


Figure 6.20. CVR comparison

At BOL, it can be observed that CVR is less negative for the FCM fuel configuration. This happens because when the core is completely voided, carbon of the FCM fuel still maintains its contribution to the moderation process whereas for oxide fuel all the moderator is removed. This leads to a significant difference between neutron spectrums in both fuel assemblies, in such a way that FCM fuel is still capable to produce thermal fissions whereas oxide fuel loses almost all its probability.

As time passes, CVR becomes less negative in both cases, but performing a different behavior as shown. For better understanding, it is very useful to plot k_{eff} values for both configurations before and after losing the water inside the core (see Figure 6.21).

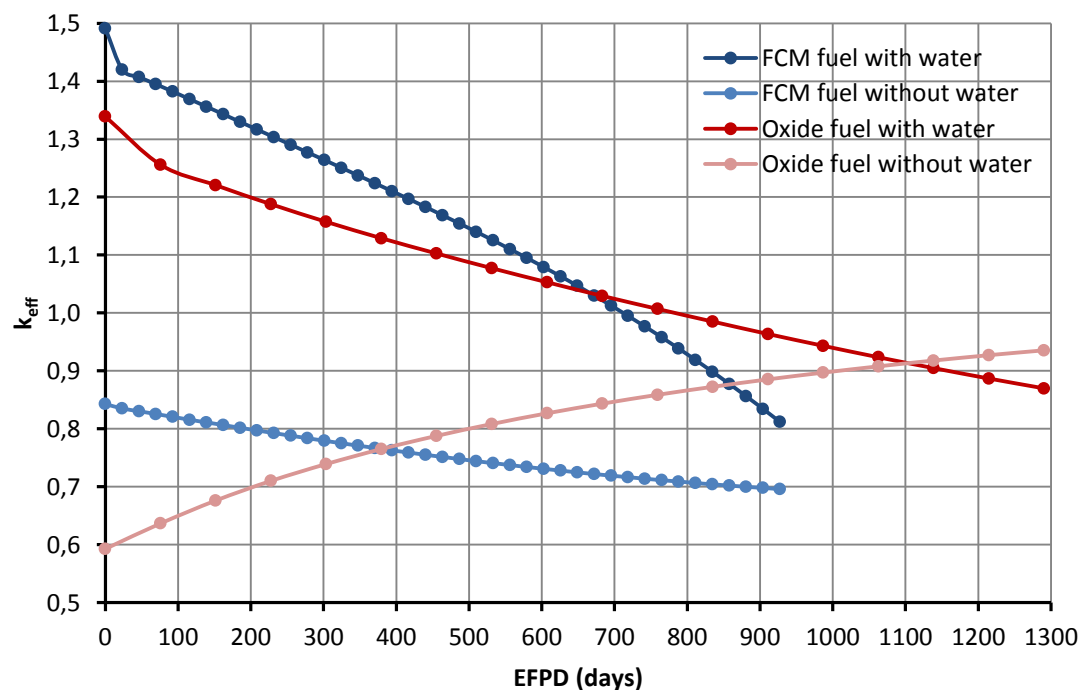


Figure 6.21. Burnup calculation for k_{eff} with and without water in the core

As shown, the reactivity curves in presence of water are the same as obtained at the beginning of the chapter. It must be remembered that the higher stiffness of the FCM fuel reactivity curve has been explained by its higher depletion of ^{235}U isotope, which leads to decrease k_{eff} as time passes. However, the CRV behavior of both fuel assemblies is also a result of the difference between them regarding to their k_{eff} values without water in the core, and it can be observed that FCM fuel curve decreases with burnup whereas oxide fuel curve increases significantly.

In the case of the oxide fuel this behavior is due to the fission of TRU isotopes that have been accumulated during the cycle. As explained, neutron spectrum extremely changes becoming much harder in the case of the oxide fuel, which leads to optimize the fission probability of TRU (see Figure 6.22).

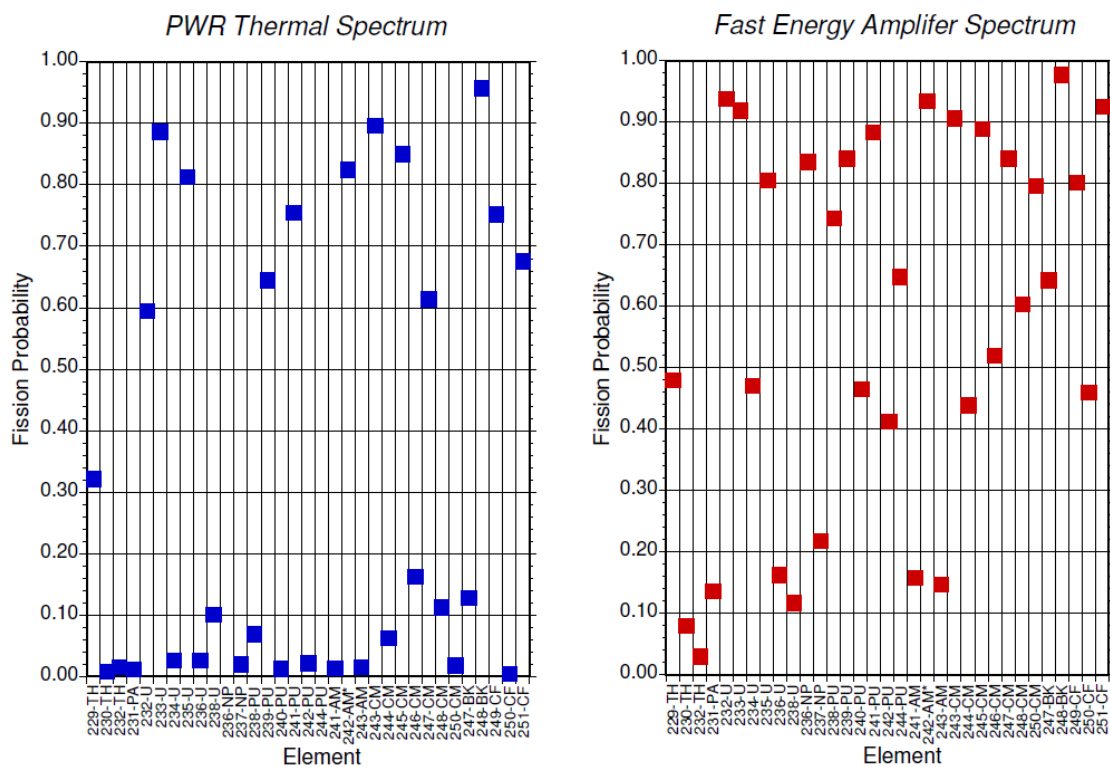


Figure 6.22. Fission probability of TRU in a thermal and fast neutron spectrum³²

As shown, the average fission probability of TRU increases significantly in a fast spectrum. This effect combined with the progressive depletion of ^{235}U makes oxide fuel CVR curve less negative as approaching EOL. This TRU fission effect has been exemplified for the case of the ^{242}Pu isotope. As seen before in Figure 6.22, ^{242}Pu isotope changes its fission probability from almost zero to about 50%, due to its higher fission cross section for high energies (see Figure 6.23).

³² Ernst Radermacher. *Contribution of the Energy Amplifier to New Applications*. CERN, Geneva, Switzerland.

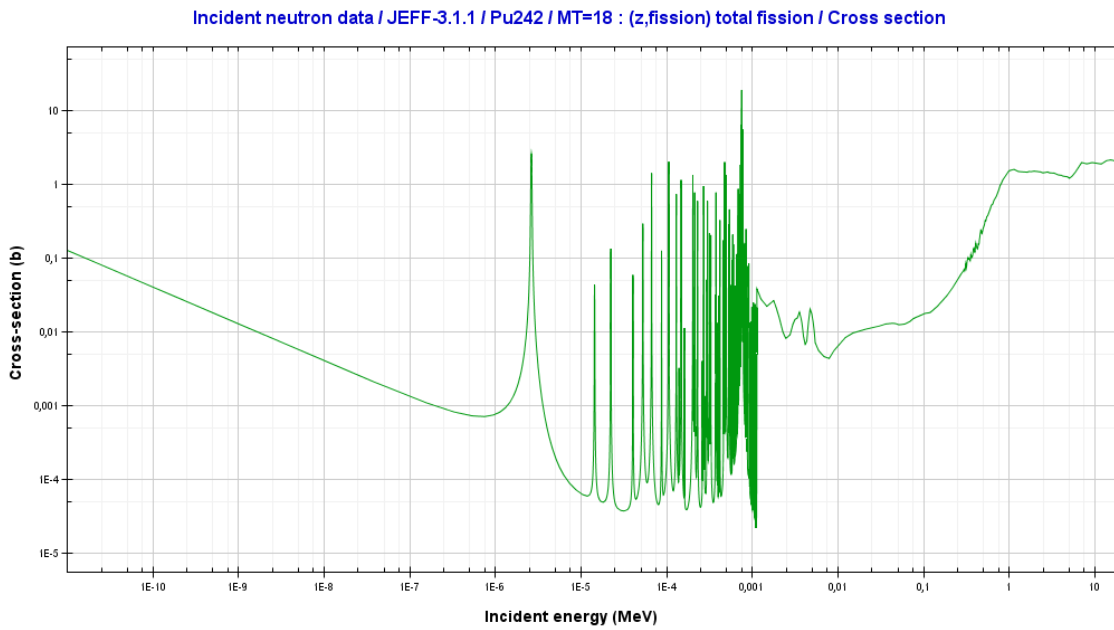


Figure 6.23. ^{242}Pu fission cross section

In addition, Figure 6.24 plots the mass of ^{242}Pu calculated along burnup for each fuel assembly configuration and in both cases: with water and without water in the core. It can be noticed that the difference between ^{242}Pu masses is much more significant in the case of the oxide fuel, in which a larger amount of ^{242}Pu is fissioned because of the fast neutron spectrum existent after a LOCA.

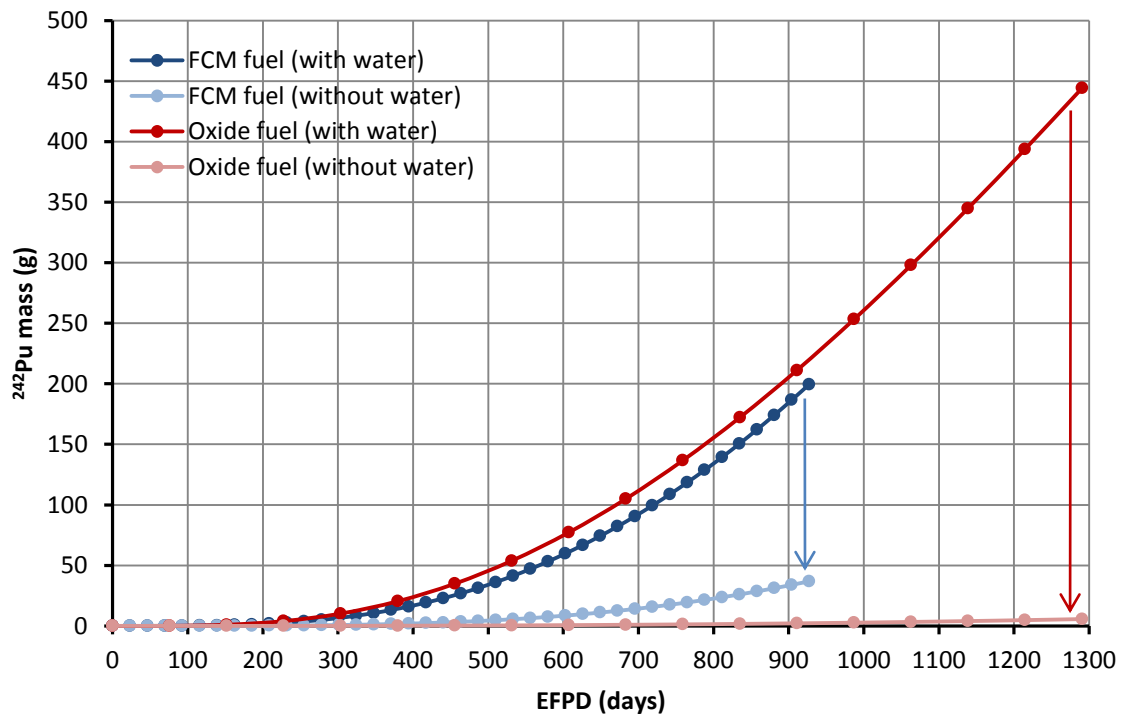


Figure 6.24. ^{242}Pu mass with and without water in the core

Finally, in the case of the FCM fuel, the TRU presence is very reduced comparing to oxide fuel due to its lower heavy metal mass. Moreover, the neutron spectrum does not become that much fast as commented, so the k_{eff} response without water in the system tends to experiment a similar behavior as for the case with water, reducing its value along burnup due to the ^{235}U depletion.

Chapter 7

Conclusions

This section is focused on exposing the conclusions obtained from the three stages this work is structured in, especially after the results analyses. In the end of the section, some of the possible proposals to continue with this project will be exposed.

The model designing has showed that the use of FMC fuel increases enrichment requirements due to the geometry of the TRISO particle and the surrounding SiC matrix, and that it is hardly dependent on the packing fraction value and the size of the TRISO particles. Regarding to the simulation, SERPENT has proved to be a very useful tool to model the geometry of a fuel assembly, as well as prepared to model TRISO particles inside the desired matrix. By the comparison between two of the methodologies of defining TRISO particles, it has been noticed that the regular 3D array is a very useful way of modeling them, producing good results without extremely increasing time calculation. Various analyses showed that the number of neutrons and cycles used changes significantly the obtained results, as well as the definition of the burnup calculation, which is especially problematic because of needing a very short step-length calculation to not produce very significant errors in the last steps.

In relation to the reactivity curves study, the burnup simulations has shown that FCM fuel increases significantly the reactivity introduced by the fuel at BOL, basically due to its higher enrichment, the SiC neutron transparency and the extra thermalization factor of the carbon. However, the use of a lower amount of total heavy metal mass compared to oxide fuel decreases the breeding of ^{239}Pu and ^{241}Pu isotopes, leading to deplete faster the ^{235}U isotope although producing the same total amount of energy. This characteristic is disadvantageous regarding to the neutron economy because of decreasing significantly the cycle length, but is advantageous in a non-proliferation point of view and in reducing the final amount of nuclear waste.

Regarding to MTC, the use of FCM fuel gives a less negative feedback during the first half of cycle compared to oxide fuel due to the presence of an important amount of carbon in its composition, which counteracts the loss of moderation capability after an increase in water temperature. However, it has been observed that MTC is still significantly negative and as

stable as the oxide fuel. The difference between both configurations appears at EOL, when FCM fuel MTC curve turns to dangerous positive feedbacks because of a higher absorption impact of fission products as ^{149}Sm and ^{135}Xe and a lack of ^{240}Pu resonance absorptions. Last but not least, the presence of boron in the water represents a very significant positive contribution to the MTC, which make the use of FCM fuel much more delicate.

In the case of the FTC, the low slowing down power of the Carbon makes from it an especial inefficient moderator in the presence of Doppler Effect, tending to resemble FCM fuel behavior to oxide fuel. However, approaching EOL the fission products contribution becomes dominant, leading to make FTC rapidly positive in the case of FCM fuel.

Finally, and oppositely to MTC and FTC, CVR analysis showed a safer behavior for the FCM fuel in case of a LOCA, especially at EOL. Its lower accumulation of TRU and the presence of Carbon in its composition maintains neutron spectrum in relatively thermal energies, smoothing the abrupt change in the neutron spectrum.

In general terms, after the neutronics analysis it is concluded that FCM fuel tends to give a more positive feedback compared to oxide fuel, especially at EOL. However, the use of FCM fuel is extremely advantageous in terms of thermal conductivity, cladding behavior and radiation containment, and even in non-proliferation and nuclear waste aspects as obtained, which makes absolutely recommendable further research in the use of FCM fuel in LWRs.

For future studies, it could be interesting to continue this work in mainly three different ways. *In first place*, it would be interesting to perform the same neutronics analysis but for higher packing fraction values. In this thesis a 40% PF value has been used, but last studies are focused on increasing UN TRISO particles packing fraction, even talking about values around 60%. It would be interesting to see whether by decreasing FCM fuel enrichment requirements and enhancing its self-shielding, safety parameters look more alike in both configurations. *Secondly*, taking into account that SERPENT accumulates a significant error for the last steps of the burnup calculation and that a detailed comparison between both configurations is especially important at EOL, it would be interesting to run a whole reactor steady state calculation at EOL, by using a more realistic spent fuel configuration in the core. *Lastly*, it would be a significant improvement to simulate a better designed FCM fuel configuration, by obtaining more exhaustive information regarding to thermo-hydraulic and power density compatibility studies.

Bibliography

- [1] British Petroleum (BP). *BP Statistical Review of World Energy June 2012*.
- [2] Consejo de Seguridad Nuclear (CSN). *Centrales Nucleares*.
Website: http://www.csn.es/index.php?option=com_content&view=article&id=132&Itemid=137%E2%8C%A9=es
- [3] World Nuclear Association. *The Nuclear Fuel Cycle*. June 2011.
Website: <http://www.world-nuclear.org/info/inf03.html>
- [4] Canadian Nuclear Safety Commission. *Safety Analysis for Nuclear Power Plants*. Regulatory document RD-310, February 2008.
- [5] Nuclear Science and Engineering at MIT. *Explanation of Nuclear Reactor Decay Heat*. Department of Nuclear Science and Engineering at MIT, March 2011
- [6] University of Illinois at Urbana-Champaign. *Accidente por apagón en Fukushima*.
Website: [https://netfiles.uiuc.edu/mragheb/www/Accidente por apagon en Fukushima.pdf](https://netfiles.uiuc.edu/mragheb/www/Accidente%20por%20apagon%20en%20Fukushima.pdf)
- [7] Manuel González Cuesta. *Aprovechamiento del Análisis Probabilístico de Seguridad en centrales nucleares*. Academia de Ingeniería de México, May 2010.
- [8] John Downer, *When Failure is an Option: Redundancy, reliability and regulation in complex technical systems*. Centre for Analysis of Risk and Regulation (CARR), 2009.
- [9] World Nuclear Association. *Fukushima accident 2011*. April 2012.
- [10] US Nuclear. *US-R100 Ultra Safe Reactor Concept*.
- [11] L.L. Snead, K.A. Terrani, F.Venneri, Y. Kim, J.E. Tulenko, C.W. Forsberg, P.F. Peterson, E.J. Lahoda. *Fully Ceramic Microencapsulated fuels: A Transformational Technology for Present and Next Generation Reactors – Properties and Fabrication of FCM Fuel*.
- [12] US Nuclear, *San Diego presentation*.
- [13] Michael A. Stawicki. *Benchmarking of the MIT High Temperature Gas-Cooled Reactor TRISO-Coated Particle Fuel Performance Model*, Massachusetts Institute of Technology, May 2006.
- [14] Dr. Eddie López Honorato. *The High Temperature Reactor and the TRISO coated fuel particle (Part1)*. November 2011.
- [15] F. Venneri, Chang-Keun Jo, J. Chang. *A Study on Feasibility of Using FCM fuel on a Light Water Reactor*, Ultra Safe Nuclear Corporation, LWRFCMPaper_v2.
- [16] Tatjana Jevremovic. *Nuclear Principles in Engineering, Second Edition*. Purdue University, 2009.
- [17] Jan Leen Kloosterman, *Nuclear Reactors*. Delft University of Technology, 2012.
Website: www.janleenkloosterman.nl/reactors.php

- [18] World Nuclear Association. *Chernobyl Accident 1986*. April 2012.
Website: <http://www.world-nuclear.org/info/chernobyl/inf07.html>
- [19] Herbert L. Anderson. *Metropolis, Monte Carlo, and the MANIAC*. Los Alamos Science Fall, LAUR-86-2600, 1986.
- [20] M. Hanuš. *Numerical Modeling of Neutron Transport*. Master's Thesis, University of West Bohemia, 2009.
- [21] Stephen A. Dupree and Stanley K. Fraley. *A Monte Carlo Premier. A Practical Approach to Radiation Transport*. Sandia National Laboratories Albuquerque, New Mexico, 2002.
- [22] Forrest B. Brown. *Fundamentals of Monte Carlo Particle Transport*. Los Alamos National Laboratory, LA-UR-05-4983, 2005.
- [23] Penn State University. *NUC E 521 Neutron Transport Theory*.
http://www.engr.psu.edu/cde/courses/nuce521/nuce521_chapter1_reading.pdf
- [24] U.S. Department of Energy. *Overview of neutron transport codes*, 2009.
- [25] D. S. Lucas, H. D. Gougar, T. Wareing, G. Failla, J. McGhee, D. A. Barnett, I. Davis, Douglas Lucas. *Comparison Of The 3-D Deterministic Neutron Transport Code Attila To Measure Data, MCNP And MCNPX For The Advanced Test Reactor*. Idaho National Laboratory, 2005.
- [26] A. D. Oliveira and C. Oliveira. *Comparison of deterministic and Monte Carlo methods in shielding design*. Oxford University Press, 2005.
- [27] Mahmoud Z Youssef. *ATTILA Deterministic Code (Status and plans for validation)*. University of California, Los Angeles, 2006.
- [28] B. L. Kirk. *Overview of Monte Carlo Neutron Transport Codes*. Radiation Safety Information Computational Center (RSICC).
- [29] Dermott E. Cullen, Christopher J. Clouse, Richard Procassini and Robert C. Little. *Static and Dynamic Criticality: Are They Different?* Lawrence Livermore National Laboratory. U.S. Department of Energy, November 22, 2003.
- [30] Jaakko Leppänen. *Development of a New Monte Carlo Reactor Physics Code*. PhD thesis, Helsinki University of Technology, 2007.
- [31] Emily R. Wolters. *Hybrid Monte Carlo – Deterministic Neutron Transport Methods Using Nonlinear Functionals*. The University of Michigan, 2011.
- [32] Joint Research center, European Commission. *Introduction to The Monte Carlo Method*. EMC_Cesme_2008_short, 2008.
- [33] Jaakko Leppänen. *PSG2 / Serpent – a Continuous-energy Monte Carlo Reactor Physics Burnup Calculation Code, User's Manual*, September 5, 2011.
- [34] J. Leppänen and T. Viitanen. *New Data Processing Features in the Serpent Monte Carlo Code*, April 2010.

- [35] United States Nuclear Regulatory Commission (U.S.NRC). *Reactor AP1000 Design Control Document*.
Website: <http://www.nrc.gov/reactors/new-reactors/design-cert/ap1000.htm>
- [36] Francesco Venneri, Jonghwa Chang, Won Jae Lee, Ser Gi Hon, Chris Hamilton, Chang Keun and Claudio Filippone. *Fuel Assembly Level and Full Core Analysis of the LWR Deep Burn Concept*. Logos Nuclear Systems, US Nuclear.
- [37] S.M. Bowman, I.C. Gauld, J.C. Wagner. *Recommendations on Fuel Parameters for Standard Technical Specifications for Spent Fuel Storage Casks*. Oak Ridge National Laboratory, NUREG/CR-6716 ORNL/TM-2000/385
- [38] Westinghouse Electric Corporation. *Composición de material Zirlo y procedimiento de fabricación*. Oficina Española de Patentes y Marcas, ES 2 093 055, August 1991.
- [39] US Nuclear. *FCM Replacement Fuel for LWR's*, Draft, 18/01/2012.
- [40] US Nuclear. *12X12 FCM fuel assembly calculation (Revision 3)*, January 2012.
- [41] U.S. Nuclear Regulatory Commission. *Nuclear Regulatory Legislation*. NUREG-0980
Vol.3, No.9, January 2011.
- [42] Calle Berglöf. *Basic Data Handling in Nuclear Applications*. Royal Institute of Technology, April 2012.
- [43] S.Mittag and S.Kliem. *Burning Plutonium and Minimizing the Radioactive Waste in Existing PWR*. Institute of Safety Research of Dresden, Germany.
- [44] J.L. Kloosterman, P.M.G. Damen. *Reactor physics aspects of plutonium burning in inert matrix fuels*. Journal of Nuclear Materials 274 (1999) 112-119.
- [45] Francesc Puig, Javier Dies and Clàudia Pereira. *Física de Reactores nucleares*. Universidad Politècnica de Catalunya.

